TECHNISCHE UNIVERSITÄT MÜNCHEN

Lehrstuhl für Nachrichtentechnik

Multiple Antenna Precoding: Indoor Communications and EIRP

Stefan Dierks

Vollständiger Abdruck der von der Fakultät für Elektrotechnik und Informationstechnik der Technischen Universität München zur Erlangung des akademischen Grades eines

Doktor–Ingenieurs

genehmigten Dissertation.

Vorsitzender:		Prof. Dr.-Ing. Eckehard Steinbach
Prüfer der Dissertation:	1.	Prof. Dr. sc. tech. Gerhard Kramer
	2.	Assoc. Prof. Emil Björnson, Ph.D.
	3.	Prof. Mari Kobayashi, Ph.D.

Die Dissertation wurde am 21.11.2017 bei der Technischen Universität München eingereicht und durch die Fakultät für Elektrotechnik und Informationstechnik am 22.01.2018 angenommen.

Acknowledgements

First of all, I give great gratitude to Professor Gerhard Kramer for encouraging and giving me the opportunity and the freedom to do research which finally led to this doctoral thesis. Amongst many other things, I learned how to be rigorous and precise. Without his guidance, this work would not have been possible. I also had the chance to go on many trips abroad. The most memorable one was my stay at the University of Southern California, where Professor Andreas Molisch and the people at his institute supported me in every way the could and made my stay successful. I am in debt to the examiners of my thesis Professor Emil Björnson and Professor Mari Kobayashi for taking the time to read my thesis thoroughly and improving it in many ways.

Next, I want to thank my collaborators at Nokia Networks Munich, namely Wolfgang Zirwas, Dr. Berthold Panzner, Dr. Simone Redana, and Michael Färber, for setting up our interesting projects and giving me the opportunity to work in an academic as well as in the industrial environment. Thanks also go to the doctoral students at Nokia Networks for our collaborations and for supporting me during my visits at Nokia Networks.

I enjoyed every day at the Chair for Communications Engineering (LNT) which is mainly due to the great people there. I enjoyed the many interesting scientific and non-scientific discussions with my colleagues, especially during the coffee breaks and the lunch breaks. During my time some colleagues became friends. LNT would not be possible without the non-scientific staff which are always there to support.

My family always loved me, and supported and encouraged me during my endeavors. Without them, I would not have been able to start the work on my thesis. I like to thank my friends for taking my mind off work while having fun together and giving me advice and encouragement when I needed it.

Finally, I thank the most important people in my life: my family Simone, Jannik and Jonathan. Sorry, that I had to spend much time on my thesis which I could not spend with you, and for the bad mood when I did not make as much progress as I intended. I love you.

München, November 2017 Stefan Dierks

Contents

Zusammenfassung

Massive MIMO ist ein wichtiger Bestandteil zukünftiger Mobilfunknetze. Massive MIMO und Senderkooperation für Innenraum-Kommunikation werden analysiert. Für doppelt so viele Sendeantennen wie mobile Nutzer erhält man die meisten Vorteile von Massive MIMO und erreicht einen guten Kompromiss zwischen Antennenkosten und spektraler Effizienz. Einfache Sendeverfahren erreichen Fairness und nähern sich der Kapazität an. Mit steigender Senderkooperation steigt die Performanz. Die Platzierung der Sender hat einen großen Einfluss auf die Performanz, da sie die Pfadverluste durch Mauern und die Interferenz bestimmt. Zudem wird die äquivalente isotrope Strahlungsleistung (englisch equivalent isotropically radiated power (EIRP)) von MIMO-Arrays, die durch Regulierungen beschränkt ist, analysiert. Oft können nur EIRP Schranken bestimmt werden. Mit obere Schranken kann man zeigen, dass Beschränkungen nicht verletzt werden. In der existierenden Literatur werden jedoch oft untere Schranken verwendet. Zwei neue obere Schranken, die für Mehr-Stream-Senden gelten, werden gezeigt. Die Vorteile von Massive MIMO sind auch für EIRP Beschränkungen erreichbar, die Beschränkungen sollten jedoch bei Analysen berücksichtigt werden.

Abstract

Massive MIMO is a key part of future mobile networks. Massive MIMO and transmitter cooperation for indoor communications are analyzed. A ratio of twice as many transmitter antennas as mobile users is shown to provide most of the massive MIMO benefits and to be a good tradeoff between antenna costs and performance. Simple transmission schemes achieve fairness and perform close to capacity. Performance improves with the level of transmitter cooperation. Transmitter placement is important since wall penetration losses and interference dominate the performance. The equivalent isotropically radiated power (EIRP) of MIMO arrays is also analyzed. The EIRP is constrained by regulations. Often one can determine only EIRP bounds. Upper bounds allow to show that EIRP constraints are not violated, but in the literature usually lower bounds are used. Two new upper bounds are proposed which apply to multiple stream transmissions. The massive MIMO advantages are achievable given EIRP constraints, but EIRP constraints should be included in massive MIMO analyses.

1

Introduction

The mobile data volume is expected to continue to increase, and this growth will open possibilities for new applications in mobile networks [1]. One goal of new mobile communication standards, for example, 5th generation mobile networks (5G), is to increase the throughput per unit area or volume by a factor of 1000 [1]. For example, the METIS (Mobile and wireless communications Enablers for the Twenty-twenty Information Society) project [2] defines target traffic volume densities for different scenarios. The goals can be achieved by [3]:

- ▷ Densifying base station (BS) deployments and increasing the number of served user equipments (UEs);
- ▷ Increasing bandwidth, for example, by using the millimeter wave spectrum;
- ▷ Increasing spectral efficiency (SE) through multiple antenna communications, i.e., multiple-input multiple-output (MIMO) communications.

We concentrate on the third method and focus on an idea called *massive MIMO*.

MIMO allows one BS to transmit several streams to one or more UEs using spatial degrees-of-freedom. Massive MIMO refers to a "vast" over-provisioning of BS antennas as compared to the number of served single antenna UEs [4]. Massive MIMO claims several advantages over conventional MIMO [5]:

- ▷ Massive MIMO increases capacity by a factor of 10 or more;
- ▷ Energy efficiency improves;
- ▷ Inexpensive, low-power components suffice;

- ▷ The multiple-access layer is simplified;
- ▷ The latency is reduced;
- ▷ Massive MIMO is robust to jamming and interference.

This work consists of two parts. In Part I we analyze massive MIMO deployments in an indoor scenario with and without cooperation. In Part II we study the equivalent isotropically radiated power (EIRP) of MIMO arrays.

Outline of Part I

Many massive MIMO studies consider wide area outdoor scenarios, e.g., [4–6]. However, most mobile traffic is generated by indoor users [7]. We analyze the performance of different BS deployments with different levels of cooperation in the downlink of the 3rd Generation Partnership Project (3GPP) indoor office scenario [8]. In Chapter 2 we explain the system model and key schemes required to transmit information in a mobile network with multiple antennas. In particular we present precoding and power allocation schemes, and discuss massive MIMO in detail. Interference is often the main limitation in mobile networks. We use the presented schemes to develop interference aware signal processing in Chapter 3. The schemes differ in the level of cooperation between BSs. In Chapter 4 we present the channel model, the indoor scenario and the BS deployments. We compare the presented transmission schemes and the BS deployments in Chapter 5.

Our approach is as follows: We fix the number of served, single antenna UEs and sweep the ratio of total number of BS antennas to the number of served UEs from one to ten. This way we determine the ratio of BS antennas to served UEs that achieves the massive MIMO benefits and provides a good tradeoff between antenna costs and SE. We compare the performance of a single BS to distributed BSs inside and outside the building, and with different levels of cooperation. As expected placing a single massive MIMO BS at the center of a building causes UEs to experience large path loss and high wall penetration loss. We analyze if our transmission schemes approach capacity, if scheduling provides gains, and how our power allocations affect the performance. We compare the fairness of the transmission schemes and the deployments, and we compare the separability of the UEs in the different deployments. Finally, we quantify the performance loss due to channel estimation errors. As in conventional MIMO, channel state information (CSI) is required to enable precoding. Acquiring CSI might be more difficult in massive MIMO due to the many antennas. Our results help guide design choices for future mobile communication systems, e.g., 5G.

Outline of Part II

In the second part of this dissertation we discuss the EIRP of MIMO arrays. MIMO arrays, and especially massive MIMO arrays, concentrate their transmit power in certain spatial directions. The EIRP, i.e., the peak power density, is constrained by regulations which

serve to protect other devices and humans. However, the EIRP constraint is rarely included in MIMO performance analyses. In Chapter 6 we review the EIRP definition and present selected EIRP regulations. For most MIMO arrays one cannot measure or calculate the exact EIRP, but must rely on EIRP bounds. In Chapter 7 we analyze an EIRP lower bound in the indoor scenario of Part I. We check if the precoders violate EIRP constraints and determine the tradeoff between performance and EIRP for different numbers of transmit antennas for different levels of cooperation. In order to show that EIRP regulations are not violated one must use EIRP upper bounds. In Chapter 8 we consider an example MIMO array, which is the uniform linear array (ULA), in more detail. We review existing upper bounds which apply to single stream transmissions only. We propose new upper bounds which also apply to multiple stream transmissions and have less complexity for certain scenarios. We complete the analysis by reviewing EIRP aware transmission schemes. We conclude the work in Chapter 9.

Notation

We denote column vectors with bold lower case letters, e.g., $\boldsymbol{x}$, and matrices with bold upper case letters, e.g., $\boldsymbol{X}$. The transpose is $\cdot^{\mathsf{T}}$, the complex conjugate is $\cdot^{*}$, and the complex conjugate transpose is $\cdot^{\mathsf{H}}$. We denote the element in the i-th row and the j-th column of matrix $\boldsymbol{X}$ as $[\boldsymbol{X}]_{(i,j)}$, the i-th row as $[\boldsymbol{X}]_{(i,:)}$ and the j-th column as $[\boldsymbol{X}]_{(:,j)}$. The Euclidean norm of $\boldsymbol{x}$ is $\|\boldsymbol{x}\|_2$, the l_1 norm of $\boldsymbol{x}$ is $\|\boldsymbol{x}\|_1$, and the Frobenius norm of $\boldsymbol{X}$ is $\|\boldsymbol{X}\|_F$. The rank of $\boldsymbol{X}$ is $\operatorname{rank}(\boldsymbol{X})$. We denote a diagonal matrix having diagonal entries $\boldsymbol{x}$ as $\operatorname{diag}(\boldsymbol{x})$. The $M \times M$ identity matrix is $\boldsymbol{I}_M$. The trace of $\boldsymbol{X}$ is $\operatorname{tr}(\boldsymbol{X})$. We denote a set with calligraphic letters, e.g., $\mathcal{T} = \{1, 2, \ldots, K\}$.

Part I.

Massive MIMO for a Local Area Scenario

2

System Model, and Basics

In the downlink of a mobile communication system the goal is to send information to several user equipment (UE) devices. Each UE desires information bits that are encoded into a sequence of transmit symbols. We normalize the average power of the sequence of transmit symbols and we model the transmit symbols as independent and identically distributed (i.i.d.). We denote the single transmit symbol at one time instant of the sequence desired by the k-th UE as $s_k \in \mathbb{C}$. The number of UEs is K. We collect the transmit symbols of all UEs into a vector

$$\boldsymbol{s} = \begin{bmatrix} s_1 \\ \vdots \\ s_K \end{bmatrix} \in \mathbb{C}^K. \tag{2.1}$$

In this chapter, we explain the system model of the considered mobile communication system and some key concepts required to convey information to the UEs, for example, we describe linear precoding schemes and the mercury/water-filling power allocation scheme. These concepts are used in Chapter 3 to implement transmission schemes. Also we discuss massive MIMO in detail.

2.1. Orthogonal Frequency-Division Multiplexing

Orthogonal frequency-division multiplexing (OFDM) is a key ingredient for modern mobile communication systems. The available bandwidth is divided into subcarriers. The spectra of the subcarriers may overlap but must be orthogonal, i.e., there is no interference between subcarriers. The bandwidth of a single subcarrier is chosen smaller than the coherence bandwidth of the channel so the fading of a subcarrier is almost flat. The inter symbol

interference (ISI) between consecutive symbols on the subcarriers is eliminated by using a guard interval or a cyclic prefix [9]. Hence we can express the channel of a subcarrier by a complex scalar only.

2.2. Multiple-Input Multiple-Output

Communication systems where the base stations (BSs) and the UEs are equipped with a single antenna are called single-input single-output (SISO) systems.[1] Performance is improved when multiple antennas are used at the BSs and/or at the UEs [9]. This is called multiple-input multiple-output (MIMO). MIMO where multiple UEs are served is called multi-user MIMO. We consider single antenna UEs but multiple antenna BSs, which is more precisely called multi-user multiple-input single-output (MISO). For each UE we obtain a scalar channel per subcarrier and BS antenna.

The UEs are served by all BSs jointly or by a single BS depending on the level of cooperation between the BSs. A broadcast channel (BC) is a system where a single BS or multiple BSs jointly serve all UEs. In contrast an interference channel has multiple BSs which each serve a single UE independently. A multi-user interference channel has multiple BSs which each serve a group of UEs independently. A point-to-point channel is a system conisting of a single BS and a single UE.

2.3. System Model

We consider the downlink from N_{BS} BSs to K single antenna UEs. The i-th BS has M_i antennas. We apply OFDM with a sufficiently long cyclic prefix and the number of subcarriers is N_{SC}. Unless otherwise mentioned we assume perfect channel state information (CSI) of the complete network at all nodes. We consider one subcarrier first. The channel coefficients from the antennas of the i-th BS to the k-th UE are collected in the row vector $\boldsymbol{h}_{i,k}^{\mathsf{H}} \in \mathbb{C}^{M_i}$. We stack the channel coefficients from all BSs to the k-th UE in

$$\boldsymbol{h}_k^{\mathsf{H}} = \left[\boldsymbol{h}_{1,k}^{\mathsf{H}}, \ldots, \boldsymbol{h}_{N_{\mathrm{BS}},k}^{\mathsf{H}}\right] \in \mathbb{C}^{M}. \tag{2.2}$$

The length of $\boldsymbol{h}_k$ is the total number of BS antennas

$$M = \sum_{i=1}^{N_{\mathrm{BS}}} M_i. \tag{2.3}$$

[1] We consider throughout this work BS sites with single cells which we call BSs. In some other works a single BS site can host multiple cells.

The signals transmitted over the antennas of the i-th BS are $\boldsymbol{x}_i \in \mathbb{C}^{M_i}$ and we stack these as

$$\boldsymbol{x} = \begin{bmatrix} \boldsymbol{x}_1 \\ \vdots \\ \boldsymbol{x}_{N_{\mathrm{BS}}} \end{bmatrix} \in \mathbb{C}^M. \tag{2.4}$$

The signal received by the k-th UE is

$$y_k = \boldsymbol{h}_k^{\mathsf{H}} \boldsymbol{x} + z_k \in \mathbb{C} \tag{2.5}$$

where $z_k \in \mathbb{C}$ is independent proper complex additive white Gaussian noise (AWGN) with variance σ_N^2. The number of receive antennas is equal to the number of UEs K as we consider single antenna UEs. The received signals of all UEs for one subcarrier are collected in the vector

$$\boldsymbol{y} = \begin{bmatrix} y_1 \\ \vdots \\ y_K \end{bmatrix} = \boldsymbol{H}^{\mathsf{H}} \boldsymbol{x} + \boldsymbol{z} \in \mathbb{C}^K \tag{2.6}$$

where we collect the channel coefficients in

$$\boldsymbol{H}^{\mathsf{H}} = \begin{bmatrix} \boldsymbol{h}_1^{\mathsf{H}} \\ \vdots \\ \boldsymbol{h}_K^{\mathsf{H}} \end{bmatrix} \in \mathbb{C}^{K \times M} \tag{2.7}$$

and the i.i.d. noise random variables in

$$\boldsymbol{z} = \begin{bmatrix} z_1 \\ \vdots \\ z_K \end{bmatrix} \in \mathbb{C}^K. \tag{2.8}$$

For perfect CSI the transmit signals are precoded as

$$\boldsymbol{x} = w\left(\boldsymbol{s}, \boldsymbol{H}^{\mathsf{H}}\right) \tag{2.9}$$

where $w(\cdot, \cdot)$ is the precoding function that maps the transmit symbols and the channel coefficients to the transmit signals. Note that the precoding function w can be restricted to account for limited or no cooperation between BSs (see Chapter 3).

Our goal is to maximize the sum rate by choosing the precoding function $w(\cdot, \cdot)$ subject to transmit power constraints. The sum rate is the sum of the rates achieved by the UEs on all subcarriers. Other objectives besides the sum rate consider, for example, fairness or minimum rate constraints. We measure the fairness of the sum rate maximization in Section 5.8

Non-linear precoding schemes such as dirty paper coding (DPC), vector perturbation

and lattice-aided methods achieve better performance at the cost of higher complexity [10]. In this work we consider low complexity linear precoding. However, we do consider DPC for capacity bounding calculations.

2.3.1. Linear Precoding

For linear precoding the function $w(\cdot,\cdot)$ is linear and can be expressed by the matrix $\boldsymbol{W} = [\boldsymbol{w}_1, \ldots, \boldsymbol{w}_K] \in \mathbb{C}^{M\times K}$. The k-th column of $\boldsymbol{W}$ is the precoding vector $\boldsymbol{w}_k \in \mathbb{C}^M$ which determines the transmission of s_k. We call $\boldsymbol{W}$ the precoding matrix.[2] The transmit signals are composed as

$$\boldsymbol{x} = \boldsymbol{W}\boldsymbol{s}. \tag{2.10}$$

Note that the structure of $\boldsymbol{W}$ might be restricted to account for limited or no cooperation between BSs (see Chapter 3).

When using linear precoding we also assume a linear receiver and we treat interference as noise. The achieved rate is determined by the signal-to-interference-plus-noise ratio (SINR). Recall that we defined

$$\mathbb{E}\left[\left|s_k^{(f)}\right|^2\right] = 1 \tag{2.11}$$

for $k \in \{1,\ldots,K\}$ and $f \in \{1,\ldots,N_{\mathrm{SC}}\}$. The SINR at the k-th UE on one subcarrier is

$$\mathrm{SINR}_k = \frac{\overbrace{\mathbb{E}\left[\left|\boldsymbol{h}_k^{\mathsf{H}}\boldsymbol{w}_k s_k\right|^2\right]}^{\text{Desired signal}}}{\underbrace{\sum_{\substack{l=1\\ l\neq k}}^{K}\mathbb{E}\left[\left|\boldsymbol{h}_k^{\mathsf{H}}\boldsymbol{w}_l s_l\right|^2\right]}_{\text{Interference}} + \underbrace{\mathbb{E}\left[|z|^2\right]}_{\text{Noise}}} = \frac{\left|\boldsymbol{h}_k^{\mathsf{H}}\boldsymbol{w}_k\right|^2}{\sum\limits_{\substack{l=1\\ l\neq k}}^{K}\left|\boldsymbol{h}_k^{\mathsf{H}}\boldsymbol{w}_l\right|^2 + \sigma_N^2}. \tag{2.12}$$

For linear precoding the maximization of the sum rate over all UEs and all subcarriers given power constraints becomes the optimization problem

$$\max_{\boldsymbol{W}^{(f)},\, f\in\{1,\ldots,N_{\mathrm{SC}}\}} \quad \sum_{k=1}^{K}\sum_{f=1}^{N_{\mathrm{SC}}} C\left(\mathrm{SINR}_k^{(f)}\right) \tag{2.13}$$

subject to transmit power constraints, where $^{(f)}$ indicates the subcarrier index and $C\left(\mathrm{SINR}_k^{(f)}\right)$ is the rate achieved at $\mathrm{SINR}_k^{(f)}$.

[2] Precoding is called beamforming when only a single UE is served. In this case the precoding matrix consists of a single beamforming vector.

2.3.2. Transmit Power Constraints

We consider two BS power constraints. The first constrains the power transmitted by each BS on all subcarriers. The per-BS power constraints are

$$\sum_{f=1}^{N_{\mathrm{SC}}} \mathbb{E}\left[\left\|\boldsymbol{x}_i^{(f)}\right\|_2^2\right] \leq P_i, \quad \forall i \in \{1,\ldots,N_{\mathrm{BS}}\} \tag{2.14}$$

where P_i is the maximal power that the i-th BS may transmit. The second constraint is a relaxed version of the per-BS power constraint that constrains the total power transmitted by all BS on all subcarriers. The total power constraint is

$$\sum_{i=1}^{N_{\mathrm{BS}}}\sum_{f=1}^{N_{\mathrm{SC}}} \mathbb{E}\left[\left\|\boldsymbol{x}_i^{(f)}\right\|_2^2\right] = \sum_{f=1}^{N_{\mathrm{SC}}} \mathbb{E}\left[\left\|\boldsymbol{x}^{(f)}\right\|_2^2\right] \leq P_{\mathrm{total}} \tag{2.15}$$

where P_{total} is the maximal power that all BSs may transmit jointly. Sometimes it is simpler to find solutions for a total power constraint but usually these solutions are not permissible for per-BS power constraints. We use the total power constraint to obtain upper bounds or to obtain suboptimal schemes for per-BS power constraints by scaling back the power. Of course for a single BS the two constraints (2.14) and (2.15) coincide.

The power constraints simplify for linear precoding. The per-BS power constraints become

$$\sum_{f=1}^{N_{\mathrm{SC}}} \mathbb{E}\left[\left\|\boldsymbol{x}_i^{(f)}\right\|_2^2\right] = \sum_{f=1}^{N_{\mathrm{SC}}} \mathbb{E}\left[\left\|\boldsymbol{W}_i^{(f)}\boldsymbol{s}^{(f)}\right\|_2^2\right] = \sum_{f=1}^{N_{\mathrm{SC}}} \left\|\boldsymbol{W}_i^{(f)}\right\|_F^2 \leq P_i, \quad \forall i \in \{1,\ldots,N_{\mathrm{BS}}\} \tag{2.16}$$

where $\boldsymbol{W}_i^{(f)}$ is the part of the precoding matrix that creates the transmit signals at the i-th BS $\boldsymbol{x}_i$. The total power constraint becomes

$$\sum_{f=1}^{N_{\mathrm{SC}}} \mathbb{E}\left[\left\|\boldsymbol{x}^{(f)}\right\|_2^2\right] = \sum_{f=1}^{N_{\mathrm{SC}}} \mathbb{E}\left[\left\|\boldsymbol{W}^{(f)}\boldsymbol{s}^{(f)}\right\|_2^2\right] = \sum_{f=1}^{N_{\mathrm{SC}}} \left\|\boldsymbol{W}^{(f)}\right\|_F^2 = \sum_{k=1}^{K}\sum_{f=1}^{N_{\mathrm{SC}}} \left\|\boldsymbol{w}_k^{(f)}\right\|_2^2 \leq P_{\mathrm{total}}. \tag{2.17}$$

Other constraints include per-antenna power constraints, per subcarrier power constraints or equivalent isotropically radiated power (EIRP) constraints.

We often omit the subcarrier index $^{(f)}$ for ease of notation in the remainder of this work if f is clear from the context.

2.4. Optimal Linear Precoding Structure

In [11] the solution structure for a simpler version of the optimization problem (2.13) is derived. The authors consider a BC with a single subcarrier where a single BS transmits independent messages to the UEs. They assume that the precoding matrix $\boldsymbol{W}$ is restricted by the total power constraint (2.15). They also assume that the number M of transmit

antennas is larger than or equal to the number K of UEs.

This optimization problem is generally hard to solve [12, 13] but the optimal precoding matrix' structure is [11]

$$\boldsymbol{W}^{\text{opt}} = \boldsymbol{H}\left(\sigma_N^2 \boldsymbol{I}_K + \text{diag}\left(\boldsymbol{\lambda}\right)\boldsymbol{H}^{\mathsf{H}}\boldsymbol{H}\right)^{-1}\text{diag}\left(\boldsymbol{p}^{\text{opt}}\right)^{\frac{1}{2}} \in \mathbb{C}^{M\times K} \tag{2.18}$$

where $\boldsymbol{\lambda} \in \mathbb{R}^K$ and $\boldsymbol{p}^{\text{opt}} \in \mathbb{R}^K$. The difficulty now lies in finding the $\boldsymbol{\lambda}$ and $\boldsymbol{p}^{\text{opt}}$ which solve the optimization problem. The structure of the optimal solution consists of two main parts: $\boldsymbol{H}$ the conjugate transpose of the channel matrix and the matrix $\left(\sigma_N^2 \boldsymbol{I}_N + \text{diag}\left(\boldsymbol{\lambda}\right)\boldsymbol{H}^{\mathsf{H}}\boldsymbol{H}\right)^{-1}$. These two parts resemble two basic precoding schemes: maximum ratio transmission (MRT) and zero-forcing beamforming (ZFBF).

2.4.1. Maximum Ratio Transmission

For maximum ratio transmission (MRT) [14] we choose the precoding vector $\boldsymbol{w}_k \in \mathbb{C}^M$ of the k-th UE as a filter matched to its channel vector $\boldsymbol{h}_k^{\mathsf{H}}$. The MRT precoding matrix for all UEs is

$$\boldsymbol{W}^{\text{MRT}} = \boldsymbol{H}\,\text{diag}\left(\boldsymbol{p}^{\text{MRT}}\right)^{\frac{1}{2}} \in \mathbb{C}^{M\times K} \tag{2.19}$$

where the diagonal matrix $\text{diag}\left(\boldsymbol{p}^{\text{MRT}}\right)$ serves to distribute the transmission power while fulfilling the power constraint. MRT precoding maximizes the received signal power at the UEs [11]. The signal power scales proportional to the number M of BS antennas [6]. This is called array gain. However, the interference between UEs is not considered, which is visualized in Figure 2.1. The MRT precoding vector of the k-th UE $\boldsymbol{w}_{k,\text{MRT}}$ points in the same direction as $\boldsymbol{h}_k$ the conjugate transpose of the channel vector.

MRT precoding is optimal in noise limited systems [11] or when transmitting a single symbol to a single UE. We use MRT to transmit to a single UE in which case all power is assigned to that single UE.

Note that MRT can be used for any ratio of transmit antennas to single antenna UEs. However, interference is large when there are few transmit antennas compared to number of UEs or for correlated channels. Increasing the number of antennas at the BS leads to diminishing interference (as long as the condition number of the channel matrix increases when adding antennas) [15]. This is one advantage of massive MIMO, as we will learn in Section 2.9.

To show that MRT is optimal in the low signal-to-noise ratio (SNR) regime, we divide the numerator and the denominator of the optimal precoding matrix (2.18) by σ_N^2. Since the diagonal matrix $\text{diag}\left(\boldsymbol{p}^{\text{opt}}\right)$ is subject to optimization we can move $1/\sigma_N^2$ into $\text{diag}\left(\boldsymbol{p}^{\text{opt}}\right)$ and arrive at

$$\boldsymbol{W}^{\text{opt}} = \boldsymbol{H}\left(\boldsymbol{I}_K + \frac{1}{\sigma_N^2}\text{diag}\left(\boldsymbol{\lambda}\right)\boldsymbol{H}^{\mathsf{H}}\boldsymbol{H}\right)^{-1}\text{diag}\left(\boldsymbol{p}^{\text{opt}}\right)^{\frac{1}{2}}. \tag{2.20}$$

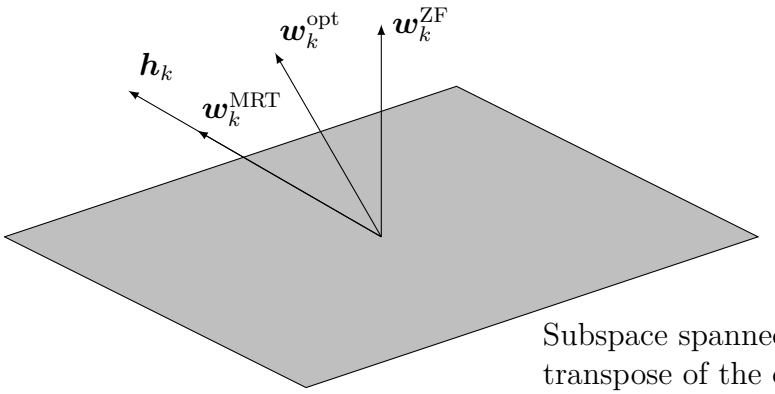

Figure 2.1.: Conjugate transpose of the channel vector of the k-th UE $\boldsymbol{h}_k$, optimal precoding vector $\boldsymbol{w}_k^{\text{opt}}$, MRT precoding vector $\boldsymbol{w}_k^{\text{MRT}}$ and ZFBF vector $\boldsymbol{w}_k^{\text{ZF}}$.

In the low SNR regime ($\sigma_N^2 \to \infty$) the optimal precoding (2.20) hence approaches MRT

$$\lim_{\substack{\sigma_N^2 \to \infty \\ \|\boldsymbol{W}^{\text{opt}}\|_F^2 \leq P_{\text{total}} < \infty}} \boldsymbol{W}^{\text{opt}} = \boldsymbol{H} \, \text{diag}\left(\boldsymbol{p}^{\text{opt}}\right)^{\frac{1}{2}}. \tag{2.21}$$

2.4.2. Zero-Forcing Beamforming

For zero-forcing beamforming (ZFBF) the linear precoding matrix is determined according to an interference zero forcing objective

$$\boldsymbol{h}_i^{\mathsf{H}} \boldsymbol{w}_k^{\text{ZF}} = 0, \quad i \neq k. \tag{2.22}$$

Zero interference is visualized in Figure 2.1. The ZFBF precoding vector of the k-th UE $\boldsymbol{w}_k^{\text{ZF}} \in \mathbb{C}^K$ is orthogonal to the subspace spanned by the transpose conjugate channel vectors of all other UEs.

Also note that the optimal linear precoder $\boldsymbol{w}_k^{\text{opt}}$ lies somewhere in between the MRT precoding vector and the ZFBF precoding vector [11]. It is a trade off between maximization of the received signal powers and the suppression of interference.

In matrix notation zero interference is

$$\boldsymbol{H}^{\mathsf{H}} \boldsymbol{W}^{\text{ZF}} = \text{diag}\left(\tilde{\boldsymbol{p}}\right)^{\frac{1}{2}} \tag{2.23}$$

where $\tilde{\boldsymbol{p}} = [\tilde{p}_1, \ldots, \tilde{p}_K] \in \mathbb{C}^K$ and $\boldsymbol{W}^{\text{ZF}} = \left[\boldsymbol{w}_1^{\text{ZF}}, \ldots, \boldsymbol{w}_K^{\text{ZF}}\right] \in \mathbb{C}^{M \times K}$. A solution exists if the rank of the channel matrix $\boldsymbol{H}^{\mathsf{H}}$ is larger or equal to the number of UEs

$$\text{rank}\left(\boldsymbol{H}^{\mathsf{H}}\right) \geq K. \tag{2.24}$$

For our system model we assume full column-rank for $\boldsymbol{H}^{\mathsf{H}}$ and at least as many transmit antennas as UEs, i.e., $M \geq K$. The received signals with ZFBF are

$$\begin{aligned} \boldsymbol{y} &= \boldsymbol{H}^{\mathsf{H}} \boldsymbol{W}^{\mathrm{ZF}} \boldsymbol{s} + \boldsymbol{z} \\ &= \operatorname{diag}\left(\tilde{\boldsymbol{p}}\right)^{\frac{1}{2}} \boldsymbol{s} + \boldsymbol{z}. \end{aligned} \tag{2.25}$$

We obtain K parallel interference-free channels. The optimization problem with an interference zero forcing constraint is

$$\begin{aligned} \max_{\boldsymbol{W}^{\mathrm{ZF}}} \quad & \sum_{k=1}^{K} C\left(\mathrm{SNR}_k\right) \\ \text{s.t.} \quad & \boldsymbol{H}^{\mathsf{H}} \boldsymbol{W}^{\mathrm{ZF}} = \operatorname{diag}\left(\tilde{\boldsymbol{p}}\right)^{\frac{1}{2}} \\ & \left\| \boldsymbol{W}^{\mathrm{ZF}} \right\|_F^2 \leq P_{\mathrm{total}} \end{aligned} \tag{2.26}$$

where the SNR of the k-th UE is $\mathrm{SNR}_k = \frac{\tilde{p}_k}{\sigma_N^2}$. Note that the SINR simplifies to the SNR when there is no interference.

The optimal solution given the total power constraint (2.15) is the pseudo-inverse combined with a power allocation [16]. The pseudo-inverse of the channel matrix $\boldsymbol{H}^{\mathsf{H}}$ is

$$\boldsymbol{H}^{\dagger} = \boldsymbol{H} \left(\boldsymbol{H}^{\mathsf{H}} \boldsymbol{H} \right)^{-1} \in \mathbb{C}^{M \times K}. \tag{2.27}$$

The optimal zero-forcing precoder given the total power constraint (2.15) is

$$\boldsymbol{W}^{\mathrm{ZF}} = \boldsymbol{H}^{\dagger} \operatorname{diag}\left(\tilde{\boldsymbol{p}}\right)^{\frac{1}{2}} = \boldsymbol{H} \left(\boldsymbol{H}^{\mathsf{H}} \boldsymbol{H} \right)^{-1} \operatorname{diag}\left(\tilde{\boldsymbol{p}}\right)^{\frac{1}{2}}. \tag{2.28}$$

where $\operatorname{diag}\left(\tilde{\boldsymbol{p}}\right)$ is the diagonal power allocation matrix. It is easy to see that (2.28) fulfills (2.23).

The total power transmitted on a single subcarrier is

$$\mathbb{E}\left[\|\boldsymbol{x}\|_2^2 \right] = \left\| \boldsymbol{W}^{\mathrm{ZF}} \right\|_F^2 = \left\| \boldsymbol{H}^{\dagger} \operatorname{diag}\left(\tilde{\boldsymbol{p}}\right)^{\frac{1}{2}} \right\|_F^2. \tag{2.29}$$

Allocating the same amount of power to different UEs has different effects on the total power depending on the norm of the UE's column of the pseudo-inverse matrix $\boldsymbol{H}^{\dagger}$. The norms of the columns of the pseudo-inverse are different since the product of the channel matrix times its pseudo-inverse is not only a diagonal matrix but an identity matrix. This means that for the same allocated power, UEs have the same received power. In other words, UEs that are further away require more power than closer UEs. This means that the columns of $\boldsymbol{W}^{\mathrm{ZF}}$ corresponding to the further away UEs have larger norms.

We split the diagonal power allocation matrix into

$$\operatorname{diag}\left(\tilde{\boldsymbol{p}}\right) = \operatorname{diag}\left(\tilde{\boldsymbol{h}}\right)^2 \operatorname{diag}\left(\boldsymbol{p}\right) \in \mathbb{R}^{K \times K} \tag{2.30}$$

to make power allocation easier, where

$$\tilde{\boldsymbol{h}} = \begin{bmatrix} \tilde{h}_1 \\ \vdots \\ \tilde{h}_K \end{bmatrix} = \begin{bmatrix} \frac{1}{\left\| \left[\boldsymbol{H}^\dagger\right]_{(:,1)} \right\|_2} \\ \vdots \\ \frac{1}{\left\| \left[\boldsymbol{H}^\dagger\right]_{(:,K)} \right\|_2} \end{bmatrix} \in \mathbb{R}^K \tag{2.31}$$

and the entries of the diagonal matrix $\operatorname{diag}(\boldsymbol{p})$ are

$$\boldsymbol{p} = [p_1, \ldots, p_K] \in \mathbb{R}^K. \tag{2.32}$$

The advantage of the diagonal power allocation matrix $\operatorname{diag}(\boldsymbol{p})$ is that the total transmit power is equal to the sum of its diagonal elements

$$\begin{aligned} \left\| \boldsymbol{W}^{\mathrm{ZF}} \right\|_F^2 = \left\| \boldsymbol{H}^\dagger \operatorname{diag}(\tilde{\boldsymbol{p}})^{\frac{1}{2}} \right\|_F^2 &= \left\| \begin{bmatrix} \left[\boldsymbol{H}^\dagger\right]_{(:,1)} \sqrt{\tilde{p}_1} \\ \vdots \\ \left[\boldsymbol{H}^\dagger\right]_{(:,K)} \sqrt{\tilde{p}_K} \end{bmatrix} \right\|_2^2 = \sum_{k=1}^K \left\| \left[\boldsymbol{H}^\dagger\right]_{(:,k)} \sqrt{\tilde{p}_k} \right\|_2^2 \\ &= \sum_{k=1}^K \tilde{p}_k \left\| \left[\boldsymbol{H}^\dagger\right]_{(:,k)} \right\|_2^2 = \sum_{k=1}^K \tilde{h}_k^2 p_k \left\| \left[\boldsymbol{H}^\dagger\right]_{(:,k)} \right\|_2^2 = \sum_{k=1}^K p_k = \|\boldsymbol{p}\|_1 . \end{aligned} \tag{2.33}$$

However, allocating the same amount of power to UEs in $\operatorname{diag}(\tilde{\boldsymbol{p}})$ does not lead to the same received powers at these UEs. The received powers are scaled by the effective channels, which are collected in $\tilde{\boldsymbol{h}}$, i.e., the amplitudes of the interference free channels to the UEs are the inverses of the norms of the columns of the pseudo inverse. The received signals become

$$\begin{aligned} \boldsymbol{y} &= \operatorname{diag}(\tilde{\boldsymbol{p}})^{\frac{1}{2}} \boldsymbol{s} + \boldsymbol{z} \\ &= \operatorname{diag}\left(\tilde{\boldsymbol{h}}\right) \operatorname{diag}(\boldsymbol{p})^{\frac{1}{2}} \boldsymbol{s} + \boldsymbol{z}. \end{aligned} \tag{2.34}$$

ZFBF precoding is optimal at high SNR ($\sigma_N^2 \to 0$) [11]. Observe (2.18) at high SNR

$$\lim_{\substack{\sigma_N^2 \to 0 \\ 0 < \|\boldsymbol{W}^{\mathrm{opt}}\|_F^2 \leq P_{\mathrm{total}}}} \boldsymbol{W}^{\mathrm{opt}} = \boldsymbol{H} \left(\boldsymbol{H}^{\mathsf{H}} \boldsymbol{H}\right)^{-1} \operatorname{diag}(\boldsymbol{\lambda})^{-1} \operatorname{diag}\left(\boldsymbol{p}^{\mathrm{opt}}\right)^{\frac{1}{2}}. \tag{2.35}$$

This is equal to (2.28) as $\left(\operatorname{diag}(\boldsymbol{\lambda})^{-1} \operatorname{diag}(\boldsymbol{p}^{\mathrm{opt}})^{\frac{1}{2}}\right)$ plays the role of $\operatorname{diag}(\tilde{\boldsymbol{p}})^{\frac{1}{2}}$.

The pseudo-inverse is not a unique solution to (2.23). A generalized inverse $\boldsymbol{H}^-$ of a channel matrix $\boldsymbol{H}^{\mathsf{H}}$ with full row-rank fulfills [16]

$$\boldsymbol{H}^{\mathsf{H}} \boldsymbol{H}^- = \boldsymbol{I}_K. \tag{2.36}$$

The pseudo-inverse is optimal given a total power constraint. However, finding the optimal generalized inverse for other power constraints, like the per-BS power constraint (2.16), requires to solve a semi-definite program [16]. This is not in the scope of this work as we are interested in low complexity calculations as well as implementations.

We discuss how we use the solutions for the BC given a total power constraint to find suboptimal solutions for the BC given per-BS power constraints in Chapter 3.

2.5. Capacity of an AWGN Channel with QAM

The capacity of a SISO point-to-point AWGN channel without memory is [17]

$$C\left(\mathrm{SNR}\right) = \log_2\left(1 + \mathrm{SNR}\right). \tag{2.37}$$

To achieve capacity continuous (Gaussian distributed) transmit symbols, continuous output, and optimal channel coding are necessary. Optimal channel coding means that unlimited effort may be taken in encoding and decoding, while the length of a code sequence can approach infinity.

In real communication systems the transmit symbols are not continuous but from a discrete set. We still assume a continuous output to upper bound the performance achieved with finite quantization resolution at the analog-to-digital converters. One can view this as a channel with discrete transmit symbols and continuous output. The discrete symbol set is called a modulation alphabet, while the mapping from the encoded bits to the modulation alphabet is called modulation. The combination of channel coding and modulation is called coded modulation. The rates achievable with finite alphabet coded modulation are less than capacity even with optimal channel coding.

We use rectangular quadrature amplitude modulation (QAM) with N_{QAM} equiprobable modulation symbols.[3] We determine the capacity of a channel with equiprobable modulation symbols (discrete transmit symbols) and continuous output as [19]

$$C_{N_{\mathrm{QAM}}}\left(\mathrm{SNR}\right) = \log_2\left(N_{\mathrm{QAM}}\right) - \frac{1}{N_{\mathrm{QAM}}} \sum_{i=0}^{N_{\mathrm{QAM}}-1} \mathbb{E}\left[\log_2\left(\sum_{k=0}^{N_{\mathrm{QAM}}-1} e^{-\left|\mathrm{SNR}\left(s^{(i)}-s^{(k)}\right)+z\right|^2-|z|^2}\right)\right] \tag{2.38}$$

where z is the proper complex AWGN with unit variance and $s^{(i)}$ is the i-th symbol of the modulation alphabet.

In order to save simulation time we do not calculate capacity by (2.38). Instead we create a table of SNR and capacity value pairs and interpolate between them to obtain the approximate capacity value for an SNR value.

Figure 2.2 shows the capacities of an AWGN channel with Gaussian modulation, 256 QAM, 64 QAM, and 16 QAM and continuous output. The capacity $C_{N_{\mathrm{QAM}}}$ with QAM is close to $C\left(\mathrm{SNR}\right)$ for low SNR, while it saturates at $\log_2\left(N_{\mathrm{QAM}}\right)$ bit for higher SNR.

[3] The rates can be improved by shaping the probabilities of the modulation alphabet symbols [18].

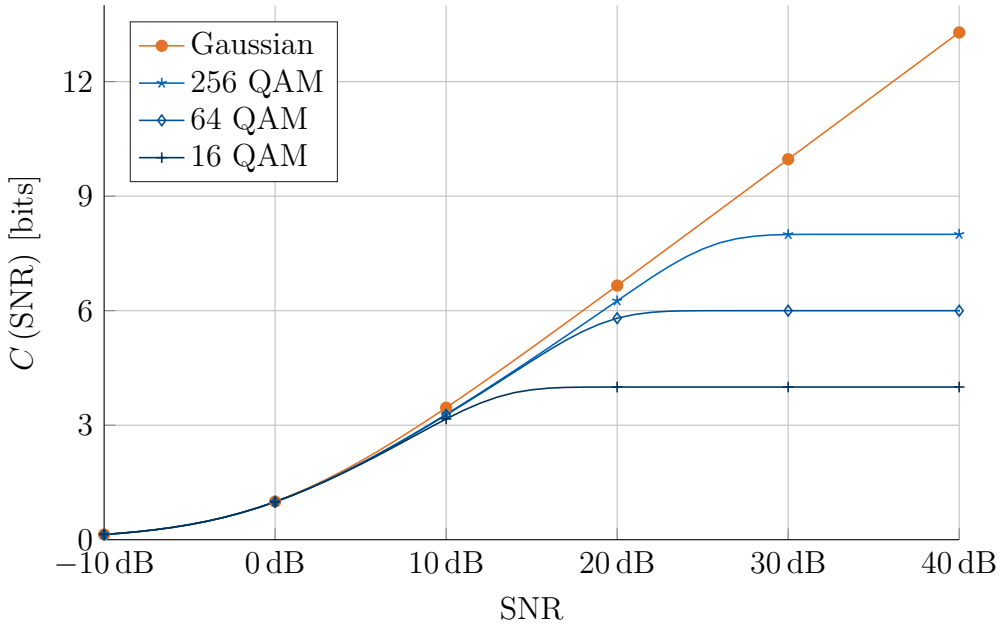

Figure 2.2.: Capacity of an AWGN channel with Gaussian modulation, 256 QAM, 64 QAM, and 16 QAM and continuous output.

2.6. Mercury/Water-filling

Using OFDM and ZFBF we obtain K independent parallel channels for each of the N_{SC} subcarriers. Recall that $\tilde{\boldsymbol{h}}^{(f)}$ are the effective channel gains of the f-th subcarrier. For ease of notation when allocating power we collect the channel gains in

$$\overline{\boldsymbol{h}} = \begin{bmatrix} \tilde{\boldsymbol{h}}^{(1)} \\ \vdots \\ \tilde{\boldsymbol{h}}^{(N_{\mathrm{SC}})} \end{bmatrix} \in \mathbb{R}^{KN_{\mathrm{SC}}}. \tag{2.39}$$

Now we can access a channel gain $\overline{h}_i$ by the single index i. Recall that the noise variance of each channel is σ_N^2. Our goal is to maximize the sum rate given a total power constraint

$$\overline{\boldsymbol{p}}^{\mathrm{opt}} = \arg \max_{\overline{\boldsymbol{p}}:\, \|\overline{\boldsymbol{p}}\|_1 \leq P_{\mathrm{total}}} \sum_{i=1}^{KN_{\mathrm{SC}}} C\left(\mathrm{SNR}_i\right) \tag{2.40}$$

where

$$\overline{\boldsymbol{p}} = \begin{bmatrix} \overline{p}_1 \\ \vdots \\ \overline{p}_{KN_{\mathrm{SC}}} \end{bmatrix} \in \mathbb{R}^{KN_{\mathrm{SC}}} \tag{2.41}$$

is the power allocation vector. The SNR is

$$\mathrm{SNR}_i = \frac{\mathbb{E}\left[\left|\overline{h}_i\sqrt{\overline{p}_i}s_i\right|\right]^2}{\sigma_N^2} = \frac{|\overline{h}_i|^2\overline{p}_i}{\sigma_N^2} \tag{2.42}$$

We use a minimum mean squared error (MMSE) estimator at the receiver to estimate the transmit symbol s. We denote the corresponding MMSE by $\mathrm{MMSE}\left(\mathrm{SNR}\right)$ and the inverse MMSE by $\mathrm{MMSE}^{-1}\left(\zeta\right)$.

The inverse MMSE is the key ingredient of mercury/water-filling which finds the optimal power allocation vector $\overline{\boldsymbol{p}}^{\mathrm{opt}}$ for channels with discrete input and continuous output [20,21]. It is a generalization of water-filling which finds the optimal power allocation for channels with continuous input (i.e., Gaussian modulation) and continuous output [22].

The solution to (2.40) is [20]

$$\overline{p}_i^{\star} = \frac{\sigma_N^2}{|\overline{h}_i|^2}\mathrm{MMSE}^{-1}\left(\min\left\{1, \frac{\sigma_N^2}{|\overline{h}_i|^2}\eta\right\}\right), \quad i = 1, \ldots, KN_{\mathrm{SC}} \tag{2.43}$$

where η is the unique solution to

$$\sum_{\substack{i=1 \\ \frac{|\overline{h}_i|^2}{\sigma_N^2} > \eta}}^{KN_{\mathrm{SC}}} \frac{\sigma_N^2}{|\overline{h}_i|^2}\mathrm{MMSE}^{-1}\left(\frac{\sigma_N^2}{|\overline{h}_i|^2}\eta\right) = P_{\mathrm{total}}. \tag{2.44}$$

For mercury/water-filling we first solve the nonlinear equation (2.44). Then we obtain the optimal power allocation from (2.43).

The MMSE is related to capacity as [23]

$$\frac{1}{\log_e\left(2\right)}\frac{d\,C\left(\mathrm{SNR}\right)}{d\,\mathrm{SNR}} = \mathrm{MMSE}\left(\mathrm{SNR}\right). \tag{2.45}$$

where the prefactor $1/\log_e\left(2\right)$ converts the capacity from bits to nats.

For closed form capacity expressions one can obtain the MMSE and its inverse directly. For Gaussian modulation the MMSE is [23]

$$\mathrm{MMSE}\left(\mathrm{SNR}\right) = \frac{1}{1+\mathrm{SNR}} = \frac{1}{1+\frac{|\overline{h}_i|^2\overline{p}_i}{\sigma_N^2}} \tag{2.46}$$

and its inverse is

$$\mathrm{MMSE}^{-1}\left(\zeta\right) = \frac{1}{\zeta} - 1. \tag{2.47}$$

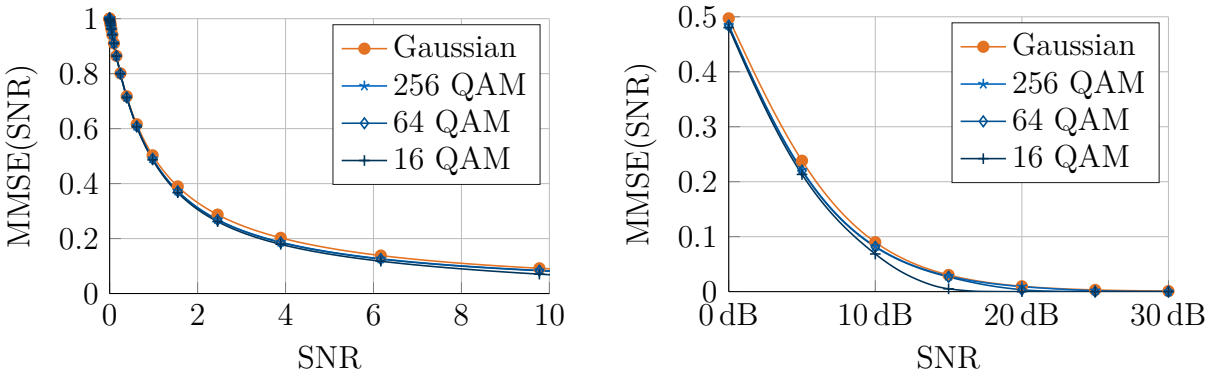

(a) Linear SNR.

(b) Logarithmic SNR.

Figure 2.3.: MMSE of an AWGN channel with Gaussian modulation, 256 QAM, 64 QAM, and 16 QAM and a continuous output.

Hence mercury/water-filling reduces for Gaussian modulation to water-filling [21]

$$\overline{p}_i^{\mathrm{wf}} = \begin{cases} 0, & \frac{|\overline{h}_i|^2}{\sigma_N^2} \leq \eta \\ \frac{1}{\eta} - \frac{\sigma_N^2}{|\overline{h}_i|^2}, & \frac{|\overline{h}_i|^2}{\sigma_N^2} > \eta \end{cases}. \tag{2.48}$$

However, for QAM inputs a closed form expression of the capacity is not known. The MMSE for a rectangular equiprobable QAM with N_{QAM} symbols can be obtained as [20]

$$\mathrm{MMSE}\left(\mathrm{SNR}\right) = 1 - \frac{1}{N_{\mathrm{QAM}}\pi} \int \frac{\left| \sum_{i=1}^{N_{\mathrm{QAM}}} s^{(i)} e^{-|y-\sqrt{\mathrm{SNR}/2}s^{(i)}|^2} \right|^2}{\sum_{i=1}^{N_{\mathrm{QAM}}} e^{-|y-\sqrt{\mathrm{SNR}/2}s^{(i)}|^2}} \mathrm{d}y. \tag{2.49}$$

We choose a different approach and use a table of capacity versus SNR pairs. From these pairs we approximate the inverse MMSE function. We obtain the MMSE versus SNR pairs from the capacity versus SNR pairs by numerical differentiation. Figure 2.3 shows the MMSE plots for Gaussian modulation and different QAM constellations. The inverse MMSE functions maps from an MMSE value ζ to an SNR value. We find the two closest MMSE values to ζ and interpolate linearly to approximate the inverse MMSE function. Figure 2.4 shows the inverse MMSE for Gaussian modulation and different QAM constellations.

With the approximate inverse MMSE function we solve (2.44) and then (2.43) to obtain the optimal power allocation. The optimal power allocation has two graphical interpretations [21]: Figure 2.5 shows the first interpretation. The functions $\frac{|\overline{h}_i|^2}{\sigma_N^2}\mathrm{MMSE}\left(\frac{|\overline{h}_i|^2}{\sigma_N^2}\overline{p}_i\right)$ versus $\overline{p}_i$ for each parallel channel are plotted in one diagram. The optimal power allocation is found by a vertical line at height η. The height η is such that the $\overline{p}_i^{\star}$ values, corresponding to the intersections of the vertical line with the functions, add up to the

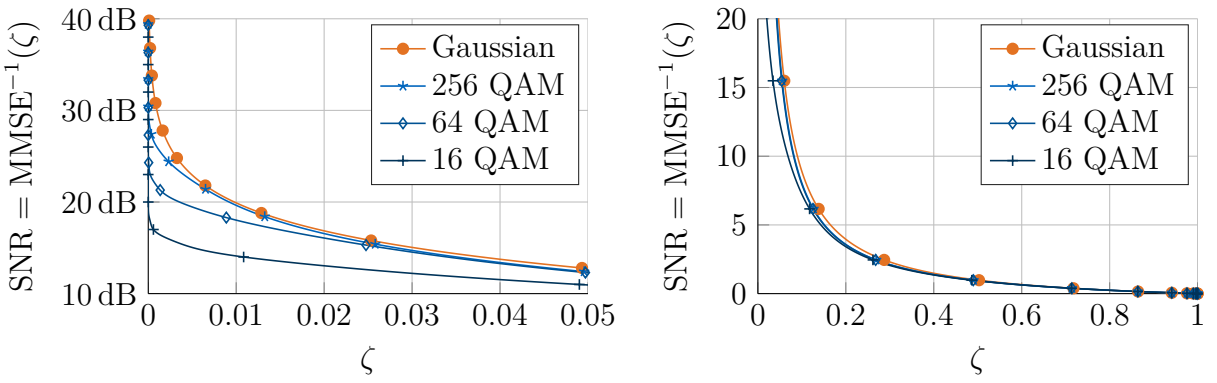

(a) Logarithmic SNR.

(b) Linear SNR.

Figure 2.4.: Inverse MMSE of an AWGN channel with Gaussian modulation, 256 QAM, 64 QAM, and 16 QAM and continuous output.

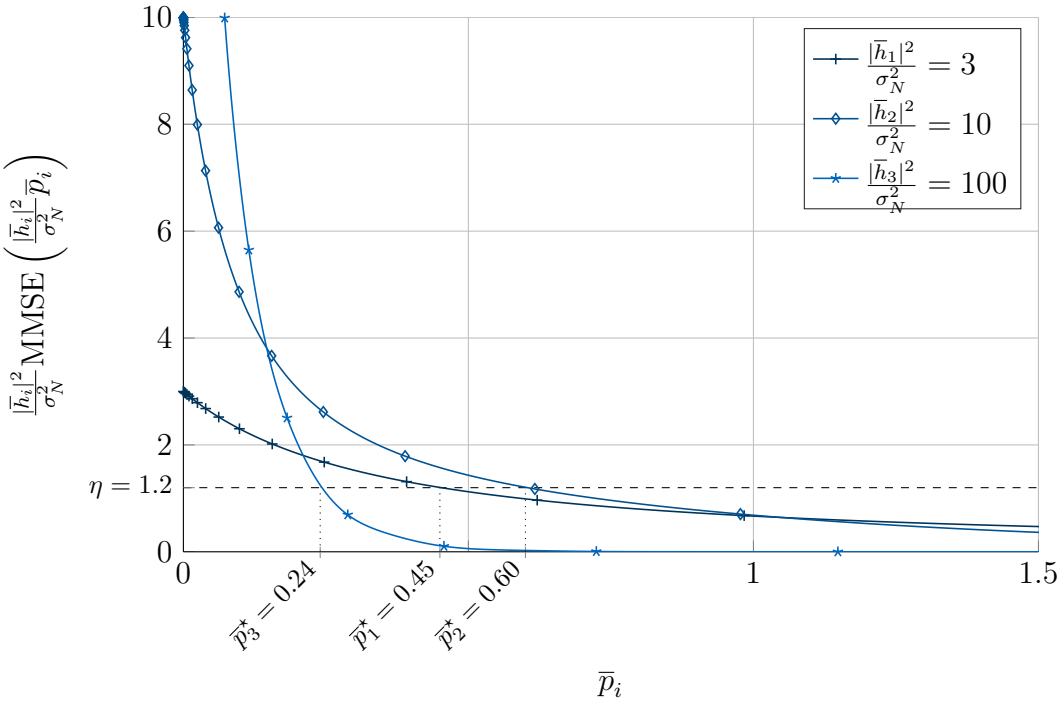

Figure 2.5.: Visualization of mercury/water-filling with 16 QAM transmitted on three parallel channels. The noise is normalized to $\sigma_N^2 = 1$.

maximal total power P_{total}.

Figure 2.6 shows the second interpretation. The graphical interpretation of classic water-filling is to pour water into vessels which are solid up to height $\frac{\sigma_N^2}{|\bar{h}_i|^2}$. For mercury/water-filling mercury of height ι_i is filled into each vessel before the water is poured.

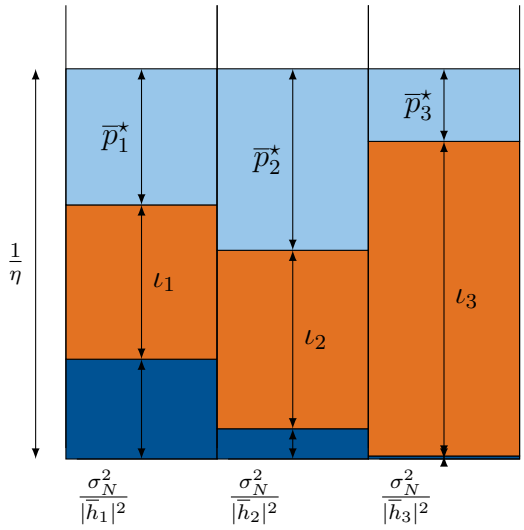

Figure 2.6.: Graphical interpretation of mercury/water-filling with 16 QAM transmitted on the same three parallel channels as in Figure 2.5.

The mercury accounts for the gap between ideal Gaussian modulation and the discrete modulation. The height of the mercury is determined as

$$\iota_i = \frac{G\left(\frac{\eta\sigma_N^2}{|\overline{h}_i|^2}\right)\sigma_N^2}{|\overline{h}_i|^2} - \frac{\sigma_N^2}{|\overline{h}_i|^2} \tag{2.50}$$

where

$$G(\zeta) = \begin{cases} \frac{1}{\zeta} - \mathrm{MMSE}^{-1}(\zeta), & 0 \le \zeta \le 1 \\ 1, & \zeta > 1. \end{cases} \tag{2.51}$$

The water level in the vessels is $1/\eta$ while the water height over the mercury is the power allocated to the parallel channel.

The excess power required by water-filling over mercury/water-filling is analyzed in [21, 24]. We analyze the gap between rates achieved with mercury/water-filling and with water-filling in Section 5.6. Mercury/water-filling can be extended to support varying modulation alphabets on the parallel channels, different user priorities and limited CSI [21, 25, 26].

Other power allocation schemes are described, for example, in [27, 28].

2.7. Capacity of a MIMO OFDM Broadcast Channel

As a meaningful benchmark for the linear transmission schemes we determine the capacity of a MIMO OFDM BC channel. We consider the capacity of a general MIMO BC first and then explain how the calculations simplify for single antenna UEs with OFDM.

The capacity of a MIMO BC is achieved by DPC [29–32]. DPC [33] is a non linear transmission scheme which requires to optimize the transmit covariance matrices. DPC is considered too complex for implementation in practical networks.

The capacity of a BC is obtained by maximizing [34]

$$C_{\mathrm{BC}}\left(\boldsymbol{H}_1^{\mathsf{H}},\ldots,\boldsymbol{H}_K^{\mathsf{H}},P_{\mathrm{total}}\right)=\max_{\substack{\boldsymbol{\Sigma}_k\succeq 0\\ \sum_{k=1}^{K}\mathrm{tr}(\boldsymbol{\Sigma}_k)\leq P_{\mathrm{total}}}}\Bigg[\log_2\left(1+\boldsymbol{H}_1^{\mathsf{H}}\boldsymbol{\Sigma}_1\boldsymbol{H}_1\right)+\log_2\left(\frac{1+\boldsymbol{H}_2^{\mathsf{H}}\left(\boldsymbol{\Sigma}_1+\boldsymbol{\Sigma}_2\right)\boldsymbol{H}_2}{1+\boldsymbol{H}_2^{\mathsf{H}}\boldsymbol{\Sigma}_1\boldsymbol{H}_2}\right)+\ldots+\log_2\left(\frac{1+\boldsymbol{H}_K^{\mathsf{H}}\left(\boldsymbol{\Sigma}_1+\ldots+\boldsymbol{\Sigma}_{K-1}+\boldsymbol{\Sigma}_K\right)\boldsymbol{H}_K}{1+\boldsymbol{H}_K^{\mathsf{H}}\left(\boldsymbol{\Sigma}_1+\ldots+\boldsymbol{\Sigma}_{K-1}\right)\boldsymbol{H}_K}\right)\Bigg] \tag{2.52}$$

where $\boldsymbol{H}_k^{\mathsf{H}}$ is the channel matrix of the k-th UE and the optimization is over the positive semi-definite downlink covariance matrices $\{\boldsymbol{\Sigma}_1,\ldots,\boldsymbol{\Sigma}_K\}$. Finding the covariance matrices is a non convex problem.

The problem can be transformed into the dual problem of a multiple-access channel (MAC), where each UE desires to transmit information to the BS. Here the uplink channel matrices are the conjugate transpose of the downlink channel matrices. The dual MAC problem is [31]

$$\max_{\substack{\boldsymbol{Q}_k\succeq 0\\ \sum_{k=1}^{K}\mathrm{tr}(\boldsymbol{Q}_k)\leq P_{\mathrm{total}}}}\log_2\left|\boldsymbol{I}+\sum_{k=1}^{K}\boldsymbol{H}_k\boldsymbol{Q}_k\boldsymbol{H}_k^{\mathsf{H}}\right| \tag{2.53}$$

where the optimization is over the positive semi-definite uplink covariance matrices $\{\boldsymbol{Q}_1,\ldots,\boldsymbol{Q}_K\}$. The capacity of the dual total power constrained MAC and the BC are equal [34]. The optimal downlink covariance matrices can be obtained by the MAC-BC duality from the uplink covariance matrices [31].

A MAC problem with per-UE constraints is solved via iterative water-filling [35]. It resembles the uplink in a wireless network. Since its constraints are separable it suffices to optimize one covariance matrix after the other while treating the other covariances matrices as constants [34]. The optimization of each covariance matrix is transformed into water-filling. The water level of a UE is chosen such that its per-UE power constraint is fulfilled.

However, the dual MAC we wish to solve has a total power constraint. To solve this optimization problem the iterative water-filling is modified. We use the hybrid algorithm from [34] where the covariance matrices are updated simultaneously. The covariance matrices of the other UEs are treated again as constant at each UE during the update. However, the constant covariance matrices are averaged over the previous steps to ensure convergence. Water-filling gives the new covariance matrices. This algorithm always converges [34]. Other algorithms are described, for example, in [36, 37].

One can view the OFDM subcarriers as virtual antennas when determining capacity [38].

We collect the subcarrier channel vectors of the k-th UE to obtain its block diagonal virtual channel matrix

$$\boldsymbol{H}_k^{\mathsf{H}} = \begin{bmatrix} \left(\boldsymbol{h}_k^{(1)}\right)^{\mathsf{H}} & \mathbf{0} & \cdots & \mathbf{0} \\ \mathbf{0} & \left(\boldsymbol{h}_k^{(2)}\right)^{\mathsf{H}} & \cdots & \mathbf{0} \\ \vdots & \ddots & \ddots & \vdots \\ \mathbf{0} & \cdots & \mathbf{0} & \left(\boldsymbol{h}_k^{(N_{\mathrm{SC}})}\right)^{\mathsf{H}} \end{bmatrix} \in N_{\mathrm{SC}} \times \mathbb{C}^{MN_{\mathrm{SC}}} \tag{2.54}$$

where $\left(\boldsymbol{h}_k^{(f)}\right)^{\mathsf{H}}$ is the channel vector of the k-th UE on the f-th subcarrier. Instead of inserting the $\boldsymbol{H}_k^{\mathsf{H}}$ matrices directly into (2.52) we make use of their block diagonal structure.

2.8. Scheduling

Selecting the subset of UEs a BS transmits information to on a subcarrier is called scheduling. Scheduling aims to maximize the sum rate or other performance measures [39]. Scheduling is especially helpful if the number K of UEs connected to a BS is larger than the number M of BS antennas.

We use the low complexity scheduling algorithm from [40] to choose a UE subset for each subcarrier when $K > M$. The goal of the algorithm is to maximize the sum rate in a BC given a total power constraint. We choose this algorithm because it performs close to optimal with lower computational complexity compared to other algorithms [40].

Sato's upper bound of the capacity of a BC is obtained by assuming that the UEs are allowed to cooperate which leads to a virtual point-to-point MIMO channel with distributed antennas [41]. The algorithm schedules the UEs to maximize the sum rate of the virtual point-to-point channel. The sum rate of the virtual point-to-point MIMO channel where we allocate transmit power equally to the streams is [42]

$$R\left(\boldsymbol{H}^{\mathsf{H}}\right) = \log_2 \left| \boldsymbol{I} + \frac{P_{\mathrm{total}}}{M} \boldsymbol{H}^{\mathsf{H}} \boldsymbol{H} \right|. \tag{2.55}$$

We simplify the algorithm from [40] for single antenna UEs and obtain Algorithm 2.1. The algorithms first schedules the UE with the largest channel norm. Then it selects greedily one UE per iteration to maximize the sum rate (2.55). The channel vector of the scheduled UE is added to the matrix of the channel vectors of the already scheduled UEs. The selection of the UE which maximizes the sum rate (2.55) is reformulated as a selection rule which requires matrix inversions. The matrix inversions are calculated in a recursive way with the help of a matrix $\boldsymbol{\Omega}$. The algorithm terminates and returns the schedule $\mathcal{T}$ if the number $|\mathcal{T}_{\mathrm{temp}}|$ of scheduled UEs is equal to the number M of BS antennas, if all UEs are scheduled, or if the sum rate R_{temp} achieved in the actual BC reduces compared to the sum rate R_{last} in the actual BC in the previous step.

Other scheduling algorithms to select the UEs of a BC are described in [43–46].

Algorithm 2.1 Max Upper Bound Greedy Scheduling Algorithm [40]

$\mathcal{T}_{\text{unscheduled}} = \{1, 2, \ldots, K\}$ (set of unscheduled UEs)
$\mathcal{T} = \emptyset$ (set of scheduled UEs)
$\boldsymbol{\Omega} = \frac{P_{\text{total}}}{\sigma_N^2} \boldsymbol{I}_M$ (recursive initialization)
$R_{\text{last}} = 0$
for $i = 1$ **to** $\min(M, K)$ **do**
  $t = \arg \max_{t \in \mathcal{T}_{\text{unscheduled}}} \boldsymbol{h}_t^{\mathsf{H}} \boldsymbol{\Omega} \boldsymbol{h}_t$ (selection rule)
  $\mathcal{T}_{\text{temp}} = \mathcal{T} + \{t\}$
  Apply ZFBF on $\begin{bmatrix} \boldsymbol{h}_{\mathcal{T}(1)}^{\mathsf{H}} \\ \vdots \\ \boldsymbol{h}_{\mathcal{T}(|\mathcal{T}_{\text{temp}}|)}^{\mathsf{H}} \end{bmatrix}$ (channels of scheduled UEs)
  and determine effective channels $\left[\tilde{h}_{\mathcal{T}(1)}, \ldots, \tilde{h}_{\mathcal{T}(|\mathcal{T}_{\text{temp}}|)}\right]$ (see (2.31))
  $R_{\text{temp}} = \sum_{k \in \mathcal{T}_{\text{temp}}} \log_2 \left(1 + \frac{P_{\text{total}}}{|\mathcal{T}_{\text{temp}}| \sigma_N^2} \tilde{h}_k\right)$
  if $R_{\text{temp}} < R_{\text{last}}$ **then** (stop if rate decreases)
    return $\mathcal{T}$
  else (else update sets)
    $\mathcal{T} = \mathcal{T}_{\text{temp}}$
    $R_{\text{last}} = R_{\text{temp}}$
    $\mathcal{T}_{\text{unscheduled}} = \mathcal{T}_{\text{unscheduled}} - \{t\}$
  end if
  $\boldsymbol{\Omega} = \boldsymbol{\Omega} - \boldsymbol{\Omega} \frac{\boldsymbol{h}_t \boldsymbol{h}_t^{\mathsf{H}}}{1 + \boldsymbol{h}_t^{\mathsf{H}} \boldsymbol{\Omega} \boldsymbol{h}_t} \boldsymbol{\Omega}$ (recursive update)
end for

2.9. Massive MIMO

Massive MIMO is also know as “Very Large MIMO”, “Hyper MIMO”, “Full Dimension MIMO”, “Large-Scale Antenna Systems”, or “ARGOS” [5]. Massive MIMO refers to a “vast” over-provisioning of BS antennas as compared to the number of served single antenna UEs [4]. Hence the term massive MIMO is not clearly defined. Massive MIMO may refer to any MIMO configuration beyond the largest MIMO mode in the current Long Term Evolution (LTE) standard, at present eight BS antennas, for example, 100 antennas or more [15], or it may simply refer to a “large“ number of antennas at the BSs. A more precise definition of massive MIMO is based on the ratio M/K of serving BS antennas to the number of active UEs. However, the ratio M/K for which one can speak of massive MIMO depends on the performance metric, the scenario, etc. [6].

Massive MIMO claims several advantages over conventional MIMO [5]:

- ▷ *Massive MIMO increases capacity by 10 times or more and simultaneously increases energy efficiency.* The transmit signals are directed precisely to the UEs through precoding which reduces interference. Each additional antenna increases the precoding degrees-of-freedom assuming no mutual coupling and a sufficiently complex propagation environment [15]. Simple linear precoding has a vanishing gap to optimal precoding [4, 6, 15]. For instance, the performance gap between ZFBF and the optimal DPC vanishes with an increasing number of BS antennas. MRT is also asymptotically optimal as the number of BS antennas increases, but for a smaller number of BS antennas MRT performs well only in the low SNR regime [15]. In contrast increasing the spectral efficiency (SE) of regular BSs, for example, in LTE, by further sectorization is not feasible, while massive MIMO is scalable by adding more antennas [47].

- ▷ *Inexpensive, low-power components suffice.* A large number of BS antennas makes the system robust against noise, fading and hardware impairments or even failure of antennas. This allows simpler transmitters and receivers at the BS, for example, few or one bit quantization, hybrid digital-analog precoding, and constant envelope precoding [6,48]. New types of BSs architectures are possible, for example, one could imagine antenna arrays on the facade of buildings [47].

- ▷ *The multiple-access layer is simplified.* The channel hardens by the law of large numbers [5,15]. This means that all subcarriers of one UE experience similar channel gains. Hence scheduling does not improve performance because all UEs can be always active on all subcarriers. Only power control is needed to distribute the power across UEs depending on the slowly varying large-scale fading [6]. We analyze the channel hardening for our scenario in Section 5.6 and in Section 5.8.

- ▷ *The latency is reduced.* Since all UEs are always scheduled, UEs need not wait for good fading conditions.

- ▷ *Massive MIMO is robust to jamming and interference.* Given accurate CSI the BSs can use the surplus of precoding degrees-of-freedom to cancel interference or jamming.

Like in conventional MIMO, CSI is required to enable precoding. Acquiring CSI might be more difficult in massive MIMO due to the many antennas. Many publications suggest to use time division duplex (TDD) for massive MIMO, e.g., [4, 5, 15, 49]. In TDD the uplink and downlink use the same frequencies at different times. The UEs transmit pilot sequences from which the uplink channel is estimated. With TDD the downlink channel is immediately known due to channel reciprocity. The number of pilot sequences scales with the number of UEs and little feedback is required. This means that the overhead for CSI is independent of the number of BS antennas. If the correlation between the BS antennas is known the CSI quality improves with the number of BS antennas [6]. Note that codebook based open-loop precoding is suitable only for small arrays [6].

For frequency division duplex (FDD) the BS must send pilot sequences also. The number of pilot sequences scales with the number of BS antennas and the UEs then have to feedback the CSI to the BS which creates additional overhead [6]. However, FDD is mandatory for some frequency bands. Efficient FDD operation might still be possible [50].

With TDD other factors might limit communication [5]:

- ▷ While the channel is assumed to be reciprocal the hardware at the BS and UE might not be reciprocal. However, calibration of the hardware is possible [6].

- ▷ The pilot sequences assigned to the UEs should be orthogonal. However, the number of pilot sequences is constrained by the channel coherence time divided by the channel delay-spread. Hence the pilot sequences usually must be reused which leads to "pilot contamination" [4]. The BS estimates a linear combination of the channels of the UEs with the same pilot sequence. Hence the BS directs the signals not only to the intended UE but also to UEs with the same pilot sequence. This creates directed interference which increases with the number of BS antennas. Remedies exist, for example, optimized pilot sequence allocation, blind channel estimation, pilot contamination precoding, angle-of-arrival based methods, and protocol-based methods like time-shifted pilot schemes [5, 10, and references therein]. The number of BS antennas for massive MIMO such that channel estimation error and interference are small compared to "pilot contamination" is given in [49].

In order for massive MIMO to achieve its advantages with either TDD or FDD the channel vectors of the UEs must be sufficiently different [5]. Some works assume i.i.d. channel coefficients. However, in real scenarios the propagation environments are usually more difficult. The advantages of massive MIMO and a similar performance as with i.i.d. Rayleigh-fading channels are obtained in real measured channels [6,15,51]. Scheduling can improve performance in difficult environments, for example, by removing a few "worst" UEs [6]. The massive MIMO performance depends not only on the propagation environment but also on the antenna pattern (for example, directive antennas) and the mutual coupling between antennas. The negative effects of coupling can be compensated by matching

networks at the cost of ohmic losses and diminishing bandwidth [15]. Note that ZFBF and MMSE precoding approach the performance of i.i.d. channels faster than MRT and that 10 times more BS antennas than single antenna UEs should suffice to approach the ideal performance even in difficult propagation environments [5, 51]. We analyze the SE gain of different massive MIMO deployments with linear ZFBF precoding in Section 5.2 and compare it to a capacity upper bound in Section 5.5.

In [48, 52] the energy efficiency gain of massive MIMO systems is analyzed. The energy used by a BS is the sum of the radiated power and the circuit power consumption. The authors assume that for massive MIMO the circuit power consumption scales with the number M of BS antennas and with the number K of UEs. In contrast, the power consumption is often assumed constant for few of BS antennas. The optimization leads to the following insights: For energy efficient transmissions M and K are of the same order of magnitude, while $M > K$ still holds; and energy efficient transmissions operate in higher SNR regimes and suppress interference, for example, by ZFBF [48]. Depending on the scenario, distributed BSs with cooperation might achieve a higher energy efficiency than a single BS [52].

3

Cooperative and Non-Cooperative Transmission Schemes

AWGN has been the major limitation in cellular networks. However, interference is becoming more and more problematic. The SINR can be small due to inter-cell interference while the SNR is large [53]. Interference management is important for modern wireless communication standards like, LTE [54], and Long Term Evolution-Advanced (LTE-Advanced) [55], and for future standards like 5th generation mobile networks (5G). In most current wireless networks (for example, LTE, wireless local area network (WLAN)) the BSs or the access points do cooperate little or not at all. Reasons to avoid cooperation are limited backhaul capabilities, simpler network design and operation, or limiting technical specifications of wireless networks.

Several schemes that limit interference exist. One can categorize these schemes depending on the level of cooperation. Without any cooperation between BSs interference can be treated as noise only. If we allow only little and long term cooperation we can employ orthogonal resource reuse schemes, for example, frequency reuse. Interference coordination requires more and quicker cooperation. Compared to orthogonal resource reuse schemes capacity improves in proportion to the number of cells affected by the interference from a BS [56]. Even more cooperation is required for network MIMO where all BSs act as one BS. The latter two schemes are forms of coordinated multipoint (CoMP). Relays can also aid to treat interference besides improving the communication between BSs and UEs [56]. However, relay-assisted cooperation is not in the scope of this work.

A general framework and optimization algorithms for multi-cell scenarios with different levels of cooperation are presented in [12]. Interference balancing for quality-of-service (QoS) constraints is described in [57]. However, we are interested in transmission schemes

with low computational complexity. We describe the categories of cooperative schemes and our implementations in the following. For ease of notation we describe the principle for a single subcarrier and omit the subcarrier index $^{(f)}$. Combinations of schemes are also possible.

3.1. No Cooperation

Non-cooperative BSs determine the transmit signals and the scheduled UEs locally. They treat interference as additional noise and thus the interference limits reliable transmission in many scenarios. As a result, backhaul requirements are low and only local CSI is required.

Suppose the k-th UE is served by the $\hat{i}$-th BS with the maximum average SNR

$$\hat{i} = \arg\max_{i} \frac{1}{M_i N_{\mathrm{SC}}} \sum_{f=1}^{N_{\mathrm{SC}}} \left\| \boldsymbol{h}_{i,k}^{(f)} \right\|_1 \tag{3.1}$$

where $\boldsymbol{h}_{i,k}^{(f)}$ is the conjugate transpose of the vector of channel coefficients from the i-th BS to the k-th UE on the f-th subcarrier. The number of UEs served by the i-th BS is K_i. Without loss of generality (w.l.o.g.) we assume that the first K_1 UEs are served by the first BS, the next K_2 UEs are served by the second BS, and so on. Hence the indices of the UEs served by the i-th BS are

$$\mathcal{K}_i = \left\{ \sum_{j=1}^{i-1} K_j + 1, \ldots, \sum_{j=1}^{i} K_j \right\} = \left\{ \sum_{j=1}^{i-1} K_j + \{1, \ldots, K_j\} \right\}. \tag{3.2}$$

The vector of symbols intended for the UEs served by the i-th BS is $\boldsymbol{s}_i$. We collect the vectors of channel coefficients from the i-th BS to the UEs served by the j-th BS (with indices $\mathcal{K}_j$) in

$$\boldsymbol{H}_{i,j}^{\mathsf{H}} = \begin{bmatrix} \boldsymbol{h}_{i,\mathcal{K}_j(1)}^{\mathsf{H}} \\ \vdots \\ \boldsymbol{h}_{i,\mathcal{K}_j(K_j)}^{\mathsf{H}} \end{bmatrix} \in \mathbb{C}^{K_j \times M_i}. \tag{3.3}$$

The channel matrix of the channel coefficients from all N_{BS} BSs to all UEs is hence composed as

$$\boldsymbol{H}^{\mathsf{H}} = \begin{bmatrix} \boldsymbol{H}_{1,1}^{\mathsf{H}} & \boldsymbol{H}_{2,1}^{\mathsf{H}} & \cdots & \boldsymbol{H}_{N_{\mathrm{BS}},1}^{\mathsf{H}} \\ \boldsymbol{H}_{1,2}^{\mathsf{H}} & \boldsymbol{H}_{2,2}^{\mathsf{H}} & \cdots & \boldsymbol{H}_{N_{\mathrm{BS}},2}^{\mathsf{H}} \\ \vdots & \vdots & \ddots & \vdots \\ \boldsymbol{H}_{1,N_{\mathrm{BS}}}^{\mathsf{H}} & \boldsymbol{H}_{2,N_{\mathrm{BS}}}^{\mathsf{H}} & \cdots & \boldsymbol{H}_{N_{\mathrm{BS}},N_{\mathrm{BS}}}^{\mathsf{H}} \end{bmatrix}. \tag{3.4}$$

We define local CSI at the i-th BS as the channel matrix to the UEs served by the i-th BS $\boldsymbol{H}_{i,i}^{\mathsf{H}}$ being available. In contrast global CSI refers to the case where $\boldsymbol{H}^{\mathsf{H}}$ is available (see

Figure 3.3).

For no cooperation the precoding function determines the local transmit signal vector $\boldsymbol{x}_i$ based on local CSI. The precoding function of the i-th BS is

$$\boldsymbol{x}_i = w_i\left(\boldsymbol{s}_i, \boldsymbol{H}_{i,i}^{\mathsf{H}}\right). \tag{3.5}$$

For ease of notation we state the precoding function for a single subcarrier. Note that a BS determines its transmit signals on all subcarriers jointly. The transmit signals of the whole network are composed as

$$\boldsymbol{x} = \begin{bmatrix} \boldsymbol{x}_1 \\ \vdots \\ \boldsymbol{x}_{N_{\mathrm{BS}}} \end{bmatrix} = \begin{bmatrix} w_1\left(\boldsymbol{s}_1, \boldsymbol{H}_{1,1}^{\mathsf{H}}\right) \\ \vdots \\ w_{N_{\mathrm{BS}}}\left(\boldsymbol{s}_{N_{\mathrm{BS}}}, \boldsymbol{H}_{N_{\mathrm{BS}},N_{\mathrm{BS}}}^{\mathsf{H}}\right) \end{bmatrix} = w\left(\boldsymbol{s}, \boldsymbol{H}^{\mathsf{H}}\right). \tag{3.6}$$

The linear precoding vector for the k-th UE is

$$\boldsymbol{w}_k^{\mathsf{T}} = \big[\underbrace{\boldsymbol{w}_{1,k}^{\mathsf{T}}, \ldots, \boldsymbol{w}_{i-1,k}^{\mathsf{T}}}_{=\boldsymbol{0}}, \boldsymbol{w}_{i,k}^{\mathsf{T}}, \underbrace{\boldsymbol{w}_{i+1,k}^{\mathsf{T}}, \ldots, \boldsymbol{w}_{N_{\mathrm{BS}},k}^{\mathsf{T}}}_{=\boldsymbol{0}}\big] \tag{3.7}$$

where $\boldsymbol{w}_{j,k} \in \mathbb{C}^{M_j}$ is the part of precoding vector containing the precoding weights for the antennas at the j-th BS. The precoding weights are zero except $\boldsymbol{w}_{i,k}$ at the i-th BS which serves the k-th UE. Recall that $\boldsymbol{W} = [\boldsymbol{w}_1, \ldots, \boldsymbol{w}_K]$. Hence the linear precoding matrix has a block-diagonal structure

$$\boldsymbol{x} = \boldsymbol{W}\boldsymbol{s} = \begin{bmatrix} \boldsymbol{W}_1 & \boldsymbol{0} & \cdots & \boldsymbol{0} \\ \boldsymbol{0} & \boldsymbol{W}_2 & \ddots & \vdots \\ \vdots & \ddots & \ddots & \boldsymbol{0} \\ \boldsymbol{0} & \cdots & \boldsymbol{0} & \boldsymbol{W}_{N_{\mathrm{BS}}} \end{bmatrix} \boldsymbol{s} \tag{3.8}$$

where

$$\boldsymbol{W}_i = \left[\boldsymbol{w}_{i,\mathcal{K}_i(1)}, \ldots, \boldsymbol{w}_{i,\mathcal{K}_i(K_i)}\right] \in \mathbb{C}^{M \times K_i} \tag{3.9}$$

is the precoding matrix at the i-th BS determined from local CSI $\boldsymbol{H}_{i,i}^{\mathsf{H}}$.

The SINR achieved at the k-th UE served by the i-th BS with linear precoding and treating interference as noise is

$$\mathrm{SINR}_k^{\text{No Cooperation}} = \frac{\left|\boldsymbol{h}_k^{\mathsf{H}}\boldsymbol{w}_k\right|^2}{\sum\limits_{\substack{l=1 \\ l\neq k}}^{K}\left|\boldsymbol{h}_k^{\mathsf{H}}\boldsymbol{w}_l\right|^2 + \sigma_N^2} = \frac{\left|\boldsymbol{h}_{i,k}^{\mathsf{H}}\boldsymbol{w}_{i,k}\right|^2}{\underbrace{\sum\limits_{\substack{l\in\mathcal{K}_i \\ l\neq k}}\left|\boldsymbol{h}_{i,k}^{\mathsf{H}}\boldsymbol{w}_{i,l}\right|^2}_{\text{Intra-cell interference}} + \underbrace{\sum\limits_{\substack{j=1 \\ j\neq i}}^{N_{\mathrm{BS}}}\sum\limits_{l\in\mathcal{K}_j}\left|\boldsymbol{h}_{j,k}^{\mathsf{H}}\boldsymbol{w}_{j,l}\right|^2}_{\text{Inter-cell interference}} + \sigma_N^2}. \tag{3.10}$$

Intra-cell interference is the interference created by the transmissions to other UEs served by the same BS. Inter-cell is the interference created by the transmissions by other BSs which do not serve the UE.

As we know from Section 2.4.2 interference is mitigated by ZFBF. Without cooperation we can mitigate only intra-cell interference

$$\boldsymbol{h}_{i,k}^{\mathsf{H}} \boldsymbol{w}_{i,l} = 0, \qquad \forall l \in \mathcal{K}_i, l \neq k \tag{3.11}$$

while we cannot influence inter-cell interference due to unavailable CSI. ZFBF requires that the i-th BS serves at most M_i UEs, i.e., we have $K_i \leq M_i$. If $K_i > M_i$ then we use the low complexity scheduling algorithm from [40] described in Section 2.8 to select M_i UEs and define $\mathcal{K}_i$ as the set of scheduled UEs. For ease of notation the channel matrices do not include the unscheduled UEs in (3.12)-(3.15). The SINR of the unscheduled UEs is zero. Note that the set of scheduled UEs may be different on each subcarrier. ZFBF is accomplished at the i-th BS by the pseudo-inverse of the local channel matrix $\boldsymbol{H}_{i,i}^{\mathsf{H}}$ combined with power allocation

$$\boldsymbol{W}_i = \boldsymbol{H}_{i,i}^{\dagger} \operatorname{diag}\left(\tilde{\boldsymbol{p}}_i\right)^{\frac{1}{2}} = \boldsymbol{H}_{i,i} \left(\boldsymbol{H}_{i,i}^{\mathsf{H}} \boldsymbol{H}_{i,i}\right)^{-1} \operatorname{diag}\left(\tilde{\boldsymbol{p}}_i\right)^{\frac{1}{2}} \tag{3.12}$$

where

$$\tilde{\boldsymbol{p}}_i = \left[\tilde{p}_{i,\mathcal{K}_i(1)}, \ldots, \tilde{p}_{i,\mathcal{K}_i(K_i)}\right] \in \mathbb{C}^{K_i} \tag{3.13}$$

is the power allocation vector at the i-th BS. We use mercury/water-filling as described in Section 2.6 at each BS to allocate power according to a per-BS power constraint. The SINRachieved at the k-th UE is

$$\mathrm{SINR}_k^{\text{local precoding}} = \frac{\left|\boldsymbol{h}_{i,k}^{\mathsf{H}} \boldsymbol{w}_{i,k}\right|^2}{\sum\limits_{\substack{j=1 \\ j \neq i}}^{N_{\mathrm{BS}}} \sum\limits_{l \in \mathcal{K}_j} \left|\boldsymbol{h}_{j,k}^{\mathsf{H}} \boldsymbol{w}_{j,l}\right|^2 + \sigma_N^2} = \frac{\tilde{p}_{i,k}^{\text{local precoding}}}{\sum\limits_{\substack{j=1 \\ j \neq i}}^{N_{\mathrm{BS}}} \sum\limits_{l \in \mathcal{K}_j} \left|\boldsymbol{h}_{j,k}^{\mathsf{H}} \boldsymbol{w}_{j,l}\right|^2 + \sigma_N^2}. \tag{3.14}$$

We call the presented non cooperative scheme *local precoding*. Figure 3.1 shows the system model of local precoding.

3.2. Orthogonal Resource Reuse

The inter-cell interference is reduced when groups of BS use orthogonal spectral resources which is called frequency reuse. Other orthogonal resources include orthogonal time slots and orthogonal spreading codes. Orthogonal resource reuse schemes are static cooperation schemes which operate on a long time scale. The backhaul requirements are hence very low.

Only BSs sharing the same resource cause inter-cell interference. Choosing the BS groups such that the distances between BSs of the same group are maximal reduces inter-

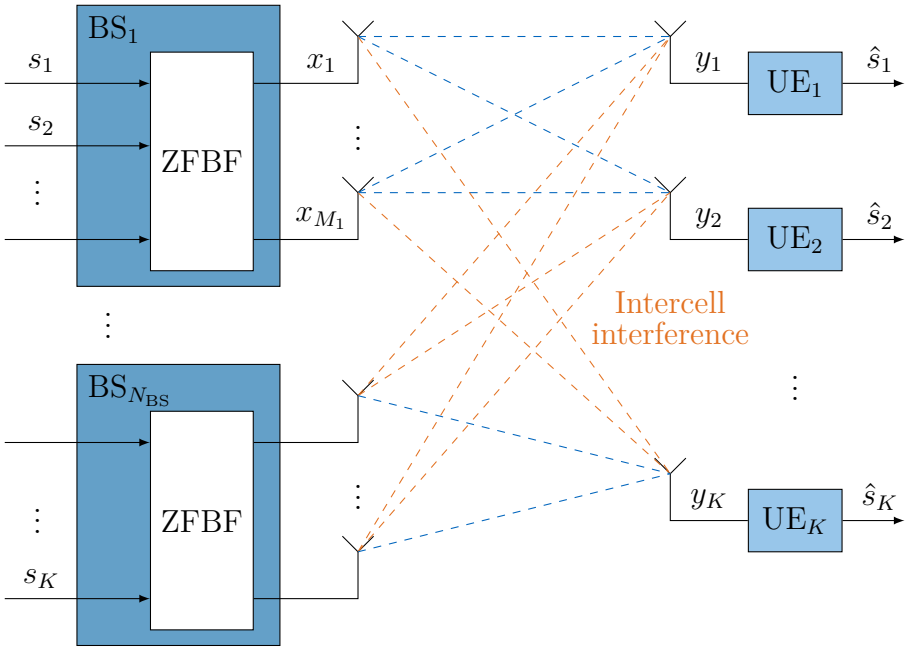

Figure 3.1.: System model for local precoding.

cell interference. However, each BS group uses only a fraction of the available resources which reduces the performance [58]. Often the average performance and especially the peak performance are worse compared to local precoding. The SINR with reuse at the k-th UE is

$$\mathrm{SINR}_k^{\text{orthogonal reuse}} = \frac{\tilde{p}_{i,k}^{\text{orthogonal reuse}}}{\sum\limits_{\substack{j \in \mathcal{G}_i \\ j \neq i}} \sum\limits_{l \in \mathcal{K}_j} \left| \boldsymbol{h}_{j,k}^{\mathsf{H}} \boldsymbol{w}_{j,l} \right|^2 + \sigma_N^2} \tag{3.15}$$

where $\mathcal{G}_i$ is the set of indices of BSs group sharing the same resources as the i-th BS. We consider orthogonal time slots as an example reuse scheme and call it *orthogonal reuse*. The system model of orthogonal reuse per group of BSs is the same as for local precoding in Figure 3.1.

Adaptive reuse improves performance but has higher requirements on the backhaul. Adaptive reuse might be considered an interference coordination scheme, as described in the next section.

With soft handover, cell-edge UEs are served simultaneously by different BSs on orthogonal resources. This improves the performance and coverage, but inter-cell interference is still limiting [56].

3.3. Interference Coordination

Interference coordination has each BS estimate its channels to all UEs, and each BS exchange its CSI with the other BSs. The resulting global CSI lets us coordinate the transmissions of the BSs, for example, by power allocation, precoding, and scheduling. This way interference is mitigated. Still each UE is served by a single BS. At a BS only the messages dedicated to the UEs served by the BS are available. The backhaul requirements are modest and a signal-level synchronization of the BSs is not needed [56].

The set $\mathcal{K}_i$ of the K_i UEs served by the i-th BS is determined based on maximal SNR as for no cooperation (3.1). For interference coordination the i-th BS estimates its channels to all UEs

$$\boldsymbol{H}_i^{\mathsf{H}} = \begin{bmatrix} \boldsymbol{H}_{i,1}^{\mathsf{H}} \\ \boldsymbol{H}_{i,2}^{\mathsf{H}} \\ \vdots \\ \boldsymbol{H}_{i,N_{\mathrm{BS}}}^{\mathsf{H}} \end{bmatrix}. \tag{3.16}$$

In contrast, for no cooperation the i-th BS estimates only its channels $\boldsymbol{H}_{i,i}^{\mathsf{H}}$ to the UEs it serves. The BSs exchange their CSI $\boldsymbol{H}_i^{\mathsf{H}}$ such that the global CSI $\boldsymbol{H}^{\mathsf{H}}$ is available at all BSs. The precoding function of the i-th BS is

$$\boldsymbol{x}_i = w_i\left(\boldsymbol{s}_i, \boldsymbol{H}^{\mathsf{H}}\right). \tag{3.17}$$

Again we state the precoding function for a single subcarrier for ease of notation. Note that the transmit signals on all subcarriers are determined jointly. This is particularly important to exploit the degrees-of-freedom while scheduling to coordinate interference. The transmit signals are composed as

$$\boldsymbol{x} = \begin{bmatrix} \boldsymbol{x}_1 \\ \vdots \\ \boldsymbol{x}_{N_{\mathrm{BS}}} \end{bmatrix} = \begin{bmatrix} w_1\left(\boldsymbol{s}_1, \boldsymbol{H}^{\mathsf{H}}\right) \\ \vdots \\ w_{N_{\mathrm{BS}}}\left(\boldsymbol{s}_{N_{\mathrm{BS}}}, \boldsymbol{H}^{\mathsf{H}}\right) \end{bmatrix} = w\left(\boldsymbol{s}, \boldsymbol{H}^{\mathsf{H}}\right). \tag{3.18}$$

Note that the only difference to the precoding functions with no cooperation is the available CSI. Consequently the linear precoding matrix has the same block-diagonal structure as in (3.8) but the precoding matrix at the i-th BS $\boldsymbol{W}_i$ is determined based on global CSI instead of local CSI. The SINR is determined as for no cooperation in (3.10). However, coordination allows to reduce both the intra-cell and the inter-cell interference.

The coordination can be accomplished at a central processor or locally at the BSs. The distributed, local coordination can be realized in a competitive (game theoretic) way or with the help of control messages over the backhaul. Note that to reduce the backhaul requirements some coordination schemes exchange little or no CSI and some schemes exchange control messages instead.

The coordination schemes can be categorized into different types:

- ▷ *Coordinated scheduling (CS)* has the scheduling and power allocation optimized jointly by all BSs. CS can increase sum rate compared to no cooperation. However, a convex formulation is unknown to most CS optimization problems [56]. A promising idea is interference pricing [56, and the references therein]. Each BS measures the impact of its own transmission on the other BSs's transmissions. The goal is to minimize this measure. CS is also called *coordinated power control*.

- ▷ *Coordinated beamforming (CB)* has the precoding coordinated using available precoding degrees-of-freedom to reduce interference. With increasing precoding degrees-of-freedom more interference can be canceled until an interference zero-forcing solution is possible when the precoding degrees-of-freedom are at least as large as the number of interferers.

- ▷ The combination of CS and CB, which is called *coordinated scheduling/coordinated beamforming (CS/CB)*, is more common than pure CB. Here again convex optimization formulations are unknown in general [56]. An uplink-downlink duality allows to solve multi-cell power minimization problems. There is a dual problem formulation but the maximization of the achievable rate region is often difficult [59].

- ▷ For CS, CB, and CS/CB interference is treated as noise. Performance can improve if interference is detected at the UEs [56]. *Coding for interference mitigation* helps to detect and treat interference at the UEs. The idea is to split messages into private and common parts. The common parts are decoded by all UEs and are canceled at the UEs to subtract interference. The private parts are transmitted with less power and hence can be decoded only at the intended UEs.

- ▷ Another form of coding for interference mitigation is *interference alignment (IA)* [60]. The main idea of IA is to code the signal at the BSs such that interference aligns at each UE in a subspace. The orthogonal subspace is used for interference-free communication. The space can be spanned by MIMO antennas, by different channel realizations, by lattice coding [60], or by carefully chosen subcarrier pairs [61].

3.3.1. Large-Scale MIMO

We consider *large-scale MIMO (LS-MIMO)* [62] as an example of an interference coordination scheme. LS-MIMO is a linear CB scheme which does not exchange CSI or control messages over the backhaul. However, the i-th BS still estimates its channels to all UEs. Sufficiently many antennas are required at each BS to allow the following. Each BS uses ZFBF to mitigate the interference created at all UEs and thereby creates parallel interference-free channels to the UEs it serves. Figure 3.2 shows the system model of LS-MIMO.

The goal of LS-MIMO is to zero-force all interference from the transmissions of the i-th BS

$$\boldsymbol{h}_{i,k}^{\mathsf{H}} \boldsymbol{w}_{i,l} = 0, \qquad \forall i \in \{1, \ldots, N_{\mathrm{BS}}\}, l \in \mathcal{K}_i, l \neq k. \tag{3.19}$$

This is feasible if the matrix of the channel coefficients from the antennas of the i-th BS to all UEs $\boldsymbol{H}_i^{\mathsf{H}}$ has rank satisfying

$$\operatorname{rank}\left(\boldsymbol{H}_i^{\mathsf{H}}\right) \geq K = \sum_{i=1}^{N_{\mathrm{BS}}} K_i. \tag{3.20}$$

For our channel model this means that the number of antennas M_i at the i-th BS must satisfy

$$M_i \geq K. \tag{3.21}$$

Hence LS-MIMO is feasible for the complete system if

$$M = \sum_{i=1}^{N_{\mathrm{BS}}} M_i \geq \sum_{i=1}^{N_{\mathrm{BS}}} K = N_{\mathrm{BS}} K. \tag{3.22}$$

In contrast to local precoding each BS estimates its channels to all UEs $\boldsymbol{H}_i^{\mathsf{H}}$ (see Figure 3.3). Then the i-th BS uses the pseudo-inverse of the channel matrix $\boldsymbol{H}_i^{\mathsf{H}}$ combined with a power allocation to zero force all interference and to create parallel interference-free channels to its K_i UEs:

$$\boldsymbol{W}_i = \boldsymbol{H}_i^{\dagger} \boldsymbol{K} \operatorname{diag}\left(\tilde{\boldsymbol{p}}_i\right)^{\frac{1}{2}} = \boldsymbol{H}_i \left(\boldsymbol{H}_i^{\mathsf{H}} \boldsymbol{H}_i\right)^{-1} \boldsymbol{K} \operatorname{diag}\left(\tilde{\boldsymbol{p}}_i\right)^{\frac{1}{2}} \tag{3.23}$$

where $\boldsymbol{K} = \left[\mathbf{0}_{K_i, \sum_{j=1}^{i-1} K_j} \boldsymbol{I}_{K_i} \mathbf{0}_{K_i, \sum_{j=i+1}^{N_{\mathrm{BS}}} K_j}\right]$ chooses the precoding vectors of the UEs $\mathcal{K}_i$ and $\tilde{\boldsymbol{p}}_i$ is the power allocation vector at the i-th BS as defined in (3.13).

We again use mercury/water-filling as described in Section 2.6 to allocate power according to a per-BS power constraint. The SINR with LS-MIMO is determined as for local precoding in (3.14) but all interference is mitigated:

$$\mathrm{SINR}_k^{\text{LS-MIMO}} = \frac{\left|\boldsymbol{h}_k^{\mathsf{H}} \boldsymbol{w}_k\right|^2}{\sum\limits_{\substack{l=1 \\ l \neq k}}^{K} \left|\boldsymbol{h}_k^{\mathsf{H}} \boldsymbol{w}_l\right|^2 + \sigma_N^2} = \frac{\left|\boldsymbol{h}_{i,k}^{\mathsf{H}} \boldsymbol{w}_{i,k}\right|^2}{\underbrace{\sum\limits_{j=1}^{N_{\mathrm{BS}}} \sum\limits_{\substack{l \in \mathcal{K}_j \\ l \neq k}} \left|\boldsymbol{h}_{j,k}^{\mathsf{H}} \boldsymbol{w}_{j,l}\right|^2}_{\text{Interference}} + \sigma_N^2} = \frac{\tilde{p}_{i,k}^{\text{LS-MIMO}}}{\sigma_N^2}. \tag{3.24}$$

Note that local precoding requires

$$M_i \geq K_i \tag{3.25}$$

antennas at each BS, while LS-MIMO requires

$$M_i \geq K \tag{3.26}$$

antennas at each BS. However, local precoding creates interference at the UEs of the other BSs.

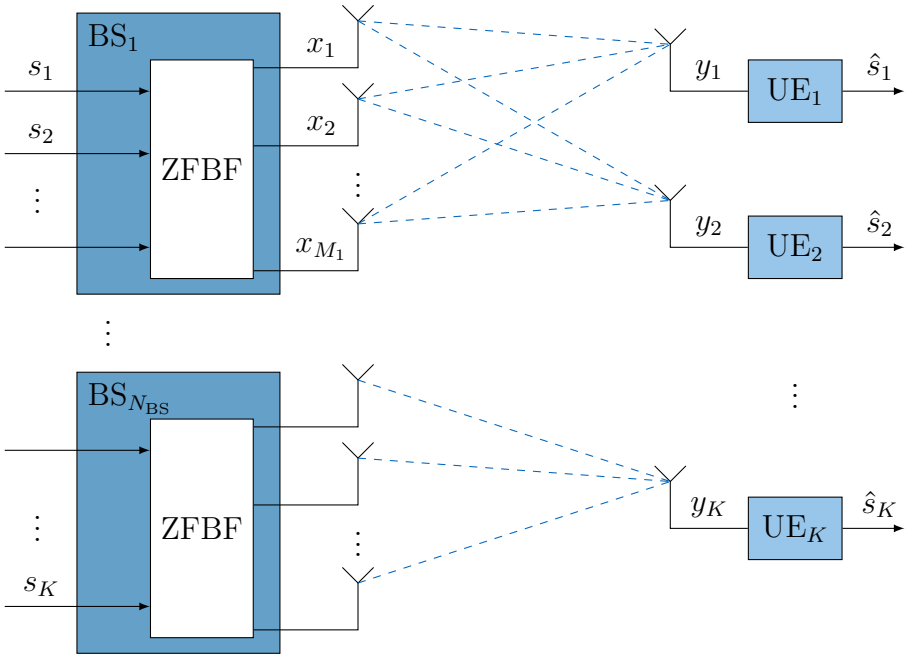

Figure 3.2.: System model for LS-MIMO.

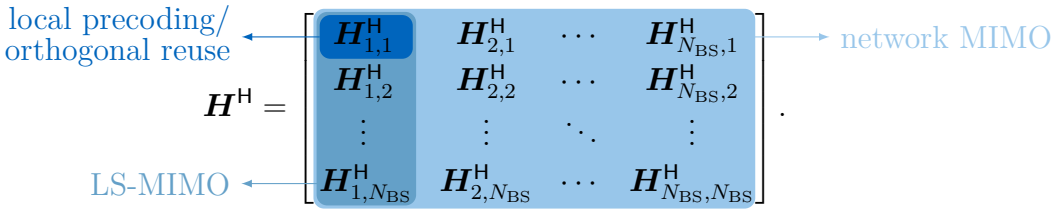

Figure 3.3.: Requied CSI knowledge of the first BS for the different transmission schemes.

Massive MIMO approaches the zero-forcing behavior of LS-MIMO with increasing M_i as the channels to the UEs of the other BSs become orthogonal to the channels to the served UEs [62].

Note that LS-MIMO can be made feasible by scheduling a subset of UEs, for example, as in Section 2.8. However, we analyze LS-MIMO only if (3.26) is fulfilled.

A generalization of LS-MIMO and local precoding is full-pilot zero-forcing (P-ZF) combining [63]. Here a BS estimates the channels to a subset of the UEs (to control the number of pilots) and mitigates interference to all UEs with known channels. If the channels to all UEs $\boldsymbol{H}_i$ are known P-ZF equals LS-MIMO. If only the channels to the UEs served by a BS $\boldsymbol{H}_{i,i}$ are known P-ZF equals local precoding.

3.4. Network MIMO

Network MIMO requires that the BSs are connected by a backhaul with low delay and high throughput. Also the BSs must be synchronized. The distributed BSs act as one BS with distributed antennas and the downlink channel becomes a BC. In contrast to interference coordination, network MIMO may have interference enhance the signals at the UEs.

Network MIMO can be realized in different ways:

- ▷ The BSs sends their CSI $\boldsymbol{H}_i^{\mathsf{H}}$ (the channels to all UEs) to a central processor. At the central processor the gathered global CSI and the messages for all UEs are available. The central processor treats the distributed BSs as one BS with distributed antennas and determines the transmit signals at the BSs. The BSs are sometimes called "Remote Radio Heads".

- ▷ The BSs exchange the messages of the UEs and their CSI $\boldsymbol{H}_i^{\mathsf{H}}$. The transmit signals are determined in a distributed fashion with the help of control messages or by decentralized algorithms.

- ▷ Each central processor is connected to a group of BSs. The central processors exchange CSI and messages to determine the transmit signals in a distributed fashion.

For network MIMO we assume a perfect backhaul with unlimited capacity and zero delay. We let all BSs act as a single BS with distributed antennas. This allows to apply ZFBF as described in Section 2.4.2 without any constraints on the structure of the precoding matrix $\boldsymbol{W}$. However, we consider single BSs constrained by per-BS power constraints. The classical MAC-BC duality does not determine the optimal precoder for per-BS power constraints [56]. We use a low-complexity approach to obtain a suboptimal precoding matrix for network MIMO with per-BS power constraints. First we determine for each subcarrier the precoding matrix $\boldsymbol{W}$ using ZFBF. Then we use mercury/water-filling as described in Section 2.6 to allocate power according to a total power constraint

$$\sum_{f=1}^{N_{\mathrm{SC}}} \mathbb{E}\left[\left\|\boldsymbol{x}^{(f)}\right\|_2^2\right] \leq \sum_{i=1}^{N_{\mathrm{BS}}} P_i. \tag{3.27}$$

Next, we determine the transmit power at each BS

$$P_i^{\text{tx Pw}} = \sum_{f=1}^{N_{\mathrm{SC}}} \mathbb{E}\left[\left\|\boldsymbol{x}_i^{(f)}\right\|_2^2\right]. \tag{3.28}$$

Finally we scale the precoding matrix $\boldsymbol{W}$ with

$$\gamma = \sqrt{\frac{P_i}{\max_i P_i^{\text{tx Pw}}}}. \tag{3.29}$$

The scaling factor γ ensures that the per-BS power constraint is satisfied at all BSs

$$\gamma^2 P_i^{\text{tx Pw}} \leq P_i, \qquad \forall i \in \{1, \ldots, N_{\text{BS}}\} \tag{3.30}$$

where the inequality is tight at least at one BS. However, some BSs could transmit with higher power. Hence this is a suboptimal approach, and better approaches can be found for per-BS power constraints [64, 65] or for per-antenna power constraints [16, 66]. We analyze the performance difference between a total power and a per-BS power constrained network MIMO transmission scheme in Section 5.5. Recall that ZFBF is a linear precoding scheme. Nonlinear precoding schemes like DPC improve performance [53]. The SINR of network MIMO is

$$\text{SINR}_k^{\text{network MIMO}} = \frac{\left|\gamma \boldsymbol{h}_k^{\mathsf{H}} \boldsymbol{w}_k\right|^2}{\sum\limits_{\substack{l=1 \\ l \neq k}}^{K} \left|\gamma \boldsymbol{h}_k^{\mathsf{H}} \boldsymbol{w}_l\right|^2 + \sigma_N^2} = \frac{\gamma^2 \tilde{p}_{i,k}^{\text{network MIMO}}}{\sigma_N^2}. \tag{3.31}$$

Figure 3.4 shows the system model of network MIMO. Note the similarities to the system model of a deployment with a single BS in Figure 3.5.

Network MIMO helps to avoid rank deficient and poorly conditioned channel matrices which are caused by spatial correlations or by the "keyhole" effect [67].

Network MIMO is sometimes called "distributed MIMO", "MIMO cooperation", "coherently coordinated transmission", "Joint Processing CoMP", "Joint Transmission CoMP", "C-RAN (Cloud-RAN)" or "p-cell" [68].

3.4.1. Rate Limited Network MIMO

If the backhaul cannot exchange all UE messages, it is still beneficial to exchange CSI and part of the UE messages [56]. Rate limited network MIMO is not in the scope of this work.

3.5. Cooperation Clusters

While it is most beneficial if all BSs of a communication network cooperate, it is usually impossible in real networks. The backhaul traffic would require a large bandwidth, it would be costly to obtain CSI of the complete network, and delay constraints for the backhaul and for the cooperation algorithms would be very tight. A single central controller has the additional drawback of being a single point of failure. Hence efficient CSI representations, decentralized cooperation algorithms, and cooperation limited to cooperation clusters are relevant for practical implementations [56]. Example decentralized cooperation algorithms are turbo base stations, game theoretic models, and team decision theory approaches. Cooperation clusters fit well to current communication networks. They reduce the complexity of cooperation algorithms and require less backhaul traffic, as less BSs and UEs are involved to cooperate within each cluster. However, inter-cluster interference remains. There

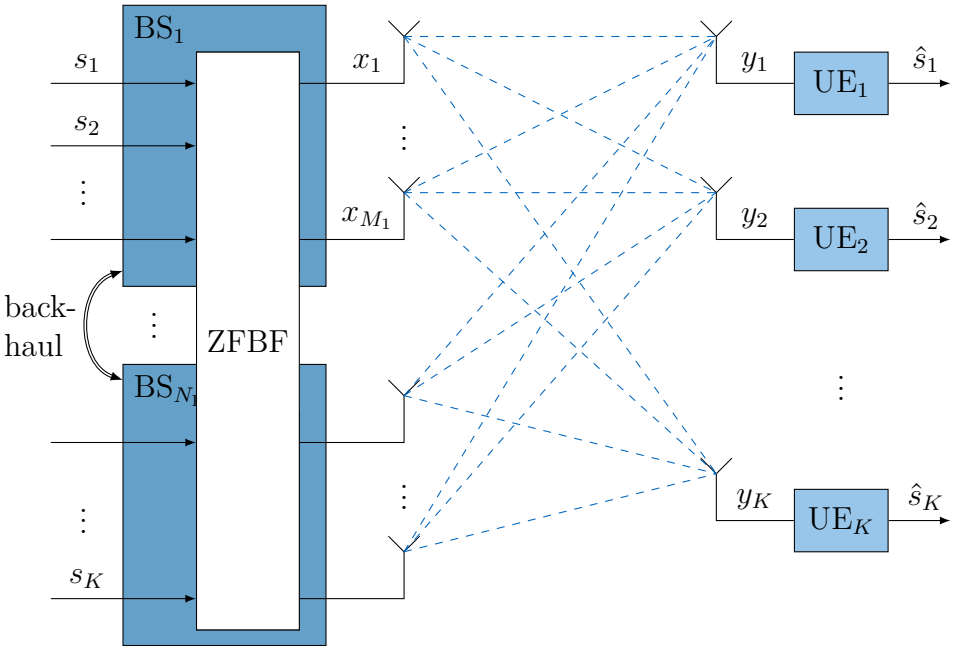

Figure 3.4.: System model for network MIMO.

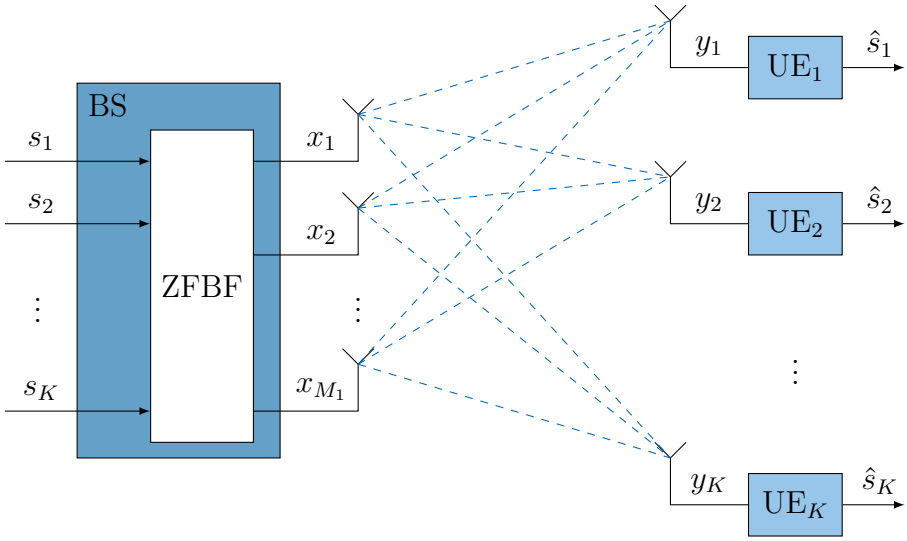

Figure 3.5.: System model for a single BS.

are several approaches to limit the impact of inter-cluster interference, see [56, 69, and references within]. The size of the cooperation clusters is a trade-off between the overhead of coordinating the transmissions to more UEs and the number of cell-edge UEs [70]. The gain of cooperation clusters versus massive MIMO in an outdoor cell without shadowing is analyzed in [71], for example.

4

Channel Model, Scenario, and Deployments

We aim to compare different BS deployments in a realistic scenario. We use the Quasi Deterministic Radio Channel Generator (QuaDRiGa) channel model to generate channel coefficients for the 3rd Generation Partnership Project (3GPP) indoor office scenario. In this chapter we present the QuaDRiGa channel model, the 3GPP indoor office scenario, and the base station deployments.

4.1. QuaDRiGa

QuaDRiGa [72, 73] is an open-source 3GPP-3D channel model reference implementation, which was developed at the Fraunhofer Heinrich Hertz Institute (HHI). The 3GPP-3D channel model is the latest evolution of 3GPP geometry-based stochastic channel models. It is based on the initial 3GPP spatial channel model (SCM) and it succeeds the channel models of Wireless World Initiative New Radio (WINNER), Wireless World Initiative New Radio II (WINNER II) and Wireless World Initiative New Radio+ (WINNER+). QuaDRiGa fulfills the requirements of the mentioned geometry-based stochastic channel models. Hence we can use QuaDRiGa to generate channel realizations according to the WINNER II and WINNER+ channel model specifications and parameters.

QuaDRiGa has the following features (besides other features) which are relevant for our analysis:

- ▷ Support of frequencies between 2 GHz and 6 GHz,
- ▷ Support of multi-user MIMO,

- ▷ 3D propagation environment models,
- ▷ Support of massive MIMO,
- ▷ Same modeling approach for indoor, outdoor and combined indoor-outdoor environments,
- ▷ Common framework for line-of-sight (LOS) and non line-of-sight (NLOS) conditions,
- ▷ Improved correlation of large-scale parameters.

The pathloss between BSs and UEs is determined based on the geometric distance in Quadriga and we enhance our simulations to count the number of walls to be able to add the wall penetration loss. However, scattering clusters are distributed randomly in the vicinity of each BS and UE for each channel realization. A scattering cluster consists of 20 individual scatters. Each individual scatter or sub-path is modeled by a single reflection. The scatterer of a cluster can be resolved in the spatial domain as their angles of departure and angles of arrival differ sufficiently. However, they cannot be resolved in the time-domain. Hence they are combined into a single signal which is called path, tap, or multi-path component. When determining the channel coefficients, the angles of departure and arrival are determined for each sub-path while path length and hence the delay is determined per scattering cluster. The number of scattering clusters depends on the scenario. The random positioning of the scattering clusters is determined by the angular spread and the delay spread which are determined by the large-scale parameters of the scenario. The large-scale parameters define the statistical distributions of channel parameters like delay spread, delay values, path power, angle spread, angles-of-departure, angles-of-arrival, shadow fading, and cross-polarization. The large-scale parameters of a scenario are derived from measurement campaigns.

4.2. Scenario

We consider the indoor office scenario defined as “A1 - Indoor Office” in the WINNER II deliverable D.1.1.2 [74]. Figure 4.1 shows the layout of the office building. One floor of the office building consists of two corridors and 20 identical offices adjacent to each corridor. The channel parameters are valid for frequencies between 2 GHz and 5 GHz [75]. We consider BS deployments inside and outside the building while the UEs are located 1.5 m above the floor inside the building. Hence we use indoor channel parameters and outdoor-to-indoor channel parameters.

4.2.1. Indoor-to-Indoor Parameters

The indoor large-scale parameters are the “A1 - Indoor Office” channel model parameters defined in WINNER II deliverable D.1.1.2 [74]. There are two sets of parameters: One for LOS and one for NLOS conditions. For NLOS conditions a wall penetration loss is

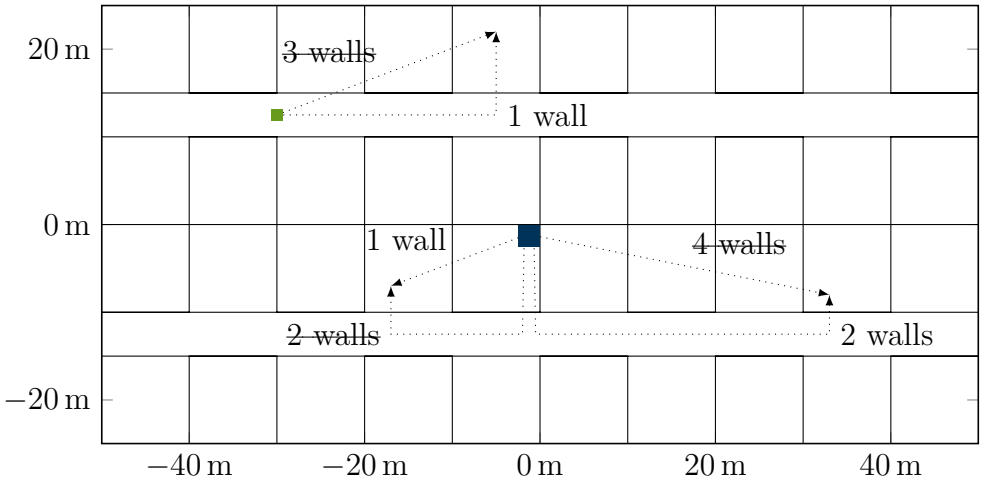

Figure 4.1.: Layout, and wall counting examples in the indoor office scenario defined in [74].

added, where the wall penetration loss is determined by counting the number of walls between each BS and UE. When counting the number of walls, paths along the corridors are considered as alternatives to the direct path, which might penetrate more walls. Figure 4.1 shows wall counting examples.

The model considers heavy and light walls. The loss for every wall beyond the first wall is 12 dB for heavy walls and 5 dB for light walls. For no walls the LOS parameters are used, otherwise NLOS parameters are used and we add the wall penetration loss.

4.2.2. Outdoor-to-Indoor Parameters

The outdoor-to-indoor large-scale parameters are the "B4 - Outdoor to indoor" channel model parameters defined in WINNER+ deliverable D5.3 [76]. This scenario provides the parameters to model outdoor BSs providing service to UEs of the "A1 - Indoor Office" scenario. The outdoor BSs are below rooftop micro BSs. The model distinguishes between LOS and NLOS conditions for the path from the BS to the outside wall of the building. We assume a LOS path from the BS to the outside wall of the building. For each UE the pathloss is calculated based on the path through the point on an outside wall nearest to the UE. The number of penetrated walls is determined as for the indoor BSs.

4.3. Base Station Deployments

We define six different BS deployments which are shown in Figure 4.2. Four deployments use indoor BSs only:

- ▷ *Single central BS* is a single BS with M antennas located in the corner of the room southwest of the center ("1" in Figure 4.2). This deployment is the classic massive MIMO deployment where all antennas are located at the same place.

- ▷ *Two indoor BSs* are two BSs with $M/2$ antennas each. One BS is located in the center of each corridor ("2").
- ▷ *Four indoor BSs* are four BSs with $M/4$ antennas each. Two BSs are located at the opposite ends of each corridor ("3").
- ▷ *Fourty indoor BSs* are forty BSs with $M/40$ antennas each. One BS is located in the center of each room ("4"). This deployment is similar to the deployment of p-cell [68].

One deployment uses outdoor BSs only:

- ▷ *Outdoor BSs* are two BSs with $M/2$ antennas each. One BS is located 15 m north of the middle of the north outside wall and one BS is located 15 m south of the middle of the south outside wall ("5"). Usually outdoor BSs are required to serve outdoor UEs. They might suffice to serve indoor UEs also.

One deployment uses indoor and outdoor BSs:

- ▷ *Indoor-outdoor BSs* are three BSs with $M/3$ antennas each. One BS is in the location of the *single central BS* deployment ("1") while two are in the location of the *outdoor BSs* deployment ("5"). If the BSs of the *outdoor BSs* deployment do not suffice, then they might be supported by an indoor BS.

Note that we need a sufficient backhaul (not shown in Figure 4.2) for the *two indoor BSs* deployment, the *four indoor BSs* deployment, the *fourty indoor BSs* deployment, the *outdoor BSs* and the *indoor-outdoor BSs* deployment to permit LS-MIMO and network MIMO. Also note that the BSs are not necessarily optimally placed.

The deployments serve outdoor and indoor UEs with different deployments as proposed in [77]. We do not simulate interference from other outdoor BSs since we assume that the inter-cell interference can be limited to few cells, for example, by the antenna down-tilt [69].

4.3.1. Antenna Array Configuration

The indoor BSs are rectangular arrays, while the outdoor BSs are uniform linear arrays (ULAs). The rectangular arrays are mounted underneath the ceiling at a height of 3 m. The antennas are spaced at half wavelength distance $\lambda_L/2$. We choose the side lengths of the rectangle such that $\left\lceil\sqrt{M_i}\right\rceil$ antennas fit per row and per column. Note that the last rows might not be fully occupied by antennas. We made this choice to compare the same number of antennas for different deployments. The area of the array is roughly

$$A = \frac{\lambda_L^2}{4}\left\lceil\sqrt{M_i}\right\rceil\left\lfloor\sqrt{M_i}\right\rfloor \geq \frac{\lambda_L^2}{4}M_i \tag{4.1}$$

which gives a realistic form factor [6]. The height of the outdoor BSs is 10 m and the antennas of the ULAs are located on a line parallel to the long side of the building. The antennas are again spaced equally at a $\lambda_L/2$ distance.

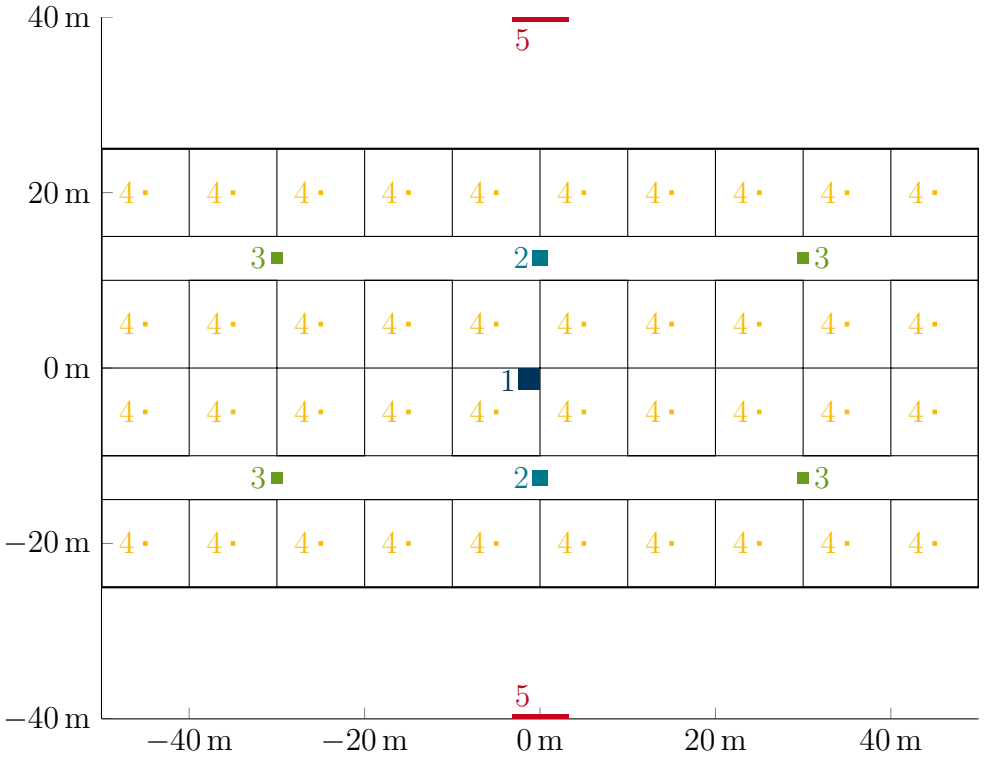

Figure 4.2.: Base station deployments in the indoor office scenario [74].

Since we place the BS antennas with an antenna spacing of $\lambda_L/2$, we assume that antenna array size increases with the number of antennas like in [49]. We assume that each antenna element is an isotopic radiator and that there is no mutual coupling between antennas. Unless otherwise stated, we assume ideal hardware, perfect synchronization, and perfect CSI of the complete network at all nodes.

5

Simulation Results

In this chapter, we compare the deployments and transmission schemes which we introduced in the previous chapters. Our results help guide design choices for future mobile communication systems, e.g., 5G. We presented preliminary results in [78–80] and we add the following results.

- ▷ Instead of using water-filling to allocate power, we refine the power allocation by using mercury/water-filling, which is optimal for finite modulation alphabets [19].
- ▷ We analyze the gap between mercury/water-filling, water-filling and equal power allocation.
- ▷ We analyze two additional deployments (the *two indoor BSs* deployment and the *fourty indoor BSs* deployment presented in Chapter 4).
- ▷ We add LS-MIMO as an example of an interference coordination scheme.
- ▷ We analyze the per-UE SEs.
- ▷ We analyze fairness for Gaussian modulation.
- ▷ We analyze the singular value spread to understand how well the UEs are separated.

5.1. Simulation Setup

We fix the number of UEs to $K = 24$ and compare the deployments with different performance measures for different numbers M of total BS antennas in the indoor office scenario

defined as "A1 - Indoor Office" in WINNER II [74]. We simulate 300 drops where one drop is a random placement of the UEs within the office building. For each drop we generate 10 channel realizations. The deployments and the generation of the channel coefficients are explained in detail in Chapter 4. The antenna array configuration with half wavelength spacing $\lambda_L/2$ is explained in Section 4.3.1. The wall penetration loss is 12 dB per wall.

We use a bandwidth of 20 MHz around a carrier frequency of 2.1 GHz. The active bandwidth is 18 MHz and 1 MHz on each side of this bandwidth is a guard band. The subcarrier spacing is 15 kHz and we obtain 1200 subcarriers. In LTE, subcarriers are arranged in groups of 12 consecutive subcarriers which are called physical resource blocks (PRBs). Hence we obtain 100 PRBs. The channel conditions of the subcarriers of one PRB are usually very similar. The schedule, power allocation and precoder are the same for all subcarriers of one PRB to save control signaling overhead. We save simulation time by simulating a single subcarrier per PRB and assuming that the same performance is achieved on the other subcarriers of the PRB.

Unless otherwise mentioned, we use 256 QAM, and we use mercury/water-filling to allocate power. The per-BS power in dBm at the i-th BS is constrained by

$$P_i = 26\,\mathrm{dBm} - 10\log_{10}\left(N_{\mathrm{BS}}\right). \tag{5.1}$$

The maximal per-BS powers are such that the maximal sum power available to the BSs is 26 dBm. We use a sum power constraint of $P_{\mathrm{total}} = 26\,\mathrm{dBm}$ to compare a sum power constraint and per-BS power constraints, and to determine the ZFBF precoders for network MIMO (see Section 3.4).

The thermal noise power is

$$P_{\mathrm{thermal}} = -173.8\,\mathrm{dBm} + 10\log_{10}\left(15\,\mathrm{kHz}\right) = -132.1\,\mathrm{dBm} \tag{5.2}$$

where 15 kHz is the subcarrier bandwidth and

$$-173.8\,\mathrm{dBm} = 10\log_{10}\left(k_B \cdot 1000\,\mathrm{mW/W} \cdot 300\,\mathrm{K}\right) \tag{5.3}$$

and the Boltzmann constant is

$$k_B = 1.3807 \times 10^{-23}\,\mathrm{J/K}. \tag{5.4}$$

The noise figure at the receiver is

$$P_{\mathrm{NF}} = 7\,\mathrm{dB}. \tag{5.5}$$

Hence the variance of the AWGN at the UEs, i.e., the noise level, is

$$\sigma_N^2 = P_{\mathrm{thermal}} + P_{\mathrm{NF}} = -125.1\,\mathrm{dBm}. \tag{5.6}$$

The simulation parameters are summarized in the Table 5.1. With these parameters,

Table 5.1.: Simulation Parameters

Carrier frequency	2.1 GHz
Bandwidth	20 MHz
Active bandwidth	18 MHz
Subcarrier spacing	15 kHz
Number of subcarriers	1200
Number of PRBs	100
Antenna Spacing	$\lambda_L/2$
Wall penetration loss	12 dB
Per-BS power constraint	$26\,\text{dBm} - 10\log_{10}(N_{\text{BS}})$
Noise level	-125.1 dBm
Largest modulation scheme	256 QAM
Number of UEs	24
Number of drops	300
Number of channel realizations per drop	10

the per-UE SE of the k-th UE without considering control signaling overhead is

$$S_k = \frac{12 \cdot \sum_{f=1}^{100} C\left(\text{SINR}_k^{(f)}\right) \cdot 14}{1\,\text{ms} \cdot 20\,\text{MHz}} \tag{5.7}$$

where 12 is the number of subcarriers per PRB, 100 is the number of PRBs, 14 is the number of OFDM blocks per subframe, 1 ms is the duration of one subframe[1] and $C\left(\text{SINR}_k^{(f)}\right)$ is the rate achieved at $\text{SINR}_k^{(f)}$ in bits (see Section 2.5). The sum SE in the building without considering control signaling overhead is

$$S = \sum_{k=1}^{24} S_k \tag{5.8}$$

where 24 is the number of UEs. The maximal sum SE for 256 QAM is

$$S^* = 161.28\,\text{bit/s/Hz} \tag{5.9}$$

since the rate $C\left(\text{SINR}_k^{(f)}\right)$ is bounded by 8 bits for 256 QAM.

[1] An LTE subframe contains 14 OFDM blocks and has a duration of 1 ms.

5.2. Sum Spectral Efficiency

We first analyze the average sum SE S achieved with 256 QAM and mercury/water-filling. We do not show the 5 %-tile sum SE and the 95 %-tile sum SE as they follow the same trends.

Figure 5.1 shows the average sum SEs of the deployments which use indoor BSs only for $M = 24$ to 240 total BS antennas. For the *single central BS* deployment there is only one BS, hence the curves for network MIMO, LS-MIMO, orthogonal reuse, and local precoding are equal.

Consider the sum SE achieved with network MIMO first (solid curves). The *single central BS* deployment, the *two indoor BSs* deployment, and the *four indoor BSs* deployment perform poorly for the fully loaded MIMO system with $M = 24$ BS antennas. All degrees-of-freedom are utilized to zero force interference leading to weak effective channels. The sum SE improves significantly when few antennas are added. We discuss in Section 5.4 how scheduling improves the sum SE for fully or close to fully loaded MIMO systems. Adding more antennas increases the sum SE, but the gain per additional antenna decreases. A ratio of twice as many BS antennas as UEs seems to be a good trade-off between achieved sum SE and number of BS antennas. For the *fourty indoor BSs* deployment the trend is similar, however, the fully loaded case is not included as the minimal number of antennas is $M = 40$. As expected, the distributed deployments (*two indoor BSs*, *four indoor BSs*, and *fourty indoor BSs*) outperform the *single central BS* deployment. The *four indoor BSs* deployment performs better than the *fourty indoor BSs* deployment for 40 antennas, which is an artifact of the suboptimal power allocation scheme. However, all distributed deployments perform similarly. The performance loss of the *single central BS* deployment (mainly due to wall penetration loss) is analyzed in more detail in Section 5.3. Note that the *four indoor BSs* deployment approaches the maximal SE $S^* = 161.28$ bit/s/Hz for only $M = 48$ BS antennas, while the *single central BS* deployment requires more than $M = 240$ antennas to approach S^*.

Next consider the sum SE achieved with LS-MIMO (dashed curves). Recall that for LS-MIMO at least $M = N_{\mathrm{BS}}K$ total BS antennas are required. Hence for the *two indoor BSs* deployment with $M = 48$ and for the *four indoor BSs* deployment with $M = 96$ all degrees-of-freedom are required to zero force interference and less BS antennas are not feasible. Similar to network MIMO, adding more antennas increases the sum SE, and the gain with each additional antenna decreases. Note that the *two indoor BSs* deployment achieves the same sum SE with LS-MIMO at $M = 84$ and with network MIMO at $M = 48$. One can trade off the costs of a backhaul with the number M of BS antennas to achieve the same sum SE. For other CS/CB schemes, fewer BS antennas might be able to achieve the same SE.

Local precoding is non-cooperative and performs poorly due to interference (dotted curves). For all deployments the sum SE improves little when adding antennas. Many more BS antennas are required as compared to network MIMO to achieve the same sum SE. Again, one can trade off the costs of a backhaul with the number BS antennas. The performance loss from network MIMO to local precoding is largest for the *four indoor BSs*

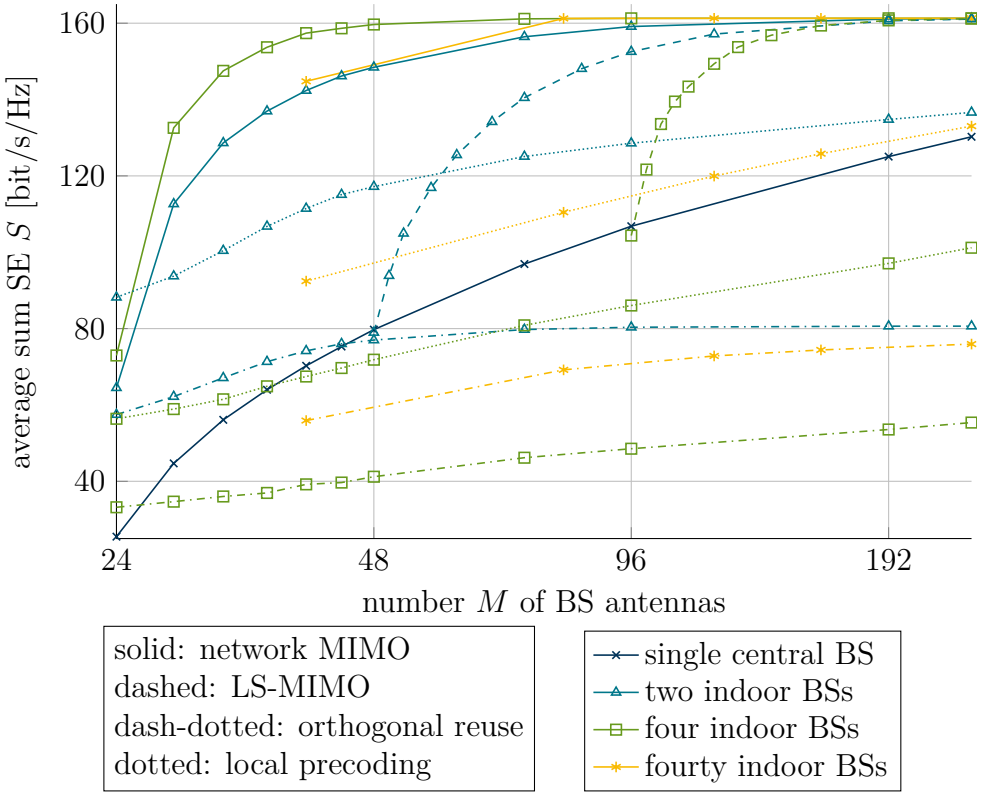

Figure 5.1.: Average sum SEs for 256 QAM and mercury/water-filling of the deployments which use indoor BSs only.

deployment. This is due to larger interference in the *four indoor BSs* deployment where not all BSs are separated by a wall. Compared to LS-MIMO more BS antennas are required to achieve the same sum SE, however, less CSI is required. Local precoding sometimes performs better than network MIMO. This can be explained as follows: For network MIMO all UEs are served. However, for local precoding, if more UEs are served by a BS than the BS can serve, only the best UEs are served. Recall that the best UEs are selected by the scheduling algorithm explained in Section 2.8. However, it may be beneficial to distribute BS antennas even without cooperation. For example, the *two indoor BSs* deployment with local precoding outperforms the *single central BS* deployment.

For orthogonal reuse we group the BSs into two groups (dash-dotted curves). For the *two indoor BSs* deployment we have one BS per group. For the *four indoor BSs* deployment the upper left BS and the lower right BS form the first group and the lower left BS and the upper right BS form the second group. For the *fourty indoor BSs* deployment we group the BSs such that neighboring BSs (also across the corridors) are in different groups. The performance with orthogonal reuse is very poor since only a fraction of the spectral resources is available at each BS, and since residual interference remains (except for the *two indoor BSs* deployment). Hence we do not consider spectral reuse further in this work.

Figure 5.2 shows additionally the average sum SEs of the deployments which use outdoor

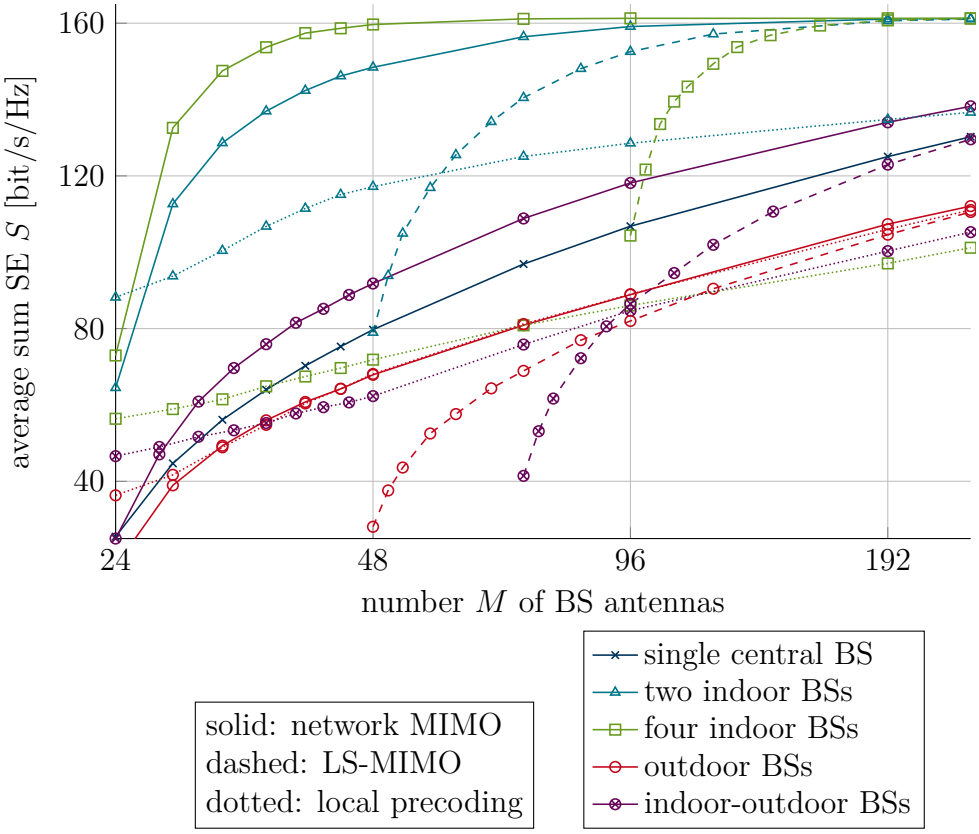

Figure 5.2.: Average sum SEs for 256 QAM and mercury/water-filling with outdoor-indoor deployments.

BSs. We do not show the *fourty indoor BSs* deployment to improve clarity.

First we analyze the *outdoor BSs* deployment which is realized without any indoor BSs. The performance with local precoding and with network MIMO are very close. There is little interference from the lower BS to the UEs in the upper half of the building and vice versa. However, this scheme performs poorly with all transmission schemes.

The *indoor-outdoor BSs* deployment combines the BSs of the *single central BS* deployment and the *outdoor BSs* deployment. The sum SE with network MIMO improves as compared to the *single central BS* deployment and the *outdoor BSs* deployment. However, the gap to the *two indoor BSs* deployment and the *four indoor BSs* deployment is still large. The performance of the *indoor-outdoor BSs* deployment with local precoding decreases as compared to the *outdoor BSs* deployment due to increased interference.

For both deployments one achieves the same sum SE with network MIMO and with LS-MIMO for a larger number of BS antennas. Again, scheduling a subset of UEs explains the sum SE gains of local precoding over network MIMO for few BS antennas.

In conclusion, the SE increases with the number of BS antennas for all deployments and all transmission schemes until it is limited by the maximal SE of the modulation. Cooperation between indoor BSs provides large gains, while cooperation between outdoor

BSs or indoor and outdoor BSs provides only smaller gains. Network MIMO performs best, but CS/CB is an interesting alternative as the backhaul requirements are reduced. Orthogonal reuse performs poorly and is worse than local precoding. As found in [63] a ratio of two to eight times as many BS antennas as served UEs is a good trade-off between performance and antenna costs, where the best trade-off depends on the transmission scheme and the BS deployment. The placement of BSs is important to overcome wall penetration losses and to control interference.

5.3. Average SNR Maps

In this section, we show why the deployments with only one or no indoor BS (*single central BS*, *outdoor BSs* and *indoor-outdoor BSs*) perform poorly as compared to the distributed indoor BSs deployments (*two indoor BSs*, *four indoor BSs*, and *fourty indoor BSs*).

We analyze the SNR achieved when a single UE is served at different positions within the office building. The BSs use network MIMO under per-BS power constraints. Each BS determines a MRT precoder coherently with the other BSs. We distribute the per-BS transmit power equally among the subcarriers. Hence the precoder at one subcarrier is

$$\boldsymbol{w} = \begin{bmatrix} \frac{\boldsymbol{h}_{1,1}}{\|\boldsymbol{h}_{1,1}\|_2}\sqrt{\frac{P_1}{N_{\mathrm{Sc}}}} \\ \vdots \\ \frac{\boldsymbol{h}_{N_{\mathrm{BS}},1}}{\|\boldsymbol{h}_{N_{\mathrm{BS}},1}\|_2}\sqrt{\frac{P_{N_{\mathrm{BS}}}}{N_{\mathrm{Sc}}}} \end{bmatrix} \in \mathbb{C}^M. \tag{5.10}$$

The SNR with MRT to the single UE serves as an upper bound to the SNR when more UEs are served with ZFBF or any other linear precoding scheme, as serving more UEs only reduces the degrees-of-freedom. When serving more UEs, the power used to convey information to one UE is scaled, for example, for $K = 24$ UEs the power is on average $10\log_{10}(K) = 13.8\,\mathrm{dB}$ lower.

Figure 5.3 shows the average SNRs achieved with MRT and 48 total BS antennas. For the *fourty indoor BSs* deployment the number of total BS antennas is only $M = 40$. We average over 300 channel realizations for each sampled position.

The *single central BS* deployment achieves low SNR in many rooms, especially those close to the outside wall. This is due to the wall penetration loss. Adding more antennas improves the SNR only slightly. Whereas the *two indoor BSs* deployment and the *four indoor BSs* deployment achieve higher SNR in the rooms close to the outside wall because the wall penetration loss is less. The *fourty indoor BSs* deployment achieves with slightly less BS antennas an even more uniform coverage than the *two indoor BSs* deployment and the *four indoor BSs* deployment. The *outdoor BSs* deployment achieves acceptable SNR in the rooms next to the outside walls. However, the SNR in the inner rooms and the corridors is poor. The *indoor-outdoor BSs* deployment achieves higher SNR than the *outdoor BSs* deployment or the *single central BS* deployment alone, but the SNR is still lower than with the distributed indoor BSs deployments.

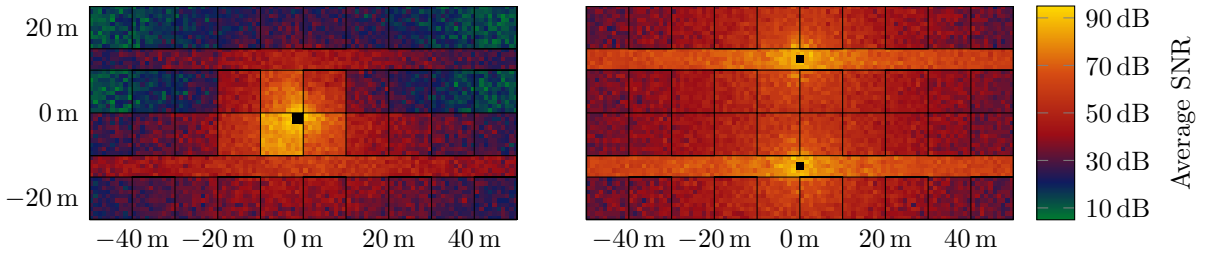

(a) *Single central BS* deployment with 48 transmit antennas.

(b) *Two indoor BSs* deployment with 48 transmit antennas.

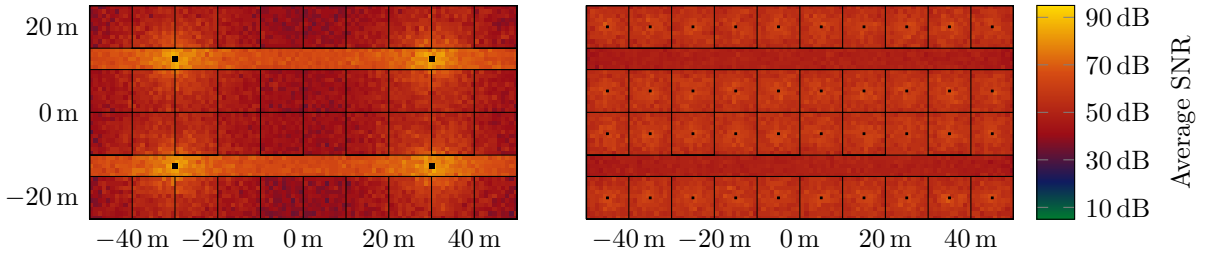

(c) *Four indoor BSs* deployment with 48 transmit antennas.

(d) *Fourty indoor BSs* deployment with 40 transmit antennas.

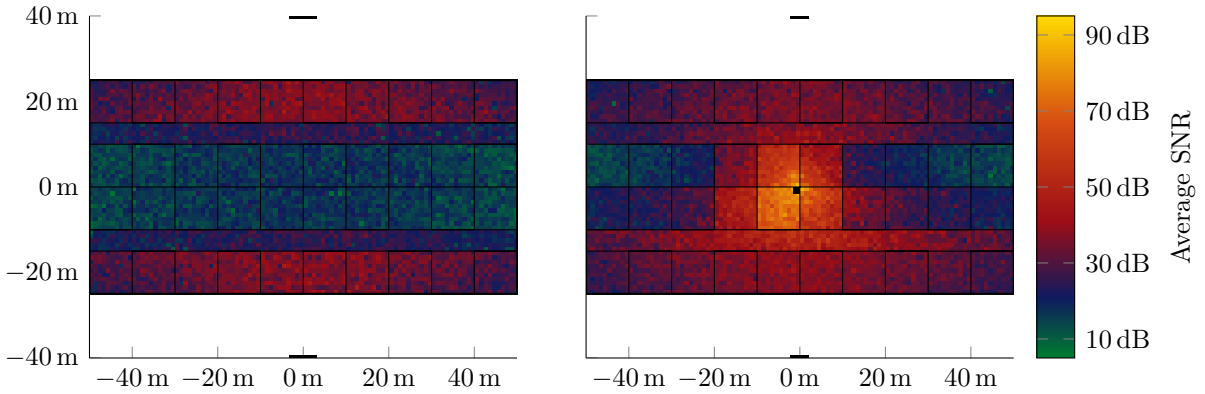

(e) *Outdoor BSs* deployment with 48 transmit antennas.

(f) *Indoor-outdoor BSs* deployment with 48 transmit antennas.

Figure 5.3.: Average SNR achieved with MRT at a single UE for different positions.

We conclude that the lower SEs of the *single central BS* deployment, the *outdoor BSs* deployment, and the *indoor-outdoor BSs* deployment are at least partly due to the large wall penetration loss and the building penetration loss.

5.4. Scheduling Gains

As we discussed in Section 2.9 one claim of massive MIMO is that with sufficient degrees-of-freedom the transmit signals are directed precisely to the UEs through precoding [15]. It is then optimal to schedule all UEs on each subcarrier and advanced scheduling/UE-selection strategies do not provide gains [6]. We compare scheduling all UEs on all subcarriers to the example Scheduling Algorithm 5.1 to analyze how many BS antennas are required for this claim to be valid in our scenario.

The example Scheduling Algorithm 5.1 utilizes the following idea: When we use mercury/water-filling as described in Section 2.6 there is usually no power allocated to some UEs on some subcarriers. When no power is allocated to a subcarrier the interference zero-forcing constraint for that UE is unnecessary on that subcarrier. Removing this constraint leaves more degrees-of-freedom when determining the precoders for the other UEs, which leads to potentially higher effective channel gains. Algorithm 5.1 starts by initializing the schedules $\mathcal{T}^{(f)}$ on all subcarriers as all UEs scheduled. Then we determine for each subcarrier the ZFBF precoder for the UEs scheduled on the subcarrier. Next we collect the effective channels obtained by ZFBF in $\overline{\boldsymbol{h}}$, where the effective channels of unscheduled UEs are zero. We determine the power allocation $\overline{\boldsymbol{p}}$ with mercury/water-filling. We then determine for each subcarrier the new schedule $\mathcal{T}^{(f)}$. The new schedule $\mathcal{T}^{(f)}$ consists of the UEs to which a positive power is allocated to. The next iteration starts with determining the ZFBF precoder for the UEs scheduled on the subcarrier. The algorithm stops once all schedules have converged. Note that fairness is not an objective of Scheduling Algorithm 5.1.

Figure 5.4 shows the average sum SEs of network MIMO achieved with 256 QAM and mercury/water-filling for all UEs being scheduled on all subcarriers, and for the example Scheduling Algorithm 5.1. As expected, the scheduling algorithm provides a considerable gain for less than twice as many BS antennas as UEs. For the *single central BS* deployment, the *two indoor BSs* deployment, and the *four indoor BSs* deployment the gain is small for $M = 48$ and very little for $M = 96$. However, for the *outdoor BSs* deployment a small gain and for the *indoor-outdoor BSs* deployment a larger gain appears for all considered numbers of BS antennas. This is somewhat surprising as we would expect scheduling all UEs on all subcarriers to be optimal for a larger number of BS antennas for all deployments.

We conclude that for indoor-to-indoor channels and more than two- to four-times as many BS antennas as served UEs it is optimal to schedule all UEs on all subcarriers. However, our scheduling algorithm is not optimal and other scheduling algorithms might achieve gains for more BS antennas, e.g., [81]. However, for outdoor-to-indoor channels scheduling does provide gains also for ten-times as many BS antennas as served UEs.

5.5. Comparison to Capacity Upper Bound

Massive MIMO lets simple transmission schemes approach capacity with an increasing number of BS antennas. In the following, we analyze this statement for our network

Algorithm 5.1 Example scheduling algorithm

for $f = 1$ **to** N_{Sc} **do** (all subcarriers)
  $\mathcal{T}^{(f)} = \{1, 2, \ldots, K\}$ (initialize as all UEs scheduled)
end for
repeat
  for $f = 1$ **to** N_{Sc} **do** (all subcarriers)
    $\tilde{\boldsymbol{h}}^{(f)} = \mathbf{0}$ (set effective channels to zero)
    Apply ZFBF on $\begin{bmatrix} \left(\boldsymbol{h}^{(f)}_{\mathcal{T}^{(f)}(1)}\right)^{\mathsf{H}} \\ \vdots \\ \left(\boldsymbol{h}^{(f)}_{\mathcal{T}^{(f)}\left(\left|\mathcal{T}^{(f)}\right|\right)}\right)^{\mathsf{H}} \end{bmatrix}$ (channels of scheduled UEs)
    and determine effective channels $\left[\tilde{h}^{(f)}_{\mathcal{T}^{(f)}(1)}, \ldots, \tilde{h}^{(f)}_{\mathcal{T}^{(f)}\left(\left|\mathcal{T}^{(f)}\right|\right)}\right]$ (see (2.31))
  end for
  $\overline{\boldsymbol{h}} = \left[\left(\tilde{\boldsymbol{h}}^{(1)}\right)^{\mathsf{T}}, \ldots, \left(\tilde{\boldsymbol{h}}^{(N_{\mathrm{Sc}})}\right)^{\mathsf{T}}\right]^{\mathsf{T}}$ (collect effective channel coefficients)
  allocate power $\overline{\boldsymbol{p}} = \left[\left(\tilde{\boldsymbol{p}}^{(1)}\right)^{\mathsf{T}}, \ldots, \left(\tilde{\boldsymbol{p}}^{(N_{\mathrm{Sc}})}\right)^{\mathsf{T}}\right]^{\mathsf{T}}$ by mercury/water-filling
  for $f = 1$ **to** N_{Sc} **do** (all subcarriers)
    $\mathcal{T}^{(f)} = \left\{k \in \mathcal{T}^{(f)} \middle| \left[\tilde{\boldsymbol{p}}^{(f)}\right]_{(k)} > 0\right\}$ (schedule UEs with positive power allocated)
  end for
until convergence of all schedules $\mathcal{T}^{(f)}$

MIMO transmission scheme.

We upper bound the capacity of a deployment by the capacity of a BC under a total power constraint. We allow all BSs of a deployment to cooperate and to act as one BS with distributed antennas, and relax the per-BS power constraint to a total-power constraint. Note that for the *single central BS* deployment the upper bound is tight. The capacity of a BC is achieved by dirty-paper coding [29–32]. We find the optimal DPC transmission policy as described in Section 2.7. We compare capacity to the SEs achieved with Gaussian modulation, since 256 QAM limits SE, while Gaussian modulation allows to approach the capacity upper bound.

Figure 5.5 shows the average sum SEs achieved with Gaussian modulation and network MIMO under per-BS power constraints and under a total power constraint, and the capacity upper bounds. The general trends are similar as in Figure 5.1 and Figure 5.2 for 256 QAM, but the SEs increase without bound with the number of BS antennas. For few BS antennas, the gap between the capacity upper bound and network MIMO is large, but the gap could be reduced by more advanced scheduling. With an increasing number of BS antennas, the gap decreases and the network MIMO scheme under a total power constraint approaches capacity. For $M = 48$ BS antennas the gap between the capacity upper bound and our schemes is already small. Twice as many BS antennas as served UEs

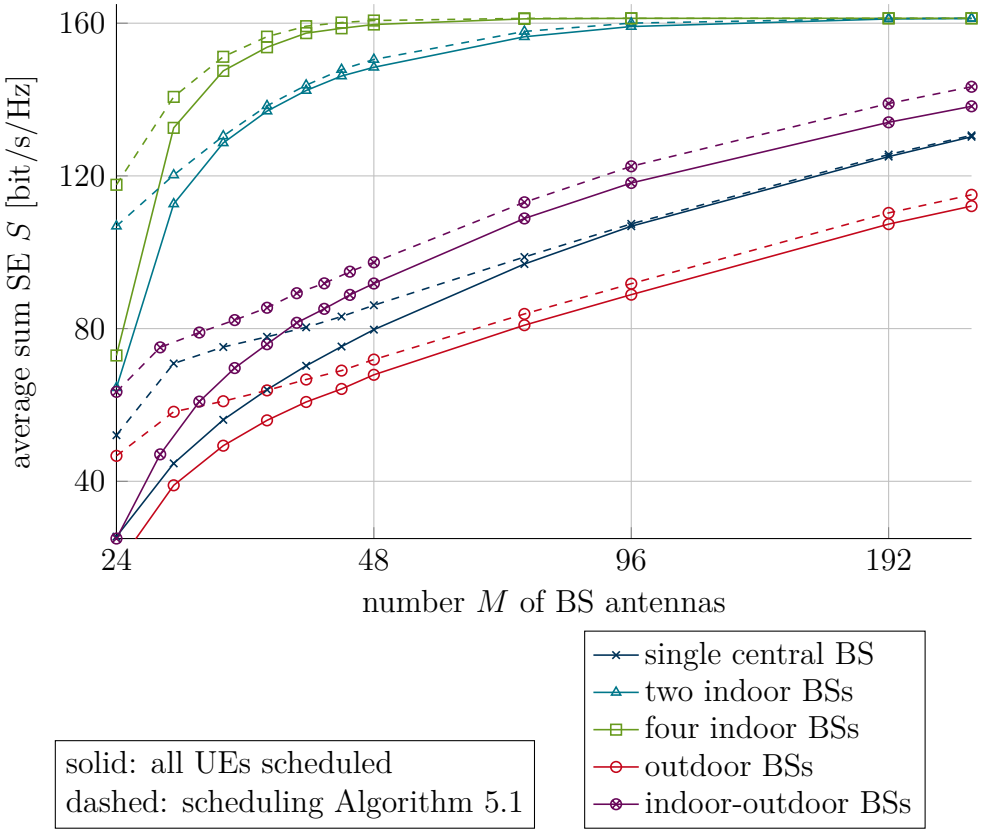

Figure 5.4.: Average sum SEs of network MIMO for 256 QAM and mercury/water-filling.

seems to be a good trade-off between performance and the number of BS antennas. While the gap vanishes completely under a total power constraint, a gap remains under per-BS power constraints. Determining more accurate capacity upper bounds given per-BS power constraints, and choosing better precoding and power allocation under per-BS power constraints would reduce the gap. We analyze the gap between a total power constraint and per-BS power constraints for 256 QAM in the next section. In summary, massive MIMO allows simple transmission schemes to approach capacity with an increasing number of BS antennas in our scenarios.

5.6. Comparison of Power Allocations

So far we used mercury/water-filling under per-BS power constraints to allocate power across subcarriers. Here we compare mercury/water-filling under per-BS power constraints to an equal power allocation under per-BS power constraints, to water-filling under per-BS power constraints, and to mercury/water-filling under a total power constraint.

For the equal power allocation we distribute the total transmit power P_{total} equally to

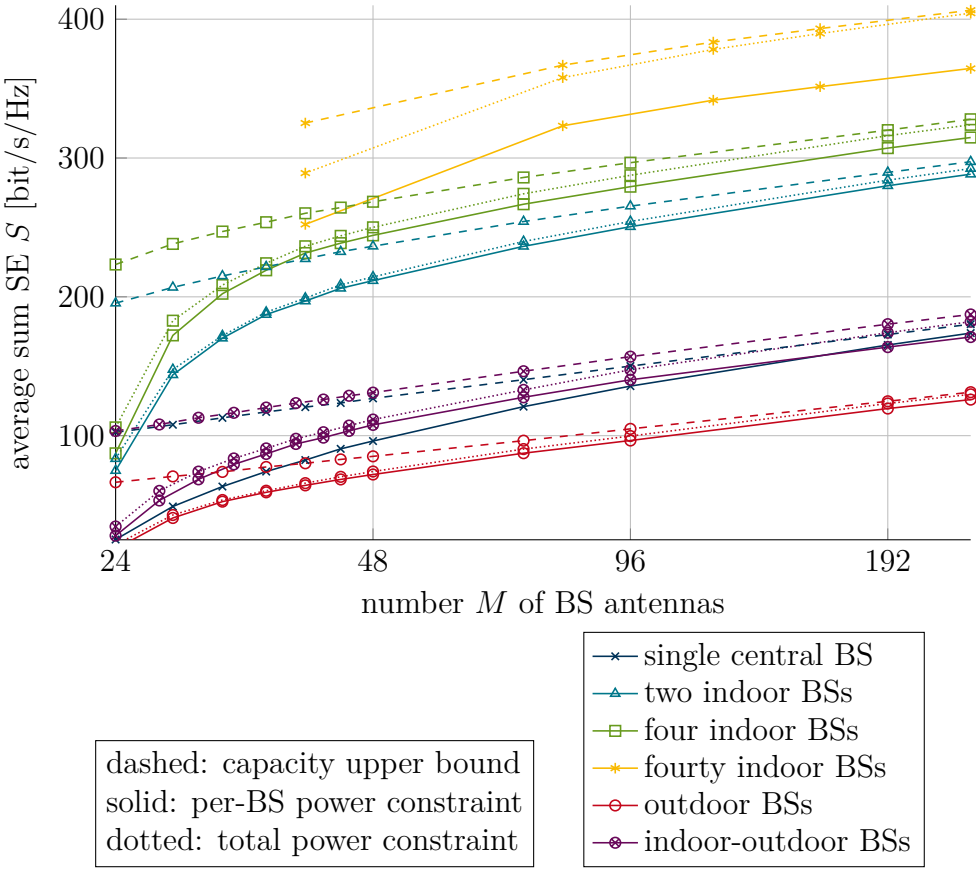

Figure 5.5.: Average sum SEs of network MIMO for Gaussian modulation.

the subcarriers of all UEs

$$\overline{\boldsymbol{p}}^{\mathrm{eq}} = \frac{P_{\mathrm{total}}}{KN_{\mathrm{Sc}}}\mathbf{1} \in \mathbb{R}^{KN_{\mathrm{Sc}}}. \tag{5.11}$$

Then we scale the power allocation to fulfill the per-BS power constraint like for network MIMO with mercury/water-filling in Section 3.4. If the channels harden, then the equal power allocation should approach the performance of mercury/water-filling.

For water-filling under per-BS power constraints we proceed like for mercury/water-filling in Section 3.4: we do water-filling assuming a total power constraint and then scale the power allocation to fulfill the per-BS power constraints. The SEs of more optimal power allocations under per-BS power constraints are bounded by the SEs of mercury/water-filling under a total power constraint.

Figure 5.6 shows the relative network MIMO sum SE gap of different power allocations compared to mercury/water-filling under per-BS power constraints. The relative sum SE gap is

$$\frac{S' - S_{\mathrm{merWf}}}{S_{\mathrm{merWf}}} \tag{5.12}$$

where S' is the SE achieved by the considered power allocation and S_{merWf} is the SE achieved by mercury/water-filling.

Consider the relative SE gap between the equal power allocation and mercury/water-filling under per-BS power constraints (solid curves). Mercury/water-filling outperforms the equal power allocation for all deployments except the *fourty indoor BSs* deployment. Especially the *single central BS* deployment, the *outdoor BSs* deployment, and the *indoor-outdoor BSs* deployment show a large gap for few BS antennas. For the *fourty indoor BSs* deployment the equal power allocation achieves higher average SE. This is due to the suboptimal scaling of mercury/water-filling to fulfill the per-BS power constraints. Note that for the *single central BS* deployment, the *outdoor BSs* deployment, and the *indoor-outdoor BSs* deployment a gap between 2.0 % to 4.1 % remains for many BS antennas.

Next compare mercury/water-filling and water-filling (dotted curves). Recall that water-filling assumes Gaussian modulation although 256 QAM is used. The average SE achieved with water-filling is only up to 4.3 % worse than with mercury/water-filling. For the *fourty indoor BSs* deployment water-filling achieves higher average SE which we can explain again by the suboptimal scaling to fulfill the per-BS power constraints while mercury/water-filling.

The relative gap between mercury/water-filling under a total power constraint and mercury/water-filling under per-BS power constraints is large for few antennas (dashed curves). For most deployments it decreases with an increasing number of BS antennas. This means that the suboptimal scaling to fulfill the per-BS power constraints approaches optimality. However, for the deployments with outdoor BSs (*outdoor BSs* and *indoor-outdoor BSs*) a gap between 2.7 % to 3.7 % remains.

We conclude that the performance differences between power allocations become small or disappear for more than twice as many BS antennas as the number of served UEs.

5.7. Per-UE Spectral Efficiency

We next analyze the per-UE SEs to understand the differences between the deployments in more detail. For 256 QAM the maximal per-UE SE is $S_k^* = 6.72\,\text{bit/s/Hz}$.

Figure 5.7 shows the cumulative distribution function (CDF) of the per-UE SEs achieved with network MIMO, 256 QAM, and mercury/water-filling. For the fully loaded case of $M = 24$ BS antennas we observe a poor performance for most UEs. For all deployments a fraction of the UEs achieves zero rate as no power is allocated to them on any subcarrier. For example, for the *single central BS* deployment more than half of the UEs are not served. This behavior is due to the sum rate maximization objective of mercury/water-filling. We analyze the fairness between UEs in Section 5.8 in more detail. Changing the power allocation can improve fairness at the cost of sum rate.

With an increasing number of BS antennas the CDF curves move to the right. The deployments with cooperating indoor BSs (*two indoor BSs*, *four indoor BSs* and *fourty indoor BSs*) achieve high median per-UE SEs and high 5 %-tile per-UE SEs with $M = 40$ BS antennas. The deployments with only one or no indoor BS (*single central BS*, *outdoor*

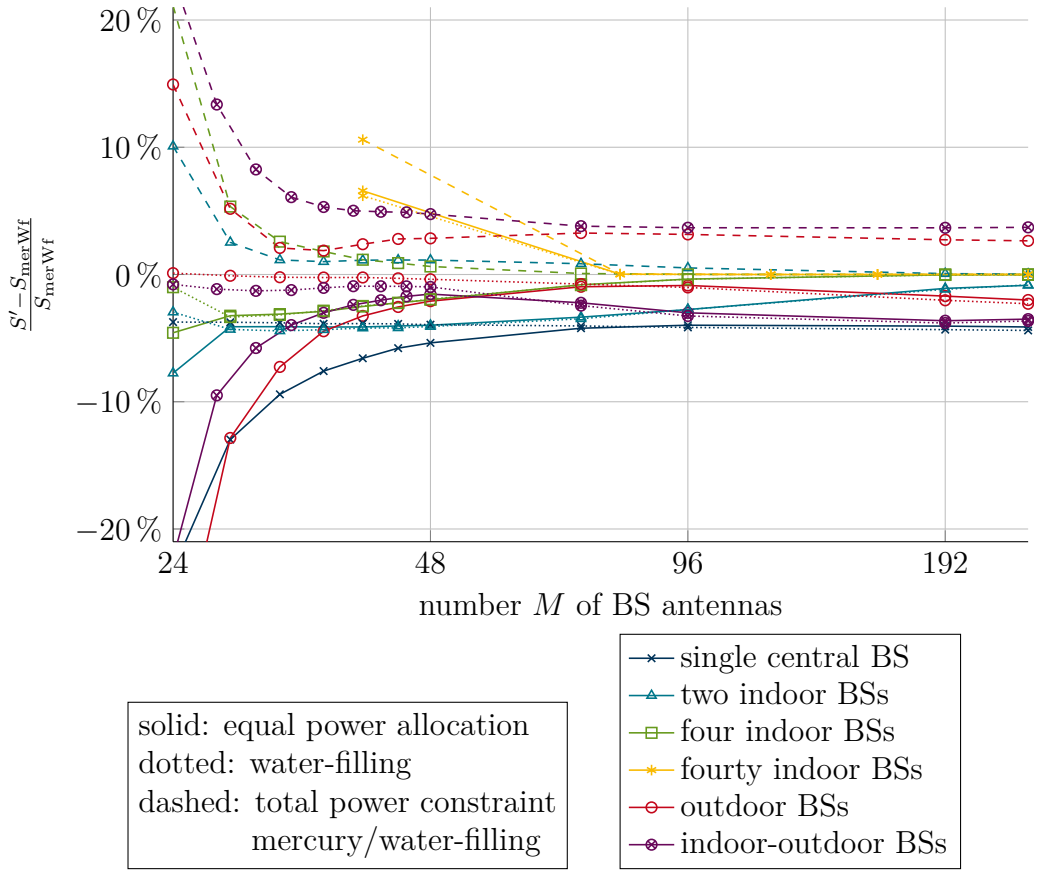

Figure 5.6.: Network MIMO relative gap to mercury/water-filling under per-BS power constraints.

BSs and *indoor-outdoor BSs*) achieve acceptable median per-UE SEs, but poor 5 %-tile per-UE SEs with $M = 40$ BS antennas.

With $M = 240$ BS antennas the deployments with cooperating indoor BSs achieve the maximal SE for almost all UEs. The deployments with only one or no indoor BS achieve high median per-UE SEs, while the 5 %-tile per-UE SEs are still lower. For LS-MIMO the trends are similar (keeping in mind that the fully loaded cases appear at different numbers of BS antennas).

We conclude that deploying more than one indoor BS achieves high sum SEs and at the same time high per-UE SEs for most UEs with fewer antennas as compared to deploying only one or no indoor BS.

5.8. Fairness Analysis

In the previous section we saw that the UEs achieve different per-UE SE. In this section, we analyze the fairness of our deployments and transmission schemes. Our transmission

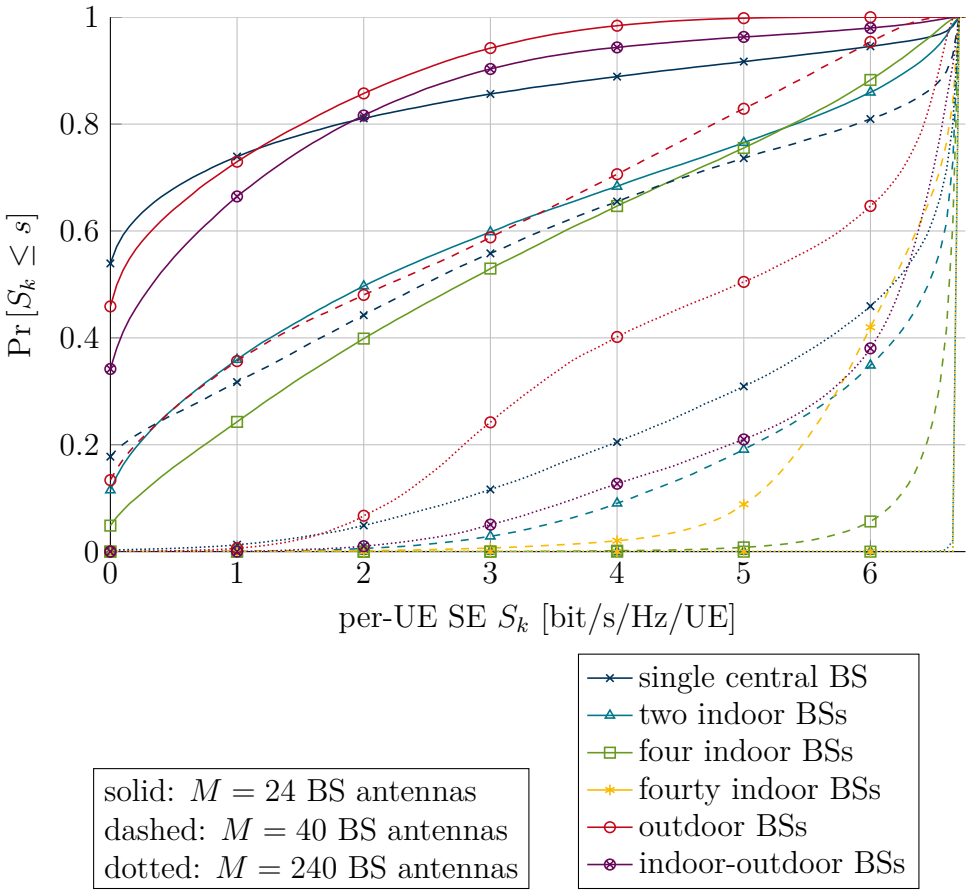

Figure 5.7.: CDF of the per-UE SEs achieved with network MIMO for 256 QAM and mercury/water-filling.

schemes should approach fairness with an increasing number of BS antennas as the channels harden (see Section 2.9).

We measure fairness quantitatively with Jain's index [82]

$$J\left(S_1, S_2, \ldots, S_K\right) = \frac{\left(\sum_{k=1}^{K} S_k\right)^2}{K \cdot \sum_{k=1}^{K} {S_k}^2} \tag{5.13}$$

where S_k is the per-UE SE of the k-th UE. Jain's index is 1 when all UEs achieve the same per-UE SE and is $1/K$ when only one UE achieves a positive per-UE SE. The advantage of Jain's fairness index is that it is dimensionless and scale invariant, and it changes continuously with SE changes [82].

Figure 5.8 shows the simulated fairness indices for 256 QAM and mercury/water-filling. For network MIMO and LS-MIMO the *two indoor BSs* deployment, the *four indoor BSs* deployment, and the *fourty indoor BSs* deployment approach fairness indices of 1 with an increasing number of BS antennas. They achieve close to perfect fairness for

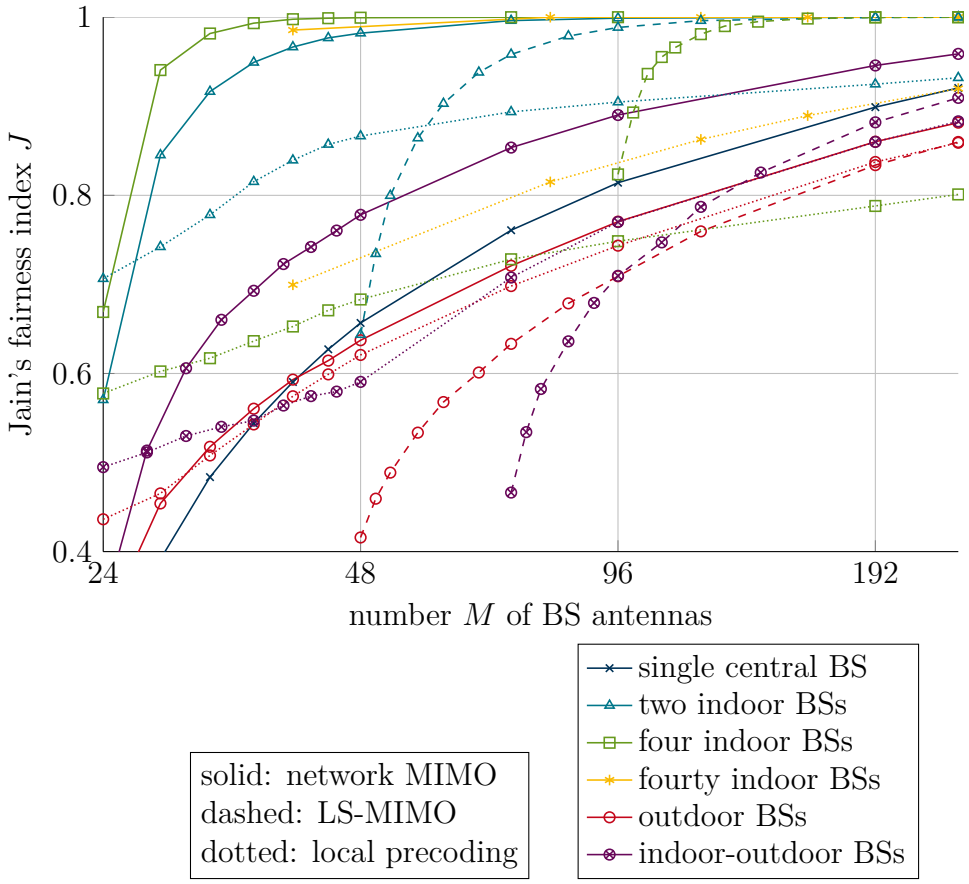

Figure 5.8.: Jain's fairness index for 256 QAM and mercury/water-filling.

network MIMO and $M = 96$ or for LS-MIMO and $M = 192$. This is partly due to all UEs being served with the maximal per-UE SE S_k^* of 256 QAM. For local precoding, the fairness indices are lower and they do not approach a fairness index of 1 in the range of BS antennas we consider. The *single central BS* deployment, the *outdoor BSs* deployment, and the *indoor-outdoor BSs* deployment do not approach a fairness index of 1 with any transmission scheme in the range of BS antennas, but the index increases with the number M of BS antennas.

We analyze the fairness achieved by Gaussian modulation and water-filling in Figure 5.9 to learn how much the saturation at the maximal sum-SE S^* of 256 QAM influences fairness. For Gaussian modulation the SE is not limited. The trends of Jain's fairness index are similar, but no deployment achieves perfect fairness. The perfect fairness achieved for 256 QAM is hence due to the saturation of the SE. If network MIMO is used, fairness increases when the BS antennas are more distributed.

Figure 5.10 shows Jain's fairness index achieved for network MIMO, 256 QAM and different power allocations and schedules. The Scheduling Algorithm 5.1 helps to increase fairness for few BS antennas. The equal power allocation achieves mostly lower fairness

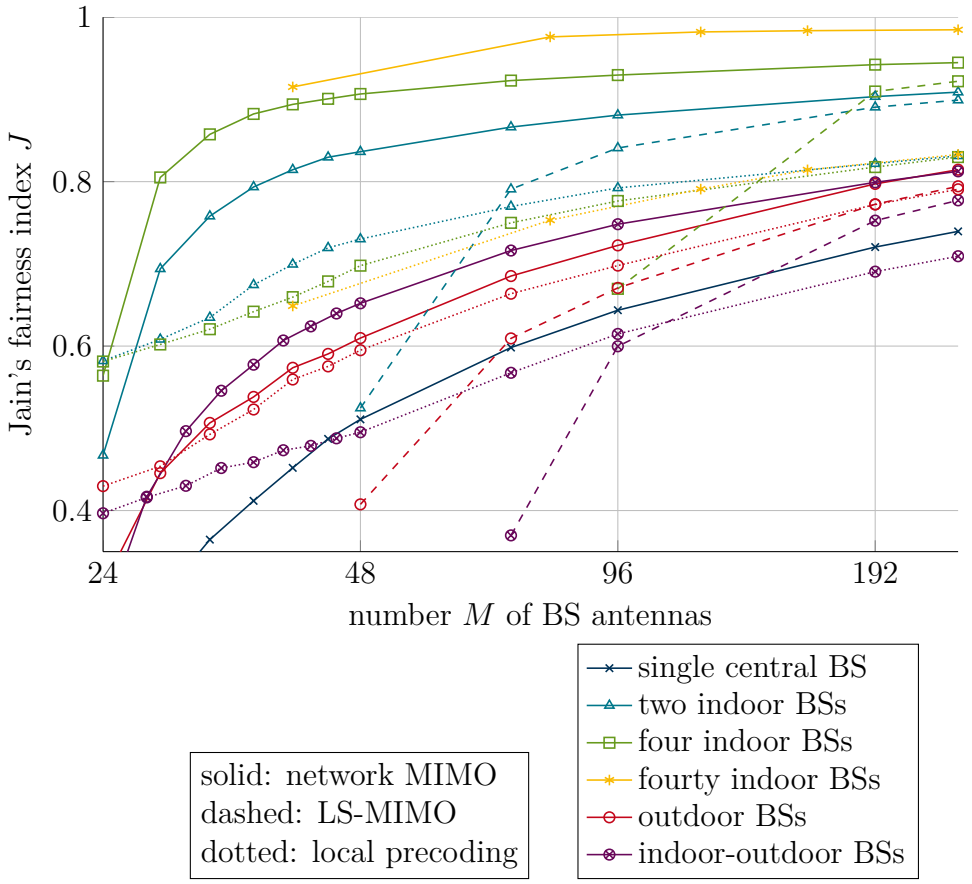

Figure 5.9.: Jain's fairness index for Gaussian modulation and water-filling.

indices as compared to mercury/water-filling. Although the same power is allocated to each UE, the difference in channel attenuation seems to lead to divers SEs. Only for the deployments with outdoor BSs (*outdoor BSs* and *indoor-outdoor BSs*) the equal power allocation sometimes achieves higher fairness.

We conclude that fairness increases with the number of BS antennas, with the level of cooperation between BSs, and with the distribution of BS antennas (given some cooperation between BSs). Note that one can increase fairness by making it an objective while scheduling and allocating power.

5.9. Singular Value Spread

Multiple UEs can be served simultaneously by using (massive) MIMO if the channel vectors to the UEs are sufficiently different [5]. In the best case the channel vectors are jointly orthogonal. This is also called "favorable" propagation or a very well conditioned channel matrix. While the joint orthogonality of i.i.d. Rayleigh-fading channels increases with the number of BS antennas [15] this must be verified for realistic channels [51].

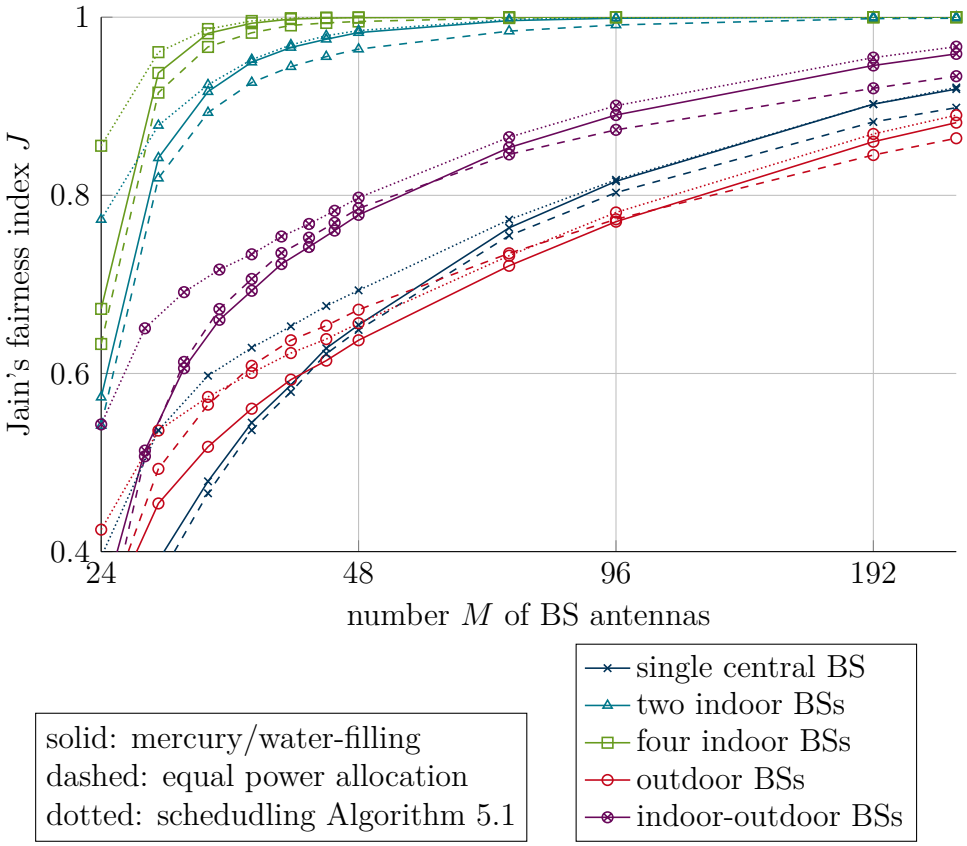

Figure 5.10.: Jain's fairness index of network MIMO for 256 QAM.

We follow [51] to quantify the joint orthogonality by analyzing the singular value spread of the normalized channel matrix. We normalize the channel matrix to remove the channel attenuation and to keep the variations over the BS antennas and the frequencies only. The normalized channel matrix at the f-th subcarrier is

$$\left(\boldsymbol{H}_{\text{norm}}^{(f)}\right)^{\mathsf{H}} = \begin{bmatrix} \left(\boldsymbol{h}_{1,\text{norm}}^{(f)}\right)^{\mathsf{H}} \\ \vdots \\ \left(\boldsymbol{h}_{K,\text{norm}}^{(f)}\right)^{\mathsf{H}} \end{bmatrix} \in \mathbb{C}^{K \times M} \tag{5.14}$$

where the k-th row is a scaled version of the channel vector $\left(\boldsymbol{h}_k^{(f)}\right)^{\mathsf{H}}$ of the k-th UE at the f-th subcarrier

$$\boldsymbol{h}_{k,\text{norm}}^{(f)} = \sqrt{\frac{MN_{\text{Sc}}}{\sum_{f=1}^{N_{\text{Sc}}} \left\|\boldsymbol{h}_k^{(f)}\right\|_2^2}} \boldsymbol{h}_k^{(f)} \in \mathbb{C}^M. \tag{5.15}$$

The singular value decomposition (SVD) of the normalized channel matrix is

$$\left(\boldsymbol{H}_{\text{norm}}^{(f)}\right)^{\mathsf{H}} = \boldsymbol{U}^{(f)}\boldsymbol{\Upsilon}^{(f)}\left(\boldsymbol{V}^{(f)}\right)^{\mathsf{H}} \tag{5.16}$$

where $\boldsymbol{U}^{(f)} \in \mathbb{C}^{K\times K}$ and $\boldsymbol{V}^{(f)} \in \mathbb{C}^{M\times M}$ are unitary and the diagonal matrix $\boldsymbol{\Upsilon}^{(f)} \in \mathbb{C}^{K\times M}$ contains the singular values $\upsilon_1^{(f)}, \ldots, \upsilon_K^{(f)}$. Recall that $M \geq K$. The singular value spread is the ratio between the largest and the smallest singular value[2]

$$\kappa^{(f)} = \frac{\max\limits_k \upsilon_k^{(f)}}{\min\limits_k \upsilon_k^{(f)}}. \tag{5.17}$$

A large singular value means that at least two channel vectors are similar, i.e., they are close to parallel. For $\kappa^{(f)} = 1$ all channel vectors are orthogonal to each other. The rank of the matrix $\left(\boldsymbol{H}_{\text{norm}}^{(f)}\right)^{\mathsf{H}}$ is equal to the number of singular values larger than zero [83]. A rank deficiency ($\text{rank}\left(\boldsymbol{H}_{\text{norm}}^{(f)}\right) < K$) hence implies an infinite singular value spread. When serving multiple UEs, the more their channel vectors are jointly orthogonal the better the performance.

In [51] the singular value spread is determined for ULA measurements and cylindrical array measurements in outdoor environments. The results are compared to i.i.d. Rayleigh fading channels. The authors find that for a fixed number of UEs the singular value spread and its variance decrease with the number of BS antennas both for i.i.d. Rayleigh fading channels and for the measured channels. The ULA achieves similar spreads as the i.i.d. channel coefficients while the cylindrical array has larger spreads. In [15] an indoor BS serves three indoor UEs and three outdoor UEs. Again for a large number of BS antennas a low singular value spread with low variance is observed.

Figure 5.11 shows the CDF of the normalized singular value spread achieved with network MIMO. We also include i.i.d. Rayleigh fading as a benchmark. With an increasing number of BS antennas the singular value spread decreases. Adding few BS antennas to the fully loaded case $M = 24$ lowers the normalized singular value spread significantly. For many antennas ($M = 240$) the UEs experience very similar effective channels. The *single central BS* deployment, the *two indoor BSs* deployment, the *four indoor BSs* deployment, and the *indoor-outdoor BSs* deployment achieve similar spreads. The *outdoor BSs* deployment has lower spreads, close to Rayleigh fading. The *fourty indoor BSs* deployment with $M = 40$ BS antennas has significantly higher spreads. For $M = 40$ two or more UEs in the same room with a BS are poorly separable since there is only a single antenna at each BS.

In conclusion, the singular value spread follows similar trends as for the channel measurements [15, 51]. It decreases as the number of BS antennas increases and is similar to the singular value spread of i.i.d. Rayleigh fading.

[2]The singular value spread is equal to the condition number with respect to the l_2-norm.

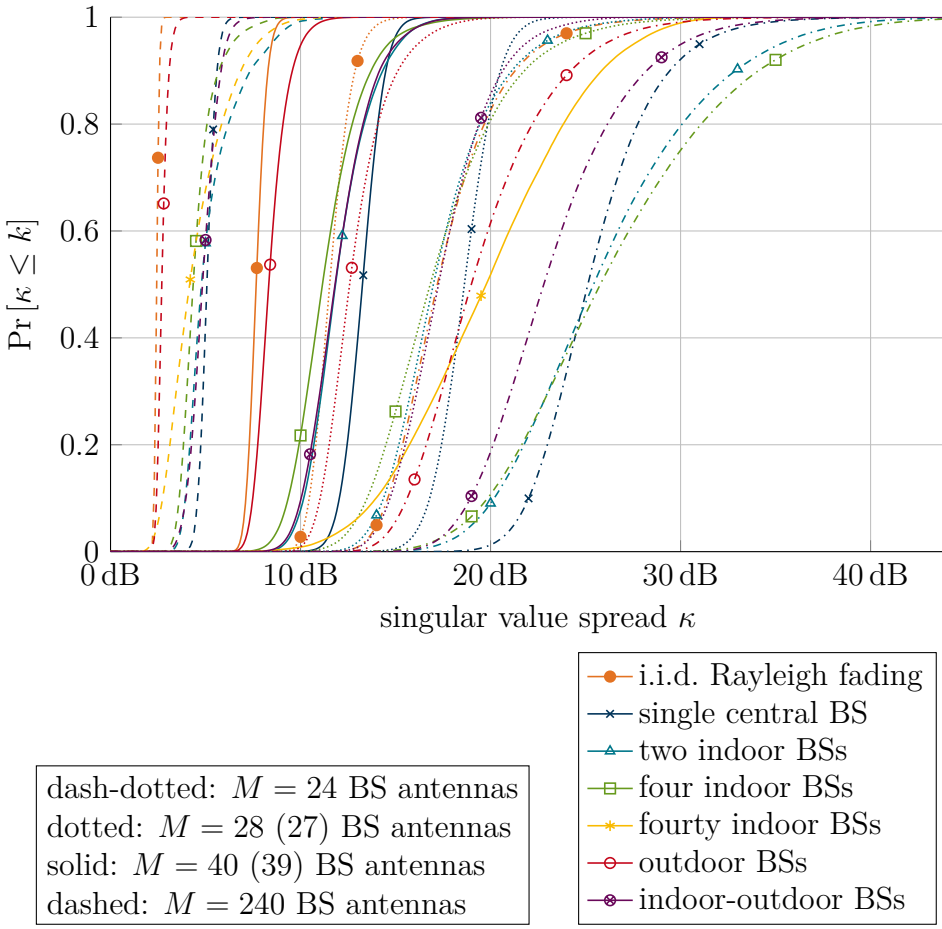

Figure 5.11.: CDF of the normalized singular value spread achieved with network MIMO and $M = \{24, 28, 40, 240\}$ BS antennas ($M = \{24, 27, 39, 240\}$ for the *indoor-outdoor BSs* deployment).

5.10. Noisy Channel Estimation

So far we analyzed performance with perfect CSI. However, perfect CSI is usually not available. In practical systems the channel coefficients are estimated with the help of pilots, but also other methods are exist, for example, ray-tracing or channel prediction [78,84]. We discuss the use of pilots to estimate channel coefficients in the context of massive MIMO in Section 2.9. More details on channel estimation can be found in [84], for example. Channel estimation schemes result in estimation errors, delays and overhead which affect performance.

In this section, we analyze the effect of estimation errors on the average SE. We denote the channel coefficient with estimation error from the m-th antenna of the i-th BS to the k-th UE at the subcarrier f as

$$\hat{h}_{i,k,m}^{(f)} = h_{i,k,m}^{(f)} + e_{i,k,m}^{(f)} \in \mathbb{C} \tag{5.18}$$

where $e_{i,k,m}^{(f)} \in \mathbb{C}$ is the estimation error. We model the estimation error as zero-mean proper complex Gaussian random variables, which are independent from each other and from the channel coefficients. We also assume that the estimation error of the channel between the i-th BS and the k-th UE is normalized such that its variance scales with the average channel coefficient power of the UE across the BS antennas and the subcarriers

$$\mathbb{E}\left[\left|e_{i,k,m}^{(f)}\right|^2\right] = \frac{1}{MN_{\mathrm{Sc}}} \sum_{m=1}^{M} \sum_{f=1}^{N_{\mathrm{Sc}}} \left|h_{i,k,m}^{(f)}\right|^2 \sigma_E^2 \tag{5.19}$$

where σ_E^2 is the normalized estimation error variance.

We determine the precoding based on the channel estimation with error. For this precoding, intra-cell interference occurs due to the estimation error. Figure 5.12 shows the average SEs versus normalized estimation error variance achieved with network MIMO and 48 total transmit antennas, except for the *fourty indoor BSs* deployment where we deploy only 40 total BS antennas. The performance of all deployments degrades with increasing estimation error variance. In Section 5.6 we saw that, with perfect CSI, mercury/water-filling performs better than equal power allocation for all deployments except for the *fourty indoor BSs* deployment. This is also the case for very low normalized estimation error variance. However, for higher normalized estimation error variance mercury/water-filling performs worse because mercury/water-filling is not aware of the intra-cell interference introduced by the estimation error. To make mercury/water-filling more robust one could gather the intra-cell interference statistics and adapt the power allocation based on these statistics. The equal power allocation is more robust per se and is optimal in case of no CSI [28]. The *two indoor BSs* deployment and the *four indoor BSs* deployment suffer most from the channel estimation error. For mercury/water-filling and high normalized estimation error variance the *two indoor BSs* deployment and the *four indoor BSs* deployment are outperformed by the *outdoor BSs* deployment and the *indoor-outdoor BSs* deployment. All deployments with mercury/water-filling achieve for a normalized estimation error variance of $\sigma_E^2 = -50\,\mathrm{dB}$ more than 97 % of the average SE achieved with perfect CSI. For $\sigma_E^2 = -20\,\mathrm{dB}$, they achieve between 51 % to 84 % and for $\sigma_E^2 = -10\,\mathrm{dB}$ they achieve between 26 % to 54 % of the average SE achieved with perfect CSI.

Figure 5.13 shows the average SEs versus normalized estimation error variance achieved with local precoding and the same number of BS antennas as in Figure 5.12. We also include the curves of network MIMO with mercury/water-filling from Figure 5.12 for comparison. The SEs of local precoding are unaffected by low normalized estimation error variance and degrade for high normalized estimation error variance only. Inter-cell interference is always present for local precoding and dominates over the interference caused by channel estimation errors for most of the normalized estimation error variance range. It is interesting to see that local precoding outperforms network MIMO for a normalized estimation error variance higher than $-30\,\mathrm{dB}$ to $-15\,\mathrm{dB}$, which is because in network MIMO mercury/water-filling is not aware of the intra-cell interference introduced by the estimation error. However, recall that the performance of network MIMO with estimation errors

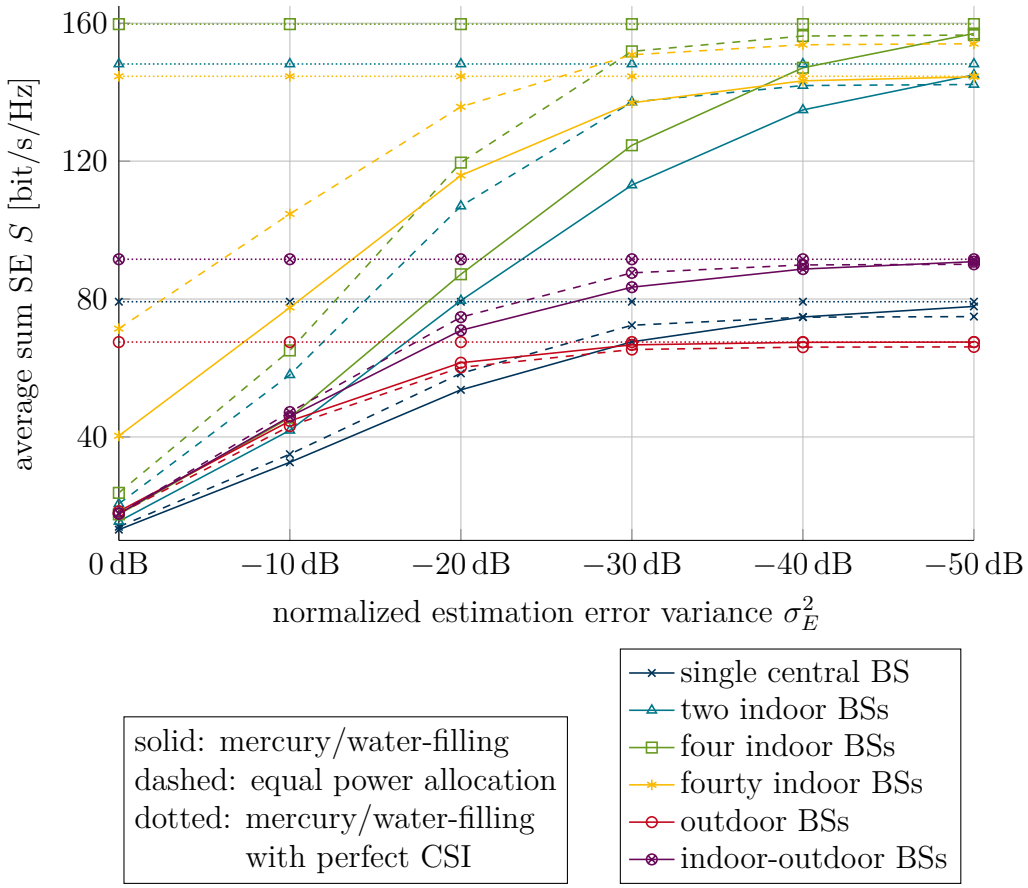

Figure 5.12.: Average SE of Network MIMO with 48 total BS antennas (40 total BS antennas with the *fourty indoor BSs* deployment) for a zero-mean proper complex Gaussian distributed channel estimation error.

can be improved, for example, by making the power allocation more robust to additional interference caused by estimation errors [28].

For more BS antennas the trends and performance differences are similar. We conclude that all deployments suffer from channel estimation noise, while some deployments are more sensitive. Good channel estimation is crucial to obtain the massive MIMO and network MIMO benefits. However, more robust precoding techniques and power allocation schemes could also improve performance in the presence of prediction errors [28].

5.11. Summary

We compared the performance of the BS deployments presented in Chapter 4 with local precoding, orthogonal reuse, LS-MIMO and network MIMO. LS-MIMO and network MIMO provide gains as compared to local precoding, where network MIMO outperforms LS-MIMO. The gains are larger for cooperation between indoor BSs than for coopera-

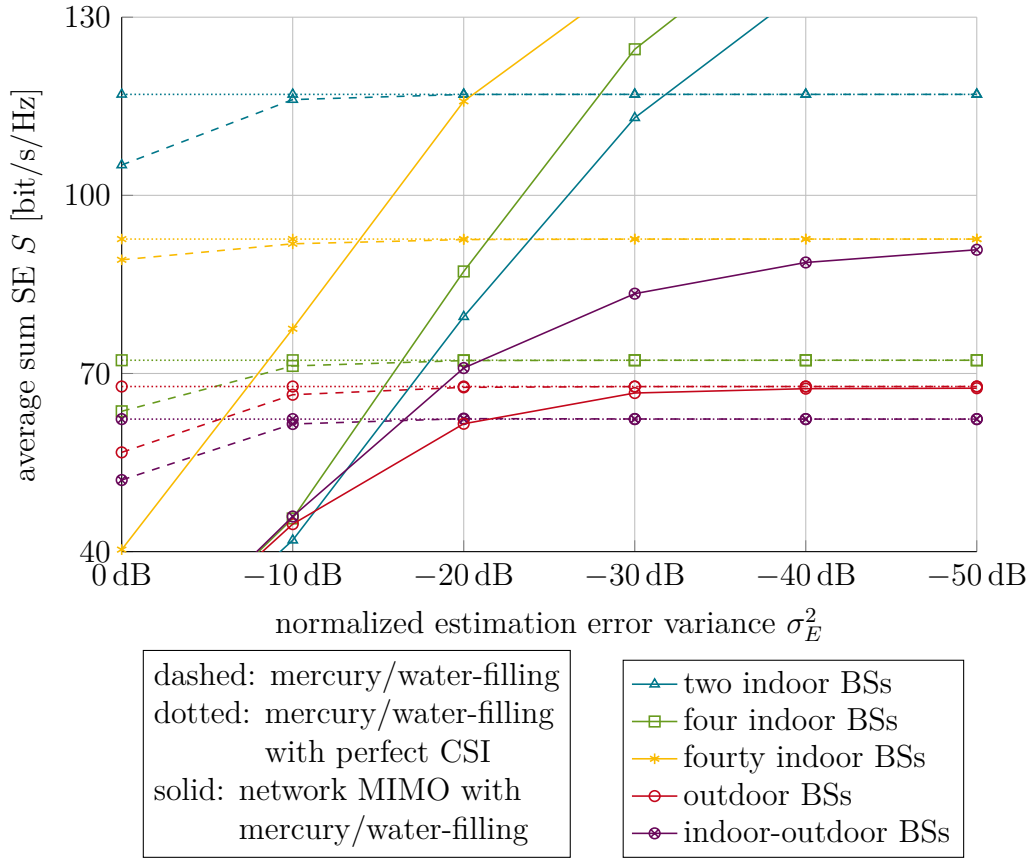

Figure 5.13.: Average SE of local precoding with 48 total BS antennas (40 total BS antennas with the *fourty indoor BSs* deployment) for a zero-mean proper complex Gaussian distributed channel estimation error.

tion between indoor and outdoor BSs. Orthogonal reuse performs worse than the other transmission schemes. The *single central BS* deployment requires more antennas than the deployments with distributed BSs to achieve the same performance. One can trade off the costs of antenna elements with the costs for backhaul capability while achieving the same performance. The positions of the BSs affect the wall penetration losses and the strength of interference. A ratio of twice as many BS antennas as served UEs offers many of the massive MIMO benefits and is a good tradeoff between the number of antennas and SE. The channels harden for two- to four-times as many BS antennas as UEs. User fairness and SE close to capacity are achieved with simple transmission schemes, while the performance difference between the power allocations is small. The singular value spread decreased as the number of BS antennas increased, and behaves similarly to i.i.d. Rayleigh fading channel coefficients and measured channels. The massive MIMO and cooperation benefits are obtained for sufficiently accurate channel estimations only.

A SE of 100 bit/s/Hz without considering overhead is achievable with 192 antennas using local precoding and less than 28 antennas using two or four indoor BSs with network

MIMO. Considering an overhead of 50 %, the required bandwidth to achieve the goals of the METIS (Mobile and wireless communications Enablers for the Twenty-twenty Information Society) project [2] is:

- For the TC1 virtual reality office:

$$\frac{0.1\,\mathrm{Gbit/s/m^2} \cdot 5000\,\mathrm{m^2}}{50\,\mathrm{bit/s/Hz}} = 10\,\mathrm{GHz}. \tag{5.20}$$

  More UE antennas, more base stations, or larger QAM constellations could reduce the required bandwidth.

- For the TC2 dense urban information society:

$$\frac{0.7\,\mathrm{Mbit/s/m^2} \cdot 5000\,\mathrm{m^2}}{50\,\mathrm{bit/s/Hz}} = 70\,\mathrm{MHz}. \tag{5.21}$$

  This performance is achievable with single antenna UEs, few BSs, and 256 QAM within a reasonable bandwidth.

In this part we analyzed massive MIMO given per-BS power constraints. In Part II we analyze a different power constraint, the EIRP constraint.

Part II.

Equivalent Isotropically Radiated Power of MIMO Arrays

6

Introduction to EIRP

The transmission of antennas and antenna arrays is constrained by regulations, for example, set by the International Telecommunication Union (ITU) or by the Federal Communications Commission (FCC). A well known example is the base station (BS) total radiated power constraint, which we called per-BS power constraint in Part I. The equivalent isotropically radiated power (EIRP) constraint is less well known. The regulations define a maximum EIRP depending on the used frequency and on the location where the transmit antennas are placed. The reason for this regulation is to protect other devices and the health of persons in the vicinity of the transmit antennas [85, p. 53]. However, the EIRP constraint is rarely analyzed for multiple-input multiple-output (MIMO) systems.

When multiple antennas are used to transmit in a MIMO system, the signals from the different antennas interfere constructively in certain spacial directions and destructively in other directions. This creates the antenna power pattern. The constructive interference is usually intended, as it potentially increases the received signal power at the receivers. On the other hand, the constructive interference can lead to concentration of electromagnetic energy, which might harm people or other devices. The EIRP measures the highest energy density.

In this chapter, we show how the EIRP is defined and review regulations on EIRP. The next chapter motivates the relevance of EIRP in MIMO systems by analyzing the EIRP in the scenario of Part I. In Chapter 8, we analyze the EIRP of a uniform linear array (ULA) in more detail, by analyzing lower and upper bounds, and by reviewing EIRP aware transmission schemes.

Some works on the EIRP of MIMO systems exist. In [86, 87] it is shown that MIMO transmissions achieve higher performances as compared to single antenna transmissions not only under total radiated power constraints or per-antenna radiated power constraints, but

also under EIRP constraints. However, most works consider the EIRP when a single user equipment (UE) is served, for example, [86–91], while few works consider multiple UEs, for example, [92]. However, the performance given an EIRP constraint and sufficiently many BS antennas increases for multiple UEs being served as compared to a single UE being served [92]. Also, most works on EIRP consider a ULA with isotropic radiators, while few works consider more diverse antennas, for example, [88].

6.1. Definition of EIRP

Equivalent isotropically radiated power (EIRP) or, alternatively, effective isotropically radiated power is the amount of power that a theoretical isotropic antenna (which evenly distributes power in all directions) would emit to produce the peak power density observed in the direction of the maximum antenna and array gain. In other words, the EIRP is the total radiated power multiplied by the antenna and array gain in the direction of the maximal antenna and array gain [93, p. 111]:

$$P_{\mathrm{EIRP}} = P_{\mathrm{t}} G_{\mathrm{t}} \tag{6.1}$$

where P_{t} is the total radiated power and G_{t} is the maximal antenna and array gain. For a single antenna the antenna gain is obtained from measurements or calculations. However, the array gain of an antenna array changes with the precoding.[1] For certain special cases of array configurations and precoding, the array gain can be calculated directly, for example, for ULAs with equal excitation amplitudes [93, Chapter 8], [94, Chapter 6].

The antenna and array gain is

$$G_{\mathrm{t}} = \frac{4\pi U_{\max}}{P_{\mathrm{t}}} \tag{6.2}$$

where $U_{\max}$ is the maximum radiation intensity [93, Section 2.5]. Hence the EIRP is

$$P_{\mathrm{EIRP}} = 4\pi U_{\max}. \tag{6.3}$$

The radiation intensity is the radiated power per unit solid angle [94, Section 2.4]. The maximum radiation intensity is the peak of the power pattern in the far-field

$$U_{\max} = \max_{\substack{\theta\in[0,\pi] \\ \varphi\in[0,2\pi]}} P(\theta, \varphi) \tag{6.4}$$

where θ and φ are the polar angle and the azimuth angle of a sphere around the antenna array center. The power pattern in the far-field is the squared magnitude of the far-zone field pattern $E(\theta, \varphi)$:

$$P(\theta, \varphi) = |E(\theta, \varphi)|^2 . \tag{6.5}$$

[1] Note that the array gain increases with M only for certain precoding and array configurations.

For an antenna array with equal antennas the field pattern is

$$E(\theta,\varphi) = E_{\text{single}}(\theta,\varphi)\, F(\theta,\varphi) \tag{6.6}$$

where $E_{\text{single}}(\theta,\varphi)$ is the field pattern of one antenna and $F(\theta,\varphi)$ is the array factor. The array factor is the field pattern of the array when its antennas are replaced by isotropic antennas but their positions and excitation remain the same [93, Section 8.4]. The field pattern of an isotropic antenna is

$$E_{\text{iso}}(\theta,\varphi) = \frac{1}{\sqrt{4\pi}}. \tag{6.7}$$

For ease of notation we consider isotropic antennas in this work. This leads to the array power pattern

$$\begin{aligned} P(\theta,\varphi) &= \left|E_{\text{iso}}(\theta,\varphi)\, F(\theta,\varphi)\right|^2 \\ &= \frac{1}{4\pi}\left|F(\theta,\varphi)\right|^2. \end{aligned} \tag{6.8}$$

Hence the EIRP of an array with isotropic antennas is determined by the array factor

$$\begin{aligned} P_{\text{EIRP}} &= 4\pi \max_{\substack{\theta\in[0,\pi]\\ \varphi\in[0,2\pi]}} P(\theta,\varphi) \\ &= \max_{\substack{\theta\in[0,\pi]\\ \varphi\in[0,2\pi]}} \left|F(\theta,\varphi)\right|^2. \end{aligned} \tag{6.9}$$

The array factor at the observation point at spatial angle (θ,φ) is the sum of the contributions from the isotropic antennas at the observation point. The contribution of an antenna is the product of the phase rotation times the excitation of the antenna. The phase rotation is determined in the far field by the position of the antenna and the wavelength λ_L. The array manifold vector $\boldsymbol{a}(\theta,\varphi) \in \mathbb{C}^M$ collects the phase rotations and the general expression is

$$\boldsymbol{a}(\theta,\varphi) = \begin{bmatrix} e^{j2\pi\frac{r_1(\theta,\varphi)}{\lambda_L}} \\ \vdots \\ e^{j2\pi\frac{r_M(\theta,\varphi)}{\lambda_L}} \end{bmatrix} \tag{6.10}$$

where $r_m(\theta,\varphi)$ is the distance from the m-th antenna to the observation point on the sphere at spatial angle (θ,φ). We collect the excitations of the antennas at time t in the vector $\boldsymbol{x}(t) \in \mathbb{C}^M$. The array factor is then determined as

$$F(\theta,\varphi) = \boldsymbol{a}(\theta,\varphi)^{\mathsf{T}}\, \boldsymbol{x}(t). \tag{6.11}$$

However, this array factor fluctuates with the excitations and hence with the transmit signals. Usually not the instantaneous peak power density is considered as the EIRP,

but the time-averaged peak power density. EIRP measurements are possible only over a non-zero time period in practice. The length of the measurement period T_{meas} determines how one determines the EIRP. If the measurement period T_{meas} is very short, one must determine the EIRP based on the instantaneous signals $\boldsymbol{x}(t)$. However, if the measurement period T_{meas} is longer than the duration of multiple symbols, then one can determine the EIRP based on the covariance matrix of the transmit signals

$$\boldsymbol{S} = \frac{1}{T_{\text{meas}}} \int_0^{T_{\text{meas}}} \boldsymbol{x}(t)\, \boldsymbol{x}^{\mathsf{H}}(t)\, \mathrm{d}t \in \mathbb{C}^{M \times M}. \tag{6.12}$$

As in [91] we assume a sufficiently long measurement period and hence obtain the EIRP based on the covariance of the transmit signals

$$\begin{aligned} P_{\text{EIRP}} &= \max_{\substack{\theta\in[0,\pi] \\ \varphi\in[0,2\pi]}} \frac{1}{T_{\text{meas}}} \int_0^{T_{\text{meas}}} \left| \boldsymbol{a}(\theta,\varphi)^{\mathsf{T}} \boldsymbol{x}(t) \right|^2 \mathrm{d}t \\ &= \max_{\substack{\theta\in[0,\pi] \\ \varphi\in[0,2\pi]}} \boldsymbol{a}(\theta,\varphi)^{\mathsf{T}} \left(\frac{1}{T_{\text{meas}}} \int_0^{T_{\text{meas}}} \boldsymbol{x}(t)\, \boldsymbol{x}(t)^{\mathsf{H}} \mathrm{d}t \right) \boldsymbol{a}(\theta,\varphi)^{*} \\ &= \max_{\substack{\theta\in[0,\pi] \\ \varphi\in[0,2\pi]}} \boldsymbol{a}(\theta,\varphi)^{\mathsf{T}} \boldsymbol{S} \boldsymbol{a}(\theta,\varphi)^{*}. \end{aligned} \tag{6.13}$$

One can reformulate the EIRP expression as in [92, 95, 96]:

$$\begin{aligned} P_{\text{EIRP}} &= \max_{\substack{\theta\in[0,\pi] \\ \varphi\in[0,2\pi]}} \boldsymbol{a}(\theta,\varphi)^{\mathsf{T}} \boldsymbol{S} \boldsymbol{a}(\theta,\varphi)^{*} \\ &= \max_{\substack{\theta\in[0,\pi] \\ \varphi\in[0,2\pi]}} \operatorname{tr}\left(\boldsymbol{a}(\theta,\varphi)^{\mathsf{T}} \boldsymbol{S} \boldsymbol{a}(\theta,\varphi)^{*} \right) \\ &= \max_{\substack{\theta\in[0,\pi] \\ \varphi\in[0,2\pi]}} \operatorname{tr}\left(\boldsymbol{R}(\theta,\varphi)\, \boldsymbol{S} \right) \\ &= \max_{\substack{\theta\in[0,\pi] \\ \varphi\in[0,2\pi]}} \sum_i \lambda_i(\theta,\varphi) \end{aligned} \tag{6.14}$$

where

$$\boldsymbol{R}(\theta,\varphi) = \boldsymbol{a}(\theta,\varphi)^{*}\, \boldsymbol{a}(\theta,\varphi)^{\mathsf{T}} \in \mathbb{C}^{M \times M} \tag{6.15}$$

and the Eigenvalues $\lambda_i(\theta,\varphi)$ at spatial angle (θ,φ) are

$$\lambda_i(\theta,\varphi) = \operatorname{eig}\left(\boldsymbol{R}(\theta,\varphi)\, \boldsymbol{S} \right). \tag{6.16}$$

6.1.1. EIRP for Linear Precoding

For linear precoding the covariance matrix is obtained from the precoding matrix. The EIRP can be obtained also from the sum of the streams' individual power patterns.

For a linear precoding matrix $\boldsymbol{W} = [w_1, \ldots, w_K] \in \mathbb{C}^{M \times K}$ and independent and identically distributed (i.i.d.) unit power transmit signals $\boldsymbol{s}(t) \in \mathbb{C}^K$, the covariance matrix is

$$\begin{aligned} \boldsymbol{S} &= \frac{1}{T_{\text{meas}}} \int_0^{T_{\text{meas}}} \boldsymbol{W}\boldsymbol{s}(t)\,\boldsymbol{s}^{\mathsf{H}}(t)\,\boldsymbol{W}^{\mathsf{H}} \mathrm{d}t \\ &= \boldsymbol{W} \underbrace{\frac{1}{T_{\text{meas}}} \int_0^{T_{\text{meas}}} \boldsymbol{s}(t)\,\boldsymbol{s}^{\mathsf{H}}(t)\,\mathrm{d}t}_{=\boldsymbol{I}_K} \boldsymbol{W}^{\mathsf{H}} \\ &= \boldsymbol{W}\boldsymbol{W}^{\mathsf{H}} \end{aligned} \tag{6.17}$$

where we assume that T_{meas} is longer than the duration of multiple symbols and shorter than the duration of a precoder.[2] We can also express the covariance matrix as the sum over the K streams' covariance matrices

$$\begin{aligned} \boldsymbol{S} &= \boldsymbol{W}\boldsymbol{W}^{\mathsf{H}} \\ &= \sum_{k=1}^{K} \boldsymbol{w}_k \boldsymbol{w}_k^{\mathsf{H}} \\ &= \sum_{k=1}^{K} \boldsymbol{S}_k \end{aligned} \tag{6.18}$$

where the covariance matrix of the k-th stream is

$$\boldsymbol{S}_k = \boldsymbol{w}_k \boldsymbol{w}_k^{\mathsf{H}} \in \mathbb{C}^{M \times M}. \tag{6.19}$$

For linear precoding one can obtain the EIRP by calculating the array power pattern for each stream and then determining the peak of the sum of the individual power patterns

$$\begin{aligned} P_{\text{EIRP}} &= \max_{\substack{\theta \in [0,\pi] \\ \varphi \in [0,2\pi]}} \boldsymbol{a}(\theta,\varphi)^{\mathsf{T}}\, \boldsymbol{S}\boldsymbol{a}(\theta,\varphi)^{*} \\ &= \max_{\substack{\theta \in [0,\pi] \\ \varphi \in [0,2\pi]}} \boldsymbol{a}(\theta,\varphi)^{\mathsf{T}} \sum_{k=1}^{K} \boldsymbol{w}_k \boldsymbol{w}_k^{\mathsf{H}} \boldsymbol{a}(\theta,\varphi)^{*} \\ &= \max_{\substack{\theta \in [0,\pi] \\ \varphi \in [0,2\pi]}} \sum_{k=1}^{K} \boldsymbol{a}(\theta,\varphi)^{\mathsf{T}}\, \boldsymbol{w}_k \boldsymbol{w}_k^{\mathsf{H}} \boldsymbol{a}(\theta,\varphi)^{*} \\ &= \max_{\substack{\theta \in [0,\pi] \\ \varphi \in [0,2\pi]}} \sum_{k=1}^{K} \left| \boldsymbol{a}(\theta,\varphi)^{\mathsf{T}}\, \boldsymbol{w}_k \right|^2 \end{aligned} \tag{6.20}$$

[2] If T_{meas} is longer than the duration of a precoder one determines the covariance matrix from multiple precoders.

We can also express the EIRP for linear precoding as in (6.14)

$$\begin{aligned} P_{\mathrm{EIRP}} &= \max_{\substack{\theta\in[0,\pi]\\ \varphi\in[0,2\pi]}} \operatorname{tr}\left(\boldsymbol{R}\left(\theta,\varphi\right)\boldsymbol{S}\right) \\ &= \max_{\substack{\theta\in[0,\pi]\\ \varphi\in[0,2\pi]}} \sum_{k=1}^{K} \operatorname{tr}\left(\boldsymbol{R}\left(\theta,\varphi\right)\boldsymbol{S}_k\right). \end{aligned} \tag{6.21}$$

6.1.2. EIRP Lower Bound

To determine the EIRP one should evaluate the power density at infinitely many sample spatial angles, unless the peak power density is known. However, measuring or calculating the power density at infinitely many samples is impossible. For many antennas and many antenna arrays the peak power density is not known, and hence one can only measure or calculate the power density at sample spatial angles. Consider the EIRP estimate formed as the maximal power density at sample spatial angles:

$$\begin{aligned} \underline{P}_{\mathrm{EIRP}} &= \max_{(\theta,\varphi)\in\Phi} P\left(\theta,\varphi\right) \\ &= \max_{(\theta,\varphi)\in\Phi} \operatorname{tr}\left(\boldsymbol{R}\left(\theta,\varphi\right)\boldsymbol{S}\right) \end{aligned} \tag{6.22}$$

where $\Phi = \left\{\left(\theta_1,\varphi_1\right),\ldots,\left(\theta_{N_{\mathrm{Samp}}},\varphi_{N_{\mathrm{Samp}}}\right)\right\}$ is the set of N_{Samp} sample spatial angles. The i-th sample is defined by the polar angle θ_i and the azimuth angle φ_i. Clearly the EIRP estimate is a lower bound since higher peak power densities can occur between the samples, i.e., we have

$$\underline{P}_{\mathrm{EIRP}} \leq P_{\mathrm{EIRP}}. \tag{6.23}$$

The accuracy of the estimate is determined by

- ▷ the distance between samples (and hence the number of samples N_{Samp}),
- ▷ the antenna power patterns,
- ▷ the number M of BS antennas,
- ▷ the positions of the antennas,
- ▷ the covariance of the excitation of the individual antennas,
- ▷ and the wavelength λ_L.

We use the EIRP estimate (6.22) to analyze the EIRP in the scenario of Part I in Chapter 7, while we quantify the accuracy of the estimate for ULAs in Chapter 8. The EIRP estimate (6.22) is used in many works on EIRP and is treated as accurate without further comment, for example, [86–89, 92].

6.1.3. Measuring EIRP

A probe used to measure EIRP naturally has a non-zero size and hence one cannot measure the peak power density, but the average power density of the probe area. The peak average power density is smaller than the peak power density. However, we consider the more strict constraint on the peak power density in this work.

Another issue is that measuring the EIRP of an installed BS can be difficult due to multi-path propagation. One solution is to measure the field strengths in the Fresnel region of the near field and apply further processing to obtain the far field strengths [97].

6.1.4. EIRP of OFDM Transmissions

When orthogonal frequency-division multiplexing (OFDM) is used, the regulations specify if the EIRP is constrained for all subcarriers or per subset of the subcarriers (even down to single subcarriers). Since the subcarriers are orthogonal, the power pattern of each subcarrier is determined individually. The EIRP is then determined as the peak power density of the sum of the power patterns [89].

The power pattern of the f-th subcarrier for linear precoding is

$$P^{(f)}(\theta,\varphi) = \sum_{k=1}^{K} \left| \left(\boldsymbol{a}^{(f)}(\theta,\varphi) \right)^{\mathsf{T}} \boldsymbol{w}_k^{(f)} \right|^2 \tag{6.24}$$

where the array manifold vector $\boldsymbol{a}^{(f)}(\theta,\varphi)$ now depends on the wavelength of the f-th subcarrier and the superscript $^{(f)}$ indicates the subcarrier. The EIRP for the subset $\mathcal{N}_{\mathrm{SC}}$ is then

$$\begin{aligned} P_{\mathrm{EIRP}} &= \max_{\substack{\theta\in[0,\pi] \\ \varphi\in[0,2\pi]}} \sum_{f\in\mathcal{N}_{\mathrm{SC}}} P^{(f)}(\theta,\varphi) \\ &= \max_{\substack{\theta\in[0,\pi] \\ \varphi\in[0,2\pi]}} \sum_{f\in\mathcal{N}_{\mathrm{SC}}} \sum_{k=1}^{K} \left| \left(\boldsymbol{a}^{(f)}(\theta,\varphi) \right)^{\mathsf{T}} \boldsymbol{w}_k^{(f)} \right|^2 \end{aligned} \tag{6.25}$$

where the set of subcarriers indices $\mathcal{N}_{\mathrm{SC}}$ varies from a single index f to all subcarriers $\mathcal{N}_{\mathrm{SC}} = \{1,\ldots,N_{\mathrm{SC}}\}$ depending on the bandwidth for which the EIRP is constrained in the regulation. Again we obtain a lower bound $\underline{P}_{\mathrm{EIRP}}$ as in (6.22) by considering the power densities at sample spatial angles instead of infinitely many spatial angles.

6.1.5. Connection of EIRP to Other Measures

The effective radiated power (ERP) is related to the EIRP. Instead of considering as a reference the power that a theoretical isotropic antenna would emit to produce the peak power density, one uses the power that an ideal half-wave dipole antenna would emit. The two are related as [98]

$$P_{\mathrm{EIRP}} = P_{\mathrm{ERP}} + 2.15\,\mathrm{dB}. \tag{6.26}$$

A similar constraint to the EIRP constraint is the specific absorption rate (SAR) constraint. SAR measures the absorption of electromagnetic energy by the body which causes heating of tissue [96]. The SAR constraint applies especially to devices which are used very closely to the human body, for example, an UE, while the EIRP constraint is more relevant to BSs. The definition of SAR is similar to the definition of EIRP. However, while the EIRP measures the peak power density in all directions, the SAR measures the power densities in one or many worst case directions [96]. The worst case directions are obtained form simulations of the SAR for human tissue models. This must be repeated for every antenna array configuration and is suitable only with few antennas. An analysis of SAR and SAR aware transmission schemes can be found in [96, 99, and the references therein].

6.2. Regulatory EIRP Constraints

We present example regulations which constrain EIRP in wireless communication systems such as Long Term Evolution (LTE), wireless local area network (WLAN) or ultra wide band (UWB).

The ITU provides guidelines for telecommunication systems, for example, LTE, to protect humans from electromagnetic fields [100, Annex B]. Transmitters with a total radiated power up to $P_\mathrm{t} \leq 100\,\mathrm{mW} = 20\,\mathrm{dBm}$ are considered inherently compliant. A transmitter where the EIRP is limited to $P_\mathrm{EIRP} \leq 2\,\mathrm{W} = 33\,\mathrm{dBm}$ is also considered inherently compliant. For larger EIRP the compliance is determined from the accessibility of the transmitter, the ability to spatially concentrate power in one direction, and the used frequency. For LTE the EIRP is constrained for the full bandwidth of an OFDM system.

For WLAN networks EIRP regulations are defined, for example, by the FCC and by the Electronic Communications Committee (ECC). The FCC restricts the total radiated power to $P_\mathrm{EIRP} \leq 1\,\mathrm{W} = 30\,\mathrm{dBm}$. However, this is decreased by 1 dB for each 3 dB exceeding a directional array gain of 6 dB [101]. The directional array gain is calculated as the sum of the maximal directional gain of an individual antenna in dB plus the number of antennas in dB: $10\log_{10}(M)$. This means that with $M = 16$ isotropic antennas the radiated power is restricted by

$$P_\mathrm{t} \leq 30\,\mathrm{dBm} - \frac{10\log_{10}(16) - 6\,\mathrm{dB}}{3} = 28\,\mathrm{dBm} \tag{6.27}$$

and with $M = 128$ isotropic antennas the radiated power is restricted by

$$P_\mathrm{t} \leq 30\,\mathrm{dBm} - \frac{10\log_{10}(128) - 6\,\mathrm{dB}}{3} = 25\,\mathrm{dBm}. \tag{6.28}$$

However, a lower directional gain is accepted but must be proven, for example, it must be shown that the precoding strategy limits the directional gain [101]. The ECC regulations for WLAN define a maximal EIRP of $P_\mathrm{EIRP} \leq 100\,\mathrm{mW} = 20\,\mathrm{dBm}$. For WLAN the EIRP is constrained for the total used bandwidth [89].

The EIRP is regulated by $-41.3\,\mathrm{dBm/MHz}$ for UWB systems [90]. In OFDM-based UWB systems the EIRP is constrained for each single subcarrier [90].

7

EIRP in the Local Area Scenario

This chapter serves to motivate the discussion of EIRP, and to show the relevance of EIRP constraints and of EIRP controlling strategies in a realistic scenario. For this we analyze the EIRP of the BSs in the local area scenario discussed in Part I.

7.1. Simulation Setup

We determine the network MIMO precoder and power allocation with mercury/water-filling for the *single central BS* deployment, the *four indoor BSs* deployment, and the *outdoor BSs* deployment using the simulation parameters given in Section 5.1. We estimate the EIRP for each BS by the lower bound $\underline{P}_{\mathrm{EIRP}}$ from (6.22). For each subcarrier we obtain the power densities at uniformly spaced samples on a sphere around the BS [1]. Then we estimate the EIRP as the maximum of the sum of the power patterns of all subcarriers as in (6.25). As we discuss in Chapter 8 the EIRP lower bound is sufficiently accurate if the number of samples is high enough. Here the number of samples is $N_{\mathrm{samp}} = 1024$. Recall that the 24 UEs are dropped randomly 300 times, that we consider 10 channel realizations per drop, and that the EIRP is determined per BS. Hence we obtain 3000 $\underline{P}_{\mathrm{EIRP}}$ values for each BS from which we determine the cumulative distribution function (CDF).

[1] We obtain uniformly spaced points on a sphere based on the technique in [102].

7.2. EIRP of a Single Base Station

Figure 7.1 shows the CDF of the EIRP lower bound $\underline{P}_{\mathrm{EIRP}}$ for the rectangular array BS of the *single central BS* deployment with the network MIMO scheme.[2] One might expect the EIRP to increase with the number of BS antennas, since more antennas increase the ability to steer transmission power into certain directions. However, the mean $\underline{P}_{\mathrm{EIRP}}$ first decreases from 34.03 dBm for $M = 24$ to 29.65 dBm for $M = 48$. Only then the mean $\underline{P}_{\mathrm{EIRP}}$ increases with an increasing number of BS antennas, as expected. The variance of $\underline{P}_{\mathrm{EIRP}}$ follows a similar trend, which is, however, less pronounced. The initial decrease of $\underline{P}_{\mathrm{EIRP}}$ is explained by two effects:

- For few BS antennas the individual beam patterns are broader and have a smaller peak power density. However, the beam patterns from the precoders of the 24 UEs overlap and hence accumulate to a large $\underline{P}_{\mathrm{EIRP}}$. With an increasing number of BS antennas the beam patterns concentrate power more, but the overlap decreases.

- The effective channel gains after zero-forcing beamforming (ZFBF) are small for few BS antennas. Hence the power is allocated mostly to the strong effective channels. This increases the EIRP as few beam patterns are excited with large powers. With an increasing number of BS antennas the power allocation becomes more uniform.

7.2.1. Example Beam Patterns

Next we study example beam patterns for the BS of the *single central BS* deployment to demonstrate these effects. Figures 7.2, 7.3 and 7.4 show for a single subcarrier the power densities of ZFBF beam patterns with $M = 24$, $M = 48$ and $M = 192$ BS antennas. The distance from the origin indicates the power density in mW. The black mesh is the sum of the power densities of the individual streams which are represented by the colored meshes. In Figure 7.2 we observe that a positive power is allocated to only few precoders when we use the network MIMO scheme with $M = 24$ BS antennas. However, the allocated powers of 0.025 mW to 0.11 mW are large. The combination of large allocated powers and broad, overlapping beam patterns creates a large peak power density of 3.06 mW. In Figure 7.3 the observations are different with $M = 48$ BS antennas. A positive power is allocated to most precoders. However, the allocated powers of 0.005 mW to 0.028 mW are small. The beam patterns also overlap little and hence the peak power density of 1.09 mW is small. Figure 7.4 shows the power densities with $M = 192$ BS antennas. Now a positive power is allocated to all precoders and the allocated powers of 0.0006 mW to 0.0193 mW are smaller than with $M = 48$. Even though the beam patterns do not overlap the peak power density 1.84 mW is larger than with $M = 48$, since the precoding concentrates power in certain directions, for example, so called “pencil beams”.

[2] Recall that for a single BS network MIMO, large-scale MIMO (LS-MIMO) and local precoding are equivalent.

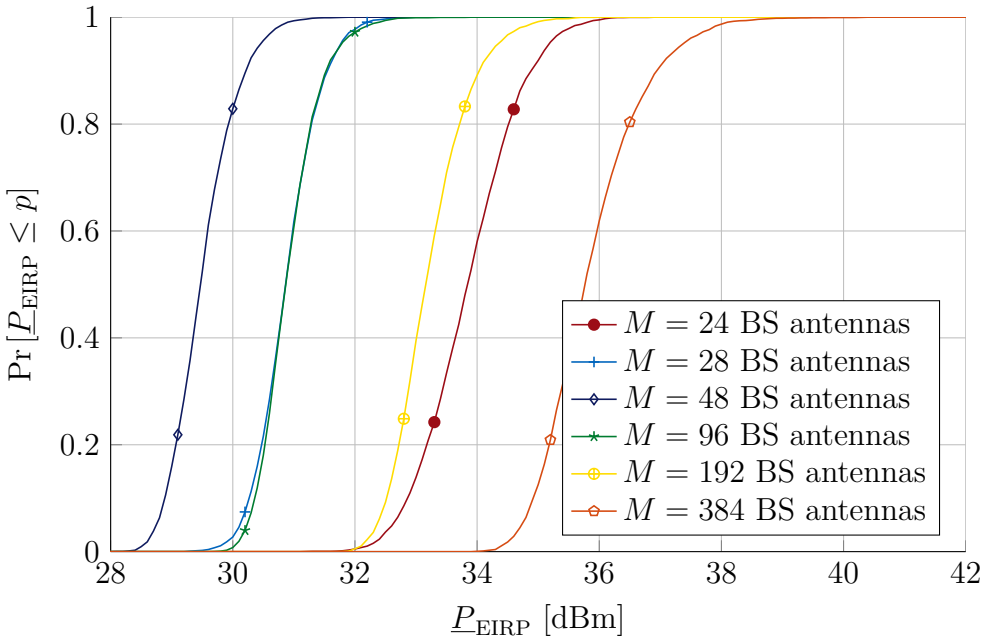

Figure 7.1.: CDF of the EIRP estimate for the rectangular array BS of the *single central BS* deployment with the network MIMO scheme.

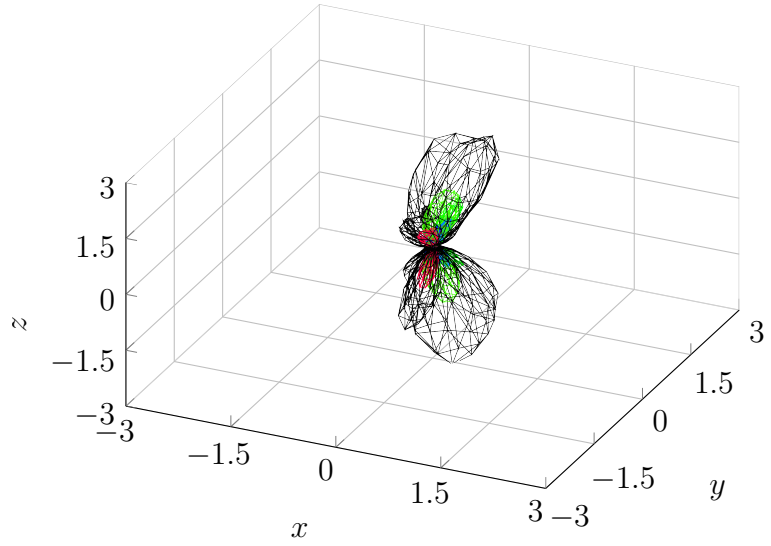

Figure 7.2.: Example beam pattern of a single subcarrier of the rectangular array BS of the *single central BS* deployment with $M = 24$ antennas. The distance from the origin indicates the power density in mW. The black mesh is the sum of the power densities of the individual streams which are represented by the colored meshes.

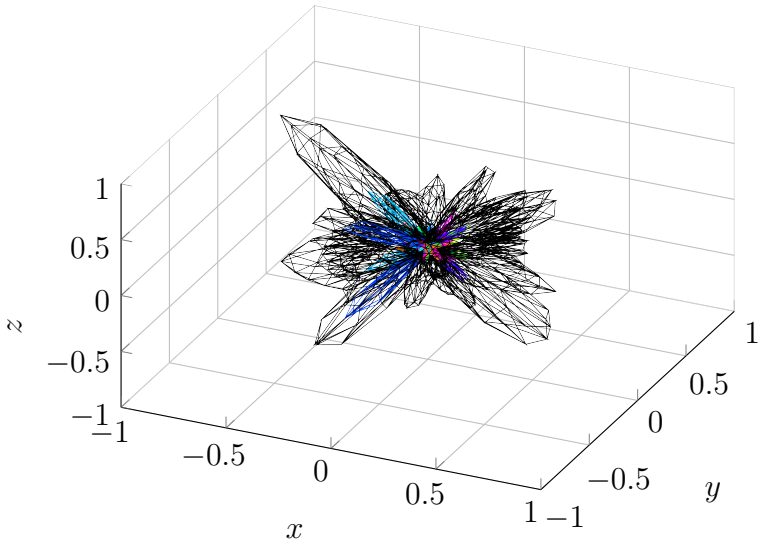

Figure 7.3.: Example beam pattern of a single subcarrier of the rectangular array BS of the *single central BS* deployment with $M = 48$ antennas. The distance from the origin indicates the power density in mW. The black mesh is the sum of the power densities of the individual streams which are represented by the colored meshes.

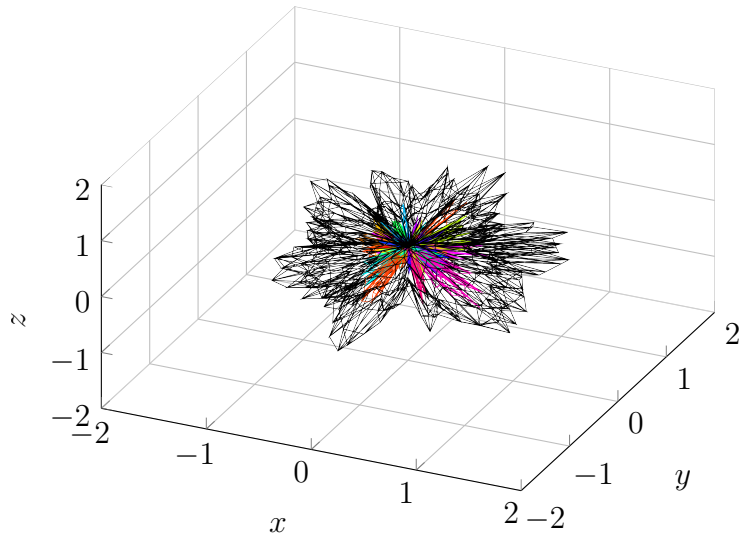

Figure 7.4.: Example beam pattern of a single subcarrier of the rectangular array BS of the *single central BS* deployment with $M = 192$ antennas. The distance from the origin indicates the power density in mW. The black mesh is the sum of the power densities of the individual streams which are represented by the colored meshes.

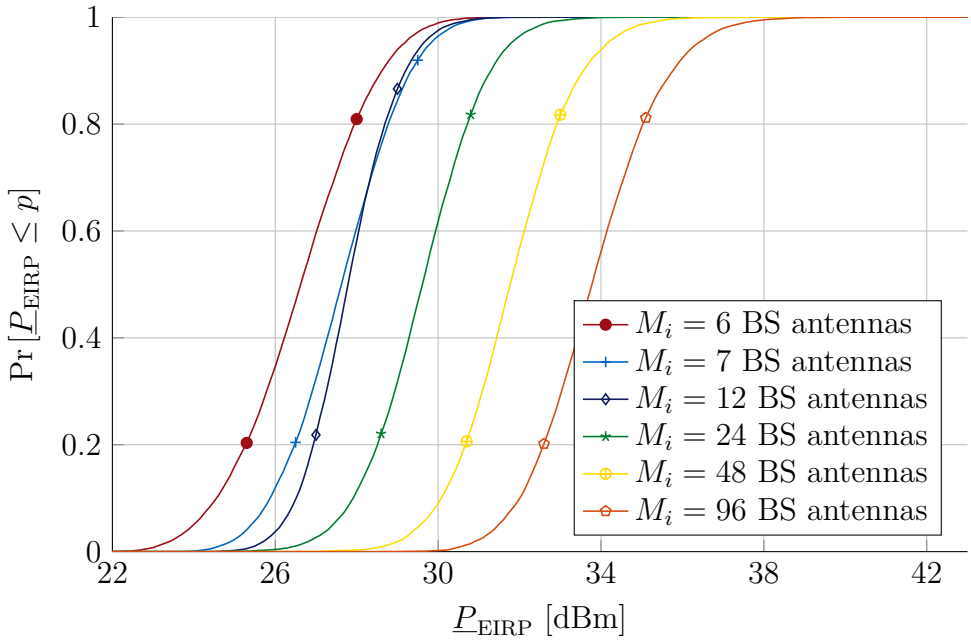

Figure 7.5.: CDF of the EIRP estimate for one rectangular array BS of the *four indoor BSs* deployment with the network MIMO scheme.

7.3. EIRP with Network MIMO

Figure 7.5 shows the CDF of the EIRP lower bound $\underline{P}_{\mathrm{EIRP}}$ for one rectangular array BS of the *four indoor BSs* deployment with the network MIMO scheme. Here the EIRP estimate $\underline{P}_{\mathrm{EIRP}}$ increases with an increasing number of BS antennas. However, the overall values are lower than for the *single central BS* deployment which is due to the maximal per-BS power $P_i = 20\,\mathrm{dBm}$ in the *four indoor BSs* deployment while it is $P_1 = 26\,\mathrm{dBm}$ in the *single central BS* deployment. The same effects as for the *single central BS* deployment determine the trends of the EIRP. However, another effect decreases the EIRP for few BS antennas. Recall that we determine the precoders and the power allocation assuming a total power constraint and then scale the precoders to fulfill the per-BS power constraints. Hence usually most BSs transmit with considerably less power than the per-BS power constraint P_i in the *four indoor BSs* deployment. This effect is most prominent for few BS antennas, where it reduces the EIRP. The effect also causes the larger variance of $\underline{P}_{\mathrm{EIRP}}$.

7.4. EIRP of an Outdoor ULA

Figure 7.6 shows the CDF of the EIRP lower bound $\underline{P}_{\mathrm{EIRP}}$ for one ULA BS of the *outdoor BSs* deployment with the network MIMO scheme. Even though the per-BS power in the *outdoor BSs* deployment is constrained by $P_i = 23\,\mathrm{dBm}$ instead of $P_1 = 26\,\mathrm{dBm}$ in the *single central BS* deployment the EIRP estimates are higher. This is due to the

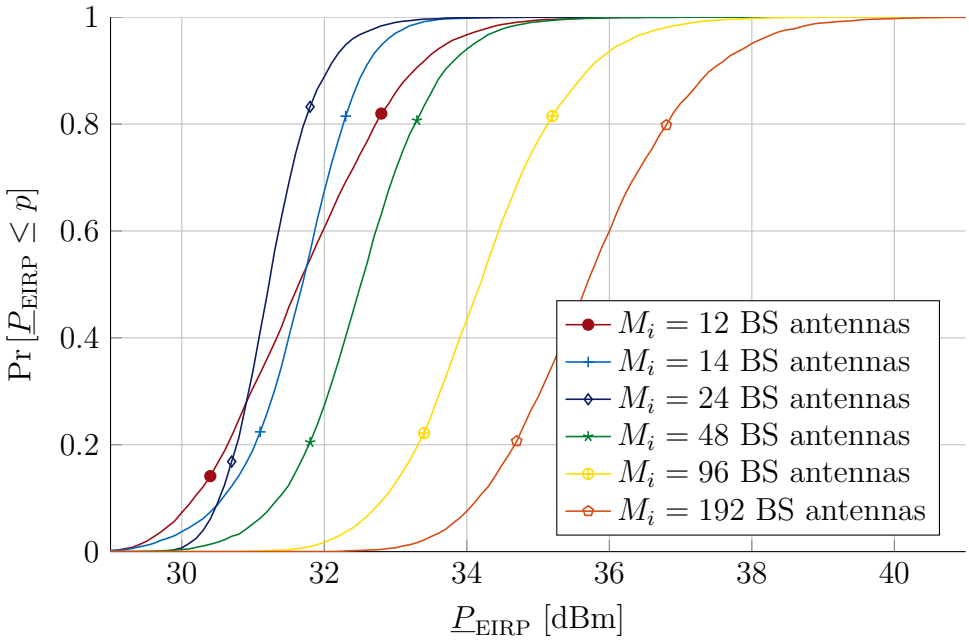

Figure 7.6.: CDF of the EIRP estimate for one ULA BS of the *outdoor BSs* deployment with the network MIMO scheme.

higher spatial concentration of UEs for the outdoor BS compared to the indoor BS of the *single central BS* deployment. This also causes the non-zero probabilities of very high $\underline{P}_{\mathrm{EIRP}}$ values. Here again the EIRP estimate decreases initially and then increases with an increasing number of BS antennas.

7.5. EIRP with Large-Scale MIMO

Up to now we analyzed the EIRP with the network MIMO scheme. Next we analyze it with the LS-MIMO scheme. Figure 7.7 shows the CDF of the EIRP lower bound $\underline{P}_{\mathrm{EIRP}}$ for one rectangular array BS of the *four indoor BSs* deployment with the LS-MIMO scheme. Here the EIRP estimate $\underline{P}_{\mathrm{EIRP}}$ decreases from the fully loaded case $M_i = 24$ to $M_i = 28$ BS antennas and then increases again with an increasing number of BS antennas. The initial decrease is again caused by the power allocation. While the effective channel gains are small and the power is concentrated to few precoders for the fully loaded case, with few additional degrees-of-freedom the power allocation becomes more uniform. Overall the values of $\underline{P}_{\mathrm{EIRP}}$ are lower with LS-MIMO than with network MIMO for the same number M_i of per-BS antennas. This is due to the additional constraints of LS-MIMO which restrict the precoding. The trends for one ULA BS of the *outdoor BSs* deployment with the LS-MIMO scheme are similar.

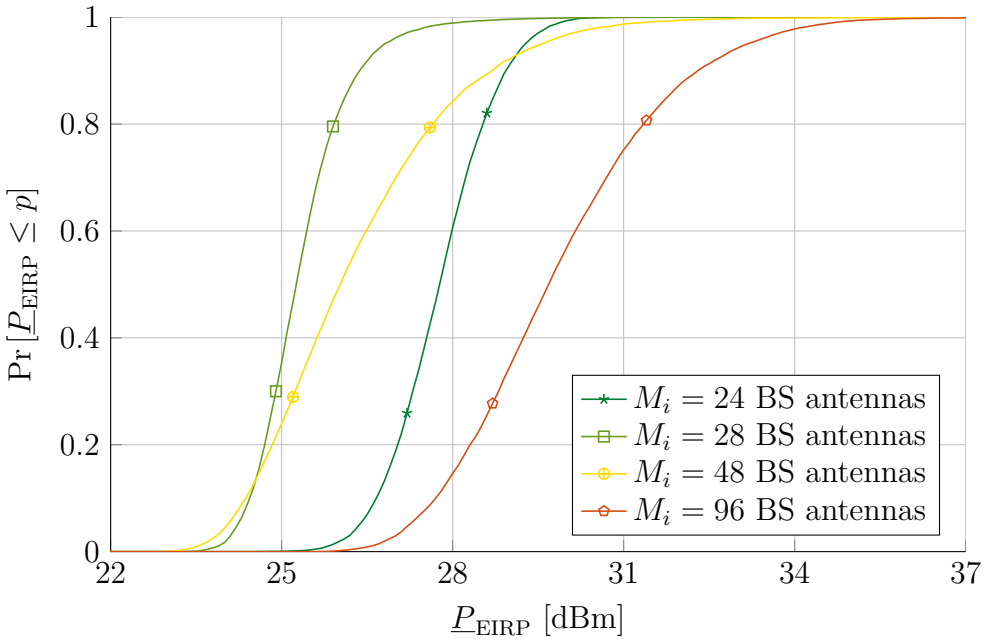

Figure 7.7.: CDF of the EIRP estimate for one rectangular array BS of the *four indoor BSs* deployment with the LS-MIMO scheme.

7.6. Summary

In conclusion, the EIRP increases with an increasing number of BS antennas, though the EIRP sometimes decreases when few degrees-of-freedom are added compared to the fully loaded case. The power allocation has a large impact on the EIRP. If we ignore the power allocation, two trends determine the EIRP as the number of BS antennas increases for ZFBF: The beam patterns overlap less, which reduces EIRP, but at the same time the transmission power becomes more concentrated in intended directions, which increases EIRP. For network MIMO twice as many total BS antennas as served UEs seems to be a good trade-off between EIRP and performance. For LS-MIMO the trade-off is achieved for twice as many per-BS antennas as served UEs. However, with additional degrees-of-freedom one could choose different precoders which might achieve a similar performance at a reduced EIRP. Especially for a large number of BS antennas the many degrees-of-freedom might allow to control EIRP and achieve a performance close to the performance without an EIRP constraint. The EIRP estimates are lower for the LS-MIMO scheme as compared to the network MIMO scheme. For a ULA they are higher as compared to a rectangular array.

We observed that the EIRP estimate in the local area scenario of Part I can be up to 40 dBm, while it is mostly between 24 dBm to 37 dBm. Some EIRP values violate regulatory constraints. However schemes to lower the EIRP exist (see Section 8.7).

Note that, we considered an EIRP estimate which is a lower bound only. Hence the presented results give a first insight only. To guarantee that the EIRP does not exceed

a constraint we must consider EIRP upper bounds. In the next chapter we discuss such bounds for a ULA.

8

EIRP of Uniform Linear Arrays

In this chapter, we analyze the EIRP of ULAs. Lower and upper bounds on the EIRP of a ULA exist for single stream transmission. We review these bounds and propose new bounds which apply to multiple stream transmissions. The combination of upper and lower bounds allows to quantify the accuracy of EIRP estimates. We compare the EIRP bounds and review EIRP aware transmission schemes.

ULA antennas are placed on a line and they are separated by a uniform spacing of

$$d = \tau \lambda_L \tag{8.1}$$

where $\tau > 0$ and $\lambda_L = \frac{c}{f}$ is the wavelength, which is determined by the frequency f and the speed c of electromagnetic waves. Note that in OFDM λ depends on the subcarrier frequency f and τ changes with the subcarrier frequency since d is constant. We assume without loss of generality (w.l.o.g.) that the antennas are placed on a line in the zenith direction as shown in Figure 8.1. For ease of derivations we assume that the antennas are isotropic radiators (point sources) and that there is no mutual coupling between antennas. With these assumptions the array factor becomes symmetric around the zenith direction, i.e., the antenna gain is independent of the azimuth angle φ.

From Figure 8.1 we observe that the phase offset in the far field between the signals from the m-th and the n-th antenna at polar angle θ is

$$\frac{2\pi}{\lambda_L} (n - m)\, d \cos(\theta) = 2\pi\, (n - m)\, \tau \cos(\theta). \tag{8.2}$$

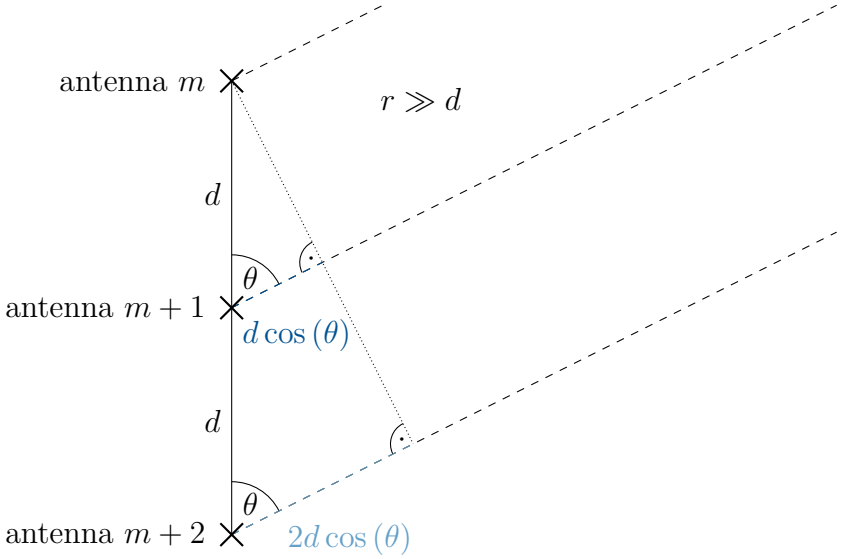

Figure 8.1.: Uniform linear array.

The array manifold vector is defined as

$$\boldsymbol{a}(\theta) = \begin{bmatrix} 1 \\ e^{j2\pi\tau\cos(\theta)} \\ e^{j2\pi 2\tau\cos(\theta)} \\ \vdots \\ e^{j2\pi(M-1)\tau\cos(\theta)} \end{bmatrix}. \tag{8.3}$$

In the following we consider the EIRP of a single subcarrier for ease of notation. One can obtain the EIRP of OFDM transmission by summing the power patterns of the subcarriers as in (6.25), where the array manifold vector depends on the subcarrier frequency.

Recall from Section 6.1.1 that the EIRP with linear precoding is

$$P_{\text{EIRP}} = \max_{\substack{\theta\in[0,\pi] \\ \varphi\in[0,2\pi]}} \sum_{k=1}^{K} \left| \boldsymbol{a}(\theta,\varphi)^{\mathsf{T}} \boldsymbol{w}_k \right|^2. \tag{8.4}$$

For a ULA we can drop the maximization over the azimuth angle. Hence the EIRP of a ULA with linear precoding is

$$\begin{aligned} P_{\text{EIRP}} &= \max_{\theta\in[0,\pi]} \sum_{k=1}^{K} \left| \boldsymbol{a}(\theta)^{\mathsf{T}} \boldsymbol{w}_k \right|^2 \\ &= \max_{\theta\in[0,\pi]} \sum_{k=1}^{K} \operatorname{tr}\left(\boldsymbol{R}(\theta)\, \boldsymbol{S}_k\right) \end{aligned} \tag{8.5}$$

$$= \max_{\theta \in [0,\pi]} \operatorname{tr}\left(\boldsymbol{R}\left(\theta\right) \boldsymbol{S}\right)$$

where $\boldsymbol{S}_k = \boldsymbol{w}_k \boldsymbol{w}_k^{\mathsf{H}}$ is the covariance matrix of the k-th stream with precoder $\boldsymbol{w}_k$ and the full covariance matrix is $\boldsymbol{S} = \sum_{k=1}^{K} \boldsymbol{S}_k$. For a ULA the matrix $\boldsymbol{R}\left(\theta\right)$ simplifies to

$$\begin{aligned} \boldsymbol{R}\left(\theta\right) &= \boldsymbol{a}\left(\theta\right)^{*} \boldsymbol{a}\left(\theta\right)^{\mathsf{T}} \\ &= \begin{bmatrix} 1 & e^{j2\pi\tau\cos(\theta)} & \cdots & e^{j2\pi(M-1)\tau\cos(\theta)} \\ e^{-j2\pi\tau\cos(\theta)} & 1 & \ddots & \vdots \\ \vdots & \ddots & \ddots & e^{j2\pi\tau\cos(\theta)} \\ e^{-j2\pi(M-1)\tau\cos(\theta)} & \cdots & e^{-j2\pi\tau\cos(\theta)} & 1 \end{bmatrix}. \end{aligned} \tag{8.6}$$

8.1. Determining the EIRP with the IDFT

The EIRP of a ULA can be determined with the help of the $N_{\mathrm{IDFT}} \times M$ inverse discrete Fourier transform (IDFT) matrix

$$\boldsymbol{F}_{N_{\mathrm{IDFT}} \times M} = \begin{bmatrix} 1 & 1 & 1 & \cdots & 1 \\ 1 & e^{j2\pi\frac{1}{N_{\mathrm{IDFT}}}} & e^{j2\pi\frac{2}{N_{\mathrm{IDFT}}}} & \cdots & e^{j2\pi\frac{M-1}{N_{\mathrm{IDFT}}}} \\ 1 & e^{j2\pi\frac{2}{N_{\mathrm{IDFT}}}} & e^{j2\pi\frac{4}{N_{\mathrm{IDFT}}}} & \cdots & e^{j2\pi\frac{2(M-1)}{N_{\mathrm{IDFT}}}} \\ \vdots & \vdots & \vdots & \ddots & \vdots \\ 1 & e^{j2\pi\frac{(N_{\mathrm{IDFT}}-1)}{N_{\mathrm{IDFT}}}} & e^{j2\pi\frac{(N_{\mathrm{IDFT}}-1)2}{N_{\mathrm{IDFT}}}} & \cdots & e^{j2\pi\frac{(N_{\mathrm{IDFT}}-1)(M-1)}{N_{\mathrm{IDFT}}}} \end{bmatrix}. \tag{8.7}$$

In [90] the EIRP for a single stream with precoder $\boldsymbol{w}_1$ is determined as

$$P_{\mathrm{EIRP}} = \max_{\theta \in [0,\pi]} \left| \boldsymbol{a}\left(\theta\right)^{\mathsf{T}} \boldsymbol{w}_1 \right|^2 = \lim_{N_{\mathrm{IDFT}} \to \infty} \left\| \boldsymbol{F}_{N_{\mathrm{IDFT}} \times M} \boldsymbol{w}_1 \right\|_{\infty}^2 \tag{8.8}$$

where the supremum norm is the supremum of the magnitudes of the vector elements $\left\|\boldsymbol{r}\right\|_{\infty} = \sup\left\{|r_1|, |r_2|, \ldots, |r_M|\right\}$ of a vector $\boldsymbol{r} = \left[r_1, r_2, \ldots, r_M\right]^{\mathsf{T}} \in \mathbb{C}^M$. The supremum norm is also called infinity norm or uniform norm.

The term $\left| \boldsymbol{a}\left(\theta\right)^{\mathsf{T}} \boldsymbol{w}_1 \right|^2$ equals the squared amplitude of an inverse Fourier transform of the precoder $\boldsymbol{w}_1$ [90]. Hence for a ULA the EIRP is the maximum magnitude of the inverse Fourier transform. Instead of using a continuous inverse Fourier transform one can use an IDFT to approximate the EIRP. We extend the idea of determining the EIRP with the help of the IDFT to multiple transmit streams with different precoders.

Theorem 8.1. The EIRP of a ULA transmitting K streams with linear precoding is

$$P_{\mathrm{EIRP}} = \lim_{N_{\mathrm{IDFT}} \to \infty} \left\| \sum_{k=1}^{K} \left| \boldsymbol{F}_{N_{\mathrm{IDFT}} \times M} \boldsymbol{w}_k \right|^2 \right\|_{\infty} \tag{8.9}$$

where we make a slight abuse of notation by denoting the element-wise magnitude squared of a vector $\boldsymbol{x} \in \mathbb{C}^M$ as

$$|\boldsymbol{x}|^2 = \begin{bmatrix} \left|[\boldsymbol{x}]_{(1)}\right|^2 \\ \vdots \\ \left|[\boldsymbol{x}]_{(M)}\right|^2 \end{bmatrix}. \tag{8.10}$$

Proof. Let $\hat{\theta}$ be the angle where the peak power density is achieved

$$\hat{\theta} = \arg\max_{\theta \in [0,\pi]} \sum_{k=1}^{K} \left| \boldsymbol{a}\left(\theta\right)^{\mathsf{T}} \boldsymbol{w}_k \right|^2. \tag{8.11}$$

As we show in Lemma A.1 in Appendix A the angle $\hat{\theta}$ is unique for $\tau < \frac{1}{2}$, one or two angles $\hat{\theta}$ exist for $\frac{1}{2} \leq \tau < 1$, and multiple angles $\hat{\theta}$ exist for $\tau \geq 1$. At least one $\hat{\theta}$ exists which fulfills

$$-\frac{1}{2} \leq \tau \cos\left(\hat{\theta}\right) < \frac{1}{2}. \tag{8.12}$$

The EIRP is

$$P_{\mathrm{EIRP}} = \sum_{k=1}^{K} \left| \left[1, e^{j2\pi\tau\cos\left(\hat{\theta}\right)}, e^{j2\pi 2\tau\cos\left(\hat{\theta}\right)}, \ldots, e^{j2\pi(M-1)\tau\cos\left(\hat{\theta}\right)}\right]^{\mathsf{T}} \boldsymbol{w}_k \right|^2. \tag{8.13}$$

Note that we can substitute $\hat{\theta}$ by $\tilde{\theta}$ where

$$0 \leq \tau \cos\left(\tilde{\theta}\right) < 1 \tag{8.14}$$

since for $-\frac{1}{2} \leq \tau \cos\left(\hat{\theta}\right) < 0$ there exists a $\tilde{\theta}$ where $\frac{1}{2} \leq \tau \cos\left(\tilde{\theta}\right) < 1$ such that for $0 \leq m < M$

$$e^{j2\pi m\tau\cos\left(\hat{\theta}\right)} = e^{j2\pi m\tau\cos\left(\tilde{\theta}\right)}. \tag{8.15}$$

Then the EIRP is

$$P_{\mathrm{EIRP}} = \sum_{k=1}^{K} \left| \left[1, e^{j2\pi\tau\cos\left(\tilde{\theta}\right)}, e^{j2\pi 2\tau\cos\left(\tilde{\theta}\right)}, \ldots, e^{j2\pi(M-1)\tau\cos\left(\tilde{\theta}\right)}\right]^{\mathsf{T}} \boldsymbol{w}_k \right|^2. \tag{8.16}$$

The n-th row of the IDFT matrix $\boldsymbol{F}_{N_{\mathrm{IDFT}} \times M}$ is

$$\left[\boldsymbol{F}_{N_{\mathrm{IDFT}} \times M}\right]_{(n,:)} = \left[1, e^{j2\pi\frac{n-1}{N_{\mathrm{IDFT}}}}, e^{j2\pi\frac{2(n-1)}{N_{\mathrm{IDFT}}}}, \ldots, e^{j2\pi\frac{(M-1)(n-1)}{N_{\mathrm{IDFT}}}}\right]. \tag{8.17}$$

Let $\hat{n}$ be the index of the row which creates in (8.9) the maximum magnitude

$$\hat{n} = \arg \max_{1 \leq n \leq N_{\mathrm{IDFT}}} \sum_{k=1}^{K} \left| \left[1, e^{j2\pi \frac{n-1}{N_{\mathrm{IDFT}}}}, e^{j2\pi \frac{2(n-1)}{N_{\mathrm{IDFT}}}}, \ldots, e^{j2\pi \frac{(M-1)(n-1)}{N_{\mathrm{IDFT}}}} \right]^{\mathsf{T}} \boldsymbol{w}_k \right|^2 . \tag{8.18}$$

Hence we obtain the maximum entry of the vector $\sum_{k=1}^{K} \left| \boldsymbol{F}_{N_{\mathrm{IDFT}} \times M} \boldsymbol{w}_k \right|^2$ as

$$\left\| \sum_{k=1}^{K} \left| \boldsymbol{F}_{N_{\mathrm{IDFT}} \times M} \boldsymbol{w}_k \right|^2 \right\|_{\infty} = \sum_{k=1}^{K} \left| \left[1, e^{j2\pi \frac{\hat{n}-1}{N_{\mathrm{IDFT}}}}, e^{j2\pi \frac{2(\hat{n}-1)}{N_{\mathrm{IDFT}}}}, \ldots, e^{j2\pi \frac{(M-1)(\hat{n}-1)}{N_{\mathrm{IDFT}}}} \right]^{\mathsf{T}} \boldsymbol{w}_k \right|^2 . \tag{8.19}$$

Now compare the EIRP expression (8.13) and the maximum vector entry (8.19). The only difference between the two terms is in the exponential functions of the array manifold vector and of the row of the IDFT matrix. In (8.16) the exponents contain $\tau \cos\left(\tilde{\theta}\right)$ while they contain $\frac{\hat{n}-1}{N_{\mathrm{IDFT}}}$ in (8.19). The difference $\left| \tau \cos\left(\tilde{\theta}\right) - \frac{\hat{n}-1}{N_{\mathrm{IDFT}}} \right| < \epsilon$ is bounded by the error $\epsilon > 0$ where the error approaches zero as the length of the IDFT matrix approaches infinity $\lim_{N_{\mathrm{IDFT}} \to \infty} \epsilon = 0$. Hence (8.19) becomes arbitrarily close to the EIRP with increasing N_{IDFT}. ■

We obtain a second expression of the EIRP

$$P_{\mathrm{EIRP}} = \lim_{N_{\mathrm{IDFT}} \to \infty} \left\| \mathrm{diag}\left(\boldsymbol{F}_{N_{\mathrm{IDFT}} \times M} \boldsymbol{S} \boldsymbol{F}^{\mathsf{H}}_{N_{\mathrm{IDFT}} \times M} \right) \right\|_{\infty} . \tag{8.20}$$

Here the sum over the power densities of the K streams is replaced by the covariance matrix $\boldsymbol{S}$ of the precoders. To obtain the second expression we transform the term inside the maximum norm of (8.9)

$$\begin{aligned} \sum_{k=1}^{K} \left| \boldsymbol{F}_{N_{\mathrm{IDFT}} \times M} \boldsymbol{w}_k \right|^2 &= \sum_{k=1}^{K} \mathrm{diag}\left(\boldsymbol{F}_{N_{\mathrm{IDFT}} \times M} \boldsymbol{w}_k \boldsymbol{w}_k^{\mathsf{H}} \boldsymbol{F}^{\mathsf{H}}_{N_{\mathrm{IDFT}} \times M} \right) \\ &= \mathrm{diag}\left(\sum_{k=1}^{K} \boldsymbol{F}_{N_{\mathrm{IDFT}} \times M} \boldsymbol{w}_k \boldsymbol{w}_k^{\mathsf{H}} \boldsymbol{F}^{\mathsf{H}}_{N_{\mathrm{IDFT}} \times M} \right) \\ &= \mathrm{diag}\left(\boldsymbol{F}_{N_{\mathrm{IDFT}} \times M} \left(\sum_{k=1}^{K} \boldsymbol{w}_k \boldsymbol{w}_k^{\mathsf{H}} \right) \boldsymbol{F}^{\mathsf{H}}_{N_{\mathrm{IDFT}} \times M} \right) \\ &= \mathrm{diag}\left(\boldsymbol{F}_{N_{\mathrm{IDFT}} \times M} \boldsymbol{S} \boldsymbol{F}^{\mathsf{H}}_{N_{\mathrm{IDFT}} \times M} \right) \end{aligned} \tag{8.21}$$

where we use

$$\left| \boldsymbol{r} \right|^2 = \mathrm{diag}\left(\boldsymbol{r} \boldsymbol{r}^{\mathsf{H}} \right) . \tag{8.22}$$

For a single stream $K = 1$ we reobtain the elegant term (8.8) from [90] from the EIRP expression (8.9) as

$$P_{\mathrm{EIRP}} = \lim_{N_{\mathrm{IDFT}} \to \infty} \left\| \left| \boldsymbol{F}_{N_{\mathrm{IDFT}} \times M} \boldsymbol{w}_1 \right|^2 \right\|_{\infty} \tag{8.23}$$

$$= \lim_{N_{\mathrm{IDFT}}\to\infty} \|\boldsymbol{F}_{N_{\mathrm{IDFT}}\times M}\boldsymbol{w}_1\|_\infty^2 .$$

Note that the EIRP of a multiple stream transmission is less than the sum of the EIRPs of the individual transmissions, which one can conclude from the triangle inequality

$$\lim_{N_{\mathrm{IDFT}}\to\infty} \left\| \sum_{k=1}^{K} |\boldsymbol{F}_{N_{\mathrm{IDFT}}\times M}\boldsymbol{w}_k|^2 \right\|_\infty \leq \lim_{N_{\mathrm{IDFT}}\to\infty} \sum_{k=1}^{K} \|\boldsymbol{F}_{N_{\mathrm{IDFT}}\times M}\boldsymbol{w}_k\|_\infty^2 . \tag{8.24}$$

8.1.1. EIRP Lower Bound for a ULA

For a finite N_{IDFT} the EIRP in (8.9) is not exact. Instead we obtain the EIRP estimate

$$\underline{P}_{\mathrm{EIRP}} = \left\| \sum_{k=1}^{K} |\boldsymbol{F}_{N_{\mathrm{IDFT}}\times M}\boldsymbol{w}_k|^2 \right\|_\infty \tag{8.25}$$

which is a lower bound. The estimate $\underline{P}_{\mathrm{EIRP}}$ samples the power density at N_{IDFT} equally spaced polar angles θ and then determines the maximum power density of the sampled points. These two operations lead to an EIRP lower bound as discussed in Section 6.1.2. We can obtain the same lower bound when using a finite N_{IDFT} in the second EIRP expression (8.20). In [90] the authors suggest that $N_{\mathrm{IDFT}} = 64$ suffices for practical purposes. However, the accuracy of the EIRP lower bound depends on the number M of BS antennas and the number N_{IDFT} of samples. In this chapter, we quantify the accuracy by analyzing EIRP upper bounds and we show that oversampling, i.e., $\frac{N_{\mathrm{IDFT}}}{M} > 1$, is necessary to obtain meaningful bounds.

The number N_{IDFT} of sample polar angles determines the complexity of the EIRP lower bound $\underline{P}_{\mathrm{EIRP}}$. We estimate the computational complexity by counting the number of multiplications and magnitude squared operations. Let the number N_{IDFT} of samples and the number M of BS antennas be powers of two. If $N_{\mathrm{IDFT}} \geq M$ we can use the inverse fast Fourier transform (IFFT) to calculate the length N_{IDFT} IDFT of the vector $\boldsymbol{w}_k$. A length N_{IDFT} IFFT can be implemented with $\frac{N_{\mathrm{IDFT}}}{2}\log_2(N_{\mathrm{IDFT}})$ multiplications [103]. One might be able to reduce the number of multiplications if $N_{\mathrm{IDFT}} > M$ by modifying the IFFT implementation. In case $N_{\mathrm{IDFT}} < M$ we can use a length M IFFT and use only every M/N_{IDFT}-th value from the resulting vector, or we modify the IFFT algorithm. The IFFT is executed K times and the magnitude squared KN_{IDFT} times. Hence the computational complexity of (8.25) is

$$C_{\mathrm{EIRP,IDFT}} = C_{\mathrm{Mul}}\, K \frac{N_{\mathrm{IDFT}}}{2}\log_2(N_{\mathrm{IDFT}}) + C_{\mathrm{MagSq}}\, K N_{\mathrm{IDFT}}. \tag{8.26}$$

where C_{Mul} is the computational complexity of one complex number multiplication and C_{MagSq} is the computational complexity of one magnitude squared operation. The second

option to calculate the EIRP in (8.20) has the computational complexity

$$C_{\mathrm{EIRP,IDFT}} = C_{\mathrm{Mul}} \left(N_{\mathrm{IDFT}} M \left(1 + M\right) + \frac{M \left(M + 1\right)}{2} K \right) \tag{8.27}$$

where $N_{\mathrm{IDFT}} M \left(1 + M\right)$ is the number of multiplications required to calculate the diagonal elements, and $\frac{M(M+1)}{2} K$ is the number of multiplications required to determine the covariance matrix $\boldsymbol{S}$. As one might expect the computational complexity is less when the IFFT is deployed.

8.2. Connection of EIRP to PAPR

The peak-to-average power ratio (PAPR) is usually defined as the ratio of the peak power of a signal divided by its average power. We could define a PAPR in spatial domain: In Section 6.1 we define the maximal power density as $U_{\max}$ while the average power density is $\frac{P_t}{4\pi}$. Hence the PAPR of the transmission power pattern is equal to the antenna and array gain:

$$\mathrm{PAPR} = \frac{U_{\max}}{\frac{P_t}{4\pi}} = G_t. \tag{8.28}$$

If we lower the PAPR of a transmission power pattern then we can increase the radiated power P_t while the EIRP constraint remains fulfilled:

$$P_{\mathrm{EIRP}} = P_t G_t = P_t \, \mathrm{PAPR} \leq P_{\mathrm{EIRP,max}}. \tag{8.29}$$

The conventional PAPR problem occurs for the PAPR of the time domain signal of an OFDM transmission. As we saw in the previous section the EIRP of a ULA is obtained from the "time domain" signal of an IDFT. Hence strategies developed to control the PAPR of OFDM transmissions can be used to control the EIRP of a ULA with few adjustments [90]. We present two of these strategies in Section 8.7.

8.3. Existing EIRP Upper Bounds

Many works, for example, [86–91], assume that the EIRP lower bound obtained from sampling the power density at different polar angles θ provides an accurate estimate of the EIRP $P_{\mathrm{EIRP}} \approx \underline{P}_{\mathrm{EIRP}}$, but they do not verify this assumption. The assumption $P_{\mathrm{EIRP}} \approx \underline{P}_{\mathrm{EIRP}}$ is only a good approximation when sufficiently many samples N_{IDFT} are used. EIRP upper bounds ensure that the EIRP is not greater than $P_{\mathrm{EIRP}} \leq \overline{P}_{\mathrm{EIRP}}$, and are feasible to ensure that EIRP constraints are not violated. For oversampling ratios $\frac{N_{\mathrm{IDFT}}}{M}$ where $\underline{P}_{\mathrm{EIRP}} \approx \overline{P}_{\mathrm{EIRP}}$ one can assume $P_{\mathrm{EIRP}} \approx \underline{P}_{\mathrm{EIRP}}$.

In this section, we review existing upper bounds on the PAPR of an OFDM transmission which allow to bound the EIRP of a single stream transmission with a linear precoder over a ULA. The extension of these bound to multiple streams should be possible but

seems to be non-trivial. Instead we propose new bounds which also apply to multi-stream transmissions in the next section.

8.3.1. Upper Bound for Critical Sampling

Sampling at the Nyquist rate is called critical sampling. In [104] an upper bound on the PAPR of an OFDM transmission based on the peak power of Nyquist rate samples is given. This upper bound also applies to the EIRP of a ULA when the number of sample polar angles is equal to the number of antennas $N_{\mathrm{IDFT}} = M$. If the peak power density from M samples is $\underline{P}_{\mathrm{EIRP}}$ then the EIRP is bounded as [104]

$$P_{\mathrm{EIRP}} \leq \overline{P}_{\mathrm{EIRP,[104]}} = \left(\frac{2}{\pi}\log_e\left(2M\right) + 2\right)^2 \underline{P}_{\mathrm{EIRP}}. \tag{8.30}$$

8.3.2. Upper Bounds for Oversampling

Many upper bounds on the PAPR of an OFDM transmission exist when the time domain signal is oversampled. In [105] the PAPR of an OFDM transmission is upper bounded if the time domain signal is oversampled at least twice. The result bounds the EIRP of a ULA where $\underline{P}_{\mathrm{EIRP}}$ is the peak power density from $N_{\mathrm{IDFT}} \geq 2M$ polar angle samples [105]:

$$P_{\mathrm{EIRP}} \leq \overline{P}_{\mathrm{EIRP,[105]}} = \frac{1}{\cos^2\left(\frac{\pi}{2}\frac{N_{\mathrm{IDFT}}}{M}\right)} \underline{P}_{\mathrm{EIRP}}. \tag{8.31}$$

This is the tightest bound we found in literature. A similar, but looser bound is obtained in [106]. It bounds the EIRP of a ULA if there are more than $N_{\mathrm{IDFT}} > \frac{\pi}{\sqrt{2}}M$ polar angle samples [106]:

$$P_{\mathrm{EIRP}} < \overline{P}_{\mathrm{EIRP,[106]}} = \frac{\left(\frac{N_{\mathrm{IDFT}}}{M}\right)^2}{\left(\frac{N_{\mathrm{IDFT}}}{M}\right)^2 - \frac{\pi^2}{2}} \underline{P}_{\mathrm{EIRP}}. \tag{8.32}$$

8.4. Proposed EIRP Upper Bounds

In this section, we propose two upper bounds on the EIRP of a ULA with linear precoding. These upper bounds are valid for single and multiple stream transmissions. Instead of sampling the power density these bounds require the covariance matrix only. They have low computational complexities if the covariance is available. The worst case upper bound is mostly interesting to gain insights and it is very loose. However, the second upper bound based on the covariance matrix provides a meaningful bound on the EIRP without sampling.

8.4.1. Worst Case Upper Bound

In the worst case the transmissions from all antennas interfere constructively in at least one direction.

Theorem 8.2. The EIRP of an ULA with linear precoding is upper bounded as:

$$P_{\text{EIRP}} \leq \overline{P}_{\text{EIRP,worst}} = \sum_{m=1}^{M} \sum_{l=1}^{M} \left| [\boldsymbol{S}]_{(m,l)} \right|. \tag{8.33}$$

Proof. We derive the worst case upper bound as

$$\begin{aligned} P_{\text{EIRP}} &= \max_{\theta \in [0,\pi]} \operatorname{tr}\left(\boldsymbol{S}\boldsymbol{R}\left(\theta\right)\right) \\ &\overset{\text{(a)}}{=} \max_{\theta \in [0,\pi]} \mathbf{1}^{\mathsf{T}} \left(\boldsymbol{S} \odot \boldsymbol{R}\left(\theta\right)^{\mathsf{T}}\right) \mathbf{1} \\ &\overset{\text{(b)}}{\leq} \max_{\left|[\tilde{\boldsymbol{R}}]_{(m,n)}\right| = 1, \forall m,n} \mathbf{1}^{\mathsf{T}} \left(\boldsymbol{S} \odot \tilde{\boldsymbol{R}}^{\mathsf{T}}\right) \mathbf{1} \\ &= \sum_{m=1}^{M} \sum_{l=1}^{M} \left| [\boldsymbol{S}]_{(m,l)} \right| \end{aligned} \tag{8.34}$$

where for (a) we use a result from [107]:

$$\operatorname{tr}\left(\boldsymbol{A}\boldsymbol{B}\right) = \mathbf{1}^{\mathsf{T}} \left(\boldsymbol{A} \odot \boldsymbol{B}^{\mathsf{T}}\right) \mathbf{1} \tag{8.35}$$

and $\mathbf{1}$ is the all ones vector. This property means that the trace of the multiplication of two matrices is the sum over the elements of the Hadamard product of the two matrices. For (b) we relax the optimization from the set of array manifold matrices $\boldsymbol{R}\left(\theta\right) = \boldsymbol{a}\left(\theta\right)^{*} \boldsymbol{a}\left(\theta\right)^{\mathsf{T}}$ to the set of all matrices with unit magnitude entries. The array manifold matrices are a subset of all matrices with unit magnitude entries, i.e., entries that only rotate the phase. ■

Note that the worst case upper bound can easily be extended to any antenna array with linear precoding and isotropic antennas.

For a single stream the worst case upper bound assumes that the signals from all antennas interfere constructively in at least one direction

$$\begin{aligned} \overline{P}_{\text{EIRP,worst}} &= \sum_{m=1}^{M} \sum_{l=1}^{M} \left| [\boldsymbol{S}]_{(m,l)} \right| \\ &= \sum_{m=1}^{M} \sum_{l=1}^{M} \left| [\boldsymbol{w}_1]_{(m)} \, [\boldsymbol{w}_1]_{(l)}^{*} \right| \\ &= \sum_{m=1}^{M} \sum_{l=1}^{M} \left| [\boldsymbol{w}_1]_{(m)} \right| \left| [\boldsymbol{w}_1]_{(l)} \right| \end{aligned} \tag{8.36}$$

$$= \left(\sum_{m=1}^{M} \left| [\boldsymbol{w}_1]_{(m)} \right| \right)^2 .$$

Hence the worst case upper bound $\overline{P}_{\text{EIRP,worst}}$ equals the maximal potential array gain for a single stream. For a ULA the potential array gain increases in dB with $10 \log_{10}(M)$. However, usually the real array gain (especially for the transmission of multiple streams) is smaller. For multiple streams the interpretation is not as intuitive, since the signals of the different streams are pointing in different spatial directions at the antennas.

8.4.2. Upper Bound Based on the Covariance Matrix

The existing upper bounds, except for the worst case upper bound, are based on the peak power density at sample polar angles. Here we propose a meaningful upper bound which does not require sampling but relies solely on the covariance matrix.

Theorem 8.3. The EIRP of an ULA is upper-bounded as

$$P_{\text{EIRP}} \leq \overline{P}_{\text{EIRP,cov}} = \operatorname{tr}(\boldsymbol{S}) + 2 \sum_{m=1}^{M-1} \left| \sum_{l=1}^{M-m} [\boldsymbol{S}]_{(l+m,l)} \right| . \tag{8.37}$$

Proof. To prove Theorem 8.3 first note that for a complex $z = |z| e^{j\angle z}$ and an integer $m \in \mathbb{Z}$, we have

$$z^m = |z|^m e^{jm\angle z} \tag{8.38}$$

which allows us to write $\boldsymbol{R}(\theta)$ compactly as

$$\boldsymbol{R}(\theta) = \begin{bmatrix} \omega^0 & \omega^1 & \cdots & \omega^{M-2} & \omega^{M-1} \\ \omega^{-1} & \omega^0 & \cdots & \omega^{M-3} & \omega^{M-2} \\ \vdots & \vdots & \ddots & \vdots & \vdots \\ \omega^{-M+2} & \omega^{-M+3} & \cdots & \omega^0 & \omega^1 \\ \omega^{-M+1} & \omega^{-M+2} & \cdots & \omega^{-1} & \omega^0 \end{bmatrix} \tag{8.39}$$

where $\omega = e^{j2\pi\tau\cos(\theta)}$. Second, observe that for $z_m = |z_m| e^{j\angle z_m} \in \mathbb{C}$ and $\alpha_m \in \mathbb{R}$ we have

$$\begin{aligned} z_m e^{j\alpha_m} + z_m^* e^{-j\alpha_m} &= 2 \operatorname{Re}\left\{ z_m e^{j\alpha_m} \right\} \\ &\leq 2 \left| z_m e^{j\alpha_m} \right| \\ &= 2 \left| z_m \right| \end{aligned} \tag{8.40}$$

and we obtain the second property

$$\max_{\boldsymbol{\alpha} \in \mathbb{R}^{M-1}} \sum_{m=1}^{M-1} \left(z_m e^{j\alpha_m} + z_m^* e^{-j\alpha_m} \right) \leq 2 \sum_{m=1}^{M-1} |z_m| \tag{8.41}$$

where $\boldsymbol{\alpha} = [\alpha_1, \ldots, \alpha_{M-1}]^{\mathsf{T}}$.

Now we upper bound the EIRP as

$$\begin{aligned}
P_{\mathrm{EIRP}} &= \max_{\theta\in[0,\pi]} \operatorname{tr}\left(\boldsymbol{R}(\theta)\,\boldsymbol{S}\right) \\
&\overset{\text{(a)}}{=} \max_{\theta\in[0,\pi]} \mathbf{1}^{\mathsf{T}}\left(\boldsymbol{R}(\theta)\odot\boldsymbol{S}^{\mathsf{T}}\right)\mathbf{1} \\
&\overset{\text{(b)}}{=} \max_{\theta\in[0,\pi]} \left(\sum_{m=1}^{M-1}\omega^{-m}\sum_{l=1}^{M-m}\left[\boldsymbol{S}^{\mathsf{T}}\right]_{(l+m,l)} + \operatorname{tr}\left(\boldsymbol{S}^{\mathsf{T}}\right) + \sum_{m=1}^{M-1}\omega^{m}\sum_{l=1}^{M-m}\left[\boldsymbol{S}^{\mathsf{T}}\right]_{(l,l+m)}\right) \\
&= \operatorname{tr}(\boldsymbol{S}) + \max_{\theta\in[0,\pi]} \left(\sum_{m=1}^{M-1}\omega^{-m}\sum_{l=1}^{M-m}[\boldsymbol{S}]_{(l,l+m)} + \sum_{m=1}^{M-1}\omega^{m}\sum_{l=1}^{M-m}[\boldsymbol{S}]_{(l+m,l)}\right) \qquad (8.42)\\
&\overset{\text{(c)}}{=} \operatorname{tr}(\boldsymbol{S}) + \max_{\theta\in[0,\pi]} \left(\sum_{m=1}^{M-1}\left(\omega^{-m}\sum_{l=1}^{M-m}[\boldsymbol{S}]^{*}_{(l+m,l)} + \omega^{m}\sum_{l=1}^{M-m}[\boldsymbol{S}]_{(l+m,l)}\right)\right) \\
&= \operatorname{tr}(\boldsymbol{S}) + \max_{\theta\in[0,\pi]} \left(\sum_{m=1}^{M-1}\left(\omega^{m}\left(\sum_{l=1}^{M-m}[\boldsymbol{S}]_{(l+m,l)}\right) + \omega^{-m}\left(\sum_{l=1}^{M-m}[\boldsymbol{S}]_{(l+m,l)}\right)^{*}\right)\right) \\
&\overset{\text{(d)}}{\leq} \operatorname{tr}(\boldsymbol{S}) + 2\sum_{m=1}^{M-1}\left|\sum_{l=1}^{M-m}[\boldsymbol{S}]_{(l+m,l)}\right| = \overline{P}_{\mathrm{EIRP,cov}}
\end{aligned}$$

where for (a) we use (8.35), for (b) we use the (off-)diagonal structure of $\boldsymbol{R}(\theta)$ in (8.39), for (c) we use that covariance matrices are Hermitian, i.e., $[\boldsymbol{S}]_{(l,m)} = [\boldsymbol{S}]^{*}_{(m,l)}$, and for (d) we use the second property (8.41). ■

Note that we have equality till (d), hence one might be able to improve the bound by finding a better inequality to replace (8.41).

We can reformulate Theorem 8.3 due to the Hermitian covariance matrix as

$$\begin{aligned}
P_{\mathrm{EIRP}} &\leq \operatorname{tr}(\boldsymbol{S}) + 2\sum_{m=1}^{M-1}\left|\sum_{l=1}^{M-m}[\boldsymbol{S}]_{(l+m,l)}\right| \\
&= \operatorname{tr}(\boldsymbol{S}) + 2\sum_{m=1}^{M-1}\left|\sum_{l=1}^{M-m}[\boldsymbol{S}]_{(l,l+m)}\right| \qquad (8.43)\\
&= \sum_{m=1}^{M-1}\left|\sum_{l=1}^{M-m}[\boldsymbol{S}]_{(l,l+m)}\right| + \operatorname{tr}(\boldsymbol{S}) + \sum_{m=1}^{M-1}\left|\sum_{l=1}^{M-m}[\boldsymbol{S}]_{(l+m,l)}\right|.
\end{aligned}$$

The EIRP for a ULA is upper bounded by the magnitudes of the sums of the (off-)diagonals of the covariance matrix of the transmit signals.

The computational complexity of the proposed EIRP upper bound $\overline{P}_{\mathrm{EIRP,cov}}$ is

$$C_{\mathrm{EIRP,cov}} = C_{\mathrm{Mul}}\,\frac{M\,(M+1)}{2}K + C_{\mathrm{MagSq}}\,(M-1)\,. \qquad (8.44)$$

The computational complexity $C_{\mathrm{EIRP,cov}}$ of the upper bound $\overline{P}_{\mathrm{EIRP,cov}}$ is higher than the

complexity $C_{\text{EIRP,IDFT}}$ of the upper bounds based on sampling for low to medium oversampling rates $\frac{N_{\text{IDFT}}}{M}$. The main contributor to the computational complexity is the calculation of the covariance matrix. However, if the covariance matrix is already calculated for other signal processing steps at the transmitter, the computational complexity of the proposed upper bound is very low.

The presented EIRP upper bound $\overline{P}_{\text{EIRP,cov}}$ also serves to upper bound the PAPR of an OFDM transmission due to its connection with the EIRP of a ULA (see Section 8.2).

8.5. Three Antenna Example

In this section, we analyze the EIRP of a ULA with $M = 3$ antennas in a different way to get more insights. The same steps can be applied to ULAs with more antennas.

Consider a ULA with $M = 3$ antennas which transmits a single stream with linear precoding. The spacing between the antennas is $d = \tau\lambda_L$. W.l.o.g. let the precoding vector be

$$\boldsymbol{w} = \begin{bmatrix} a_1 \\ a_2 e^{j\varphi_2} \\ a_3 e^{j\varphi_3} \end{bmatrix} \tag{8.45}$$

where $a_1, a_2, a_3 \in \mathbb{R}$ and $\varphi_2, \varphi_3 \in [0, 2\pi]$. The EIRP is

$$\begin{aligned} P_{\text{EIRP}} &= \max_{\theta\in[0,\pi]} \left|\boldsymbol{a}\left(\theta\right)\boldsymbol{w}\right|^2 \\ &= \max_{\theta\in[0,\pi]} \left|a_1 + a_2 e^{j(\varphi_2 + 2\pi\tau\cos(\theta))} + a_3 e^{j(\varphi_3 + 4\pi\tau\cos(\theta))}\right|^2 \\ &= \max_{\theta\in[0,\pi]} \Big[a_1^2 + a_2^2 + a_3^2 + 2a_1a_2\cos\left(\varphi_2 + 2\pi\tau\cos(\theta)\right) \\ &\quad + 2a_1a_3\cos\left(\varphi_3 + 4\pi\tau\cos(\theta)\right) + 2a_2a_3\cos\left(\varphi_3 - \varphi_2 + 2\pi\tau\cos(\theta)\right)\Big] \\ &= a_1^2 + a_2^2 + a_3^2 + \max_{\theta\in[0,\pi]} \big[2a_1a_3\cos\left(\varphi_3 + 4\pi\tau\cos(\theta)\right) \\ &\quad + 2a_1a_2\cos\left(\varphi_2 + 2\pi\tau\cos(\theta)\right) + 2a_2a_3\cos\left(\varphi_3 - \varphi_2 + 2\pi\tau\cos(\theta)\right)\big]. \end{aligned} \tag{8.46}$$

If we assume that there exists a θ where all cosinusoidal functions in (8.46) are maximal we recover the worst case upper bound:

$$\begin{aligned} P_{\text{EIRP}} &\leq a_1^2 + a_2^2 + a_3^2 + 2a_1a_3 + 2a_1a_2 + 2a_2a_3 \\ &= \left(a_1 + a_2 + a_3\right)^2 \\ &= \sum_{m=1}^{3}\sum_{l=1}^{3} \left|[\boldsymbol{S}]_{(m,l)}\right| = \overline{P}_{\text{EIRP,worst}}. \end{aligned} \tag{8.47}$$

This upper bound is usually too loose as the cosinusoidal functions usually do not super-

impose completely constructively. However, note that for $M = 2$ antennas, i.e., $a_3 = 0$, only one cosinusoidal function remains and hence the worst case upper bound is tight for $M = 2$. This result shows that antenna selection is optimal for the transmission of a single stream and $M = 2$ [91].

If we treat the term $\cos(\theta) \in [-1, 1]$ in (8.46) as a time variable, we obtain constant terms which equal the transmit power, and three harmonic oscillations: two with the frequency $2\pi\tau$ and one with twice the frequency $4\pi\tau$. The harmonic addition theorem, which we discuss in detail in Lemma A.2 in Appendix A, allows to express cosinusoidal functions with the same frequency as one cosinusoidal function. Hence we express the two functions with frequency $2\pi\tau$ as

$$\begin{aligned} &2a_1a_2\cos\left(\varphi_2 + 2\pi\tau\cos(\theta)\right) + 2a_2a_3\cos\left(\varphi_3 - \varphi_2 + 2\pi\tau\cos(\theta)\right) \\ &= 2a_2\tilde{a}\cos\left(\tilde{\varphi} + 2\pi\tau\cos(\theta)\right) \end{aligned} \tag{8.48}$$

where

$$\tilde{a} = \sqrt{a_1^2 + a_3^2 + 2a_1a_3\cos\left(2\varphi_2 - \varphi_3\right)} \tag{8.49}$$

and

$$\tilde{\varphi} = \cos^{-1}\left(\frac{a_1\cos\left(\varphi_2\right) + a_3\cos\left(-\varphi_2 + \varphi_3\right)}{\sqrt{a_1^2 + a_3^2 + 2a_1a_3\cos\left(2\varphi_2 - \varphi_3\right)}}\right). \tag{8.50}$$

The EIRP becomes

$$\begin{aligned} P_{\text{EIRP}} = a_1^2 + a_2^2 + a_3^2 + \max_{\theta\in[0,\pi]} &\left[2a_1a_3\cos\left(\varphi_3 + 4\pi\tau\cos(\theta)\right)\right. \\ &\left. + 2a_2\tilde{a}\cos\left(\tilde{\varphi} + 2\pi\tau\cos(\theta)\right)\right]. \end{aligned} \tag{8.51}$$

Observing $a_2\tilde{a} = \left|[\boldsymbol{S}]_{(2,1)} + [\boldsymbol{S}]_{(3,2)}\right|$ and assuming that there exists a θ where both cosinusoidal functions are maximal, we recover the upper bound $\overline{P}_{\text{EIRP,cov}}$ proposed in Theorem 8.3:

$$P_{\text{EIRP}} \leq \underbrace{a_1^2 + a_2^2 + a_3^2}_{=\operatorname{tr}(\boldsymbol{S})} + \underbrace{2a_2\tilde{a}}_{=2\left|[\boldsymbol{S}]_{(2,1)}+[\boldsymbol{S}]_{(3,2)}\right|} + \underbrace{2a_1a_3}_{=2\left|[\boldsymbol{S}]_{(3,3)}\right|} = \overline{P}_{\text{EIRP,cov}}. \tag{8.52}$$

We complete the section by discussing the power density terms of an example precoder in Figure 8.2. The example precoder has normalized transmit power, i.e., $a_1^2 + a_2^2 + a_3^2 = 1$. The first two curves are the cosinusoidal functions $2a_1a_2\cos\left(\varphi_2 + 2\pi\tau\cos(\theta)\right)$ and $2a_2a_3\cos\left(\varphi_3 - \varphi_2 + 2\pi\tau\cos(\theta)\right)$ which have the same frequency. One could interpret these functions as the power density variations caused by the interference of the transmissions from the first and second antenna, and from the second and third antenna, respectively. Their sum is the third curve $2a_1\tilde{a}\cos\left(\tilde{\varphi} + 2\pi\tau\cos(\theta)\right)$. Note that the amplitude of this cosinusoidal function is less than the amplitudes of the individual functions. This is considered in the proposed upper bound based on the covariance matrix $\overline{P}_{\text{EIRP,cov}}$, while the worst case upper bound $\overline{P}_{\text{EIRP,worst}}$ assumes that the amplitudes of the individual cosinusoidal

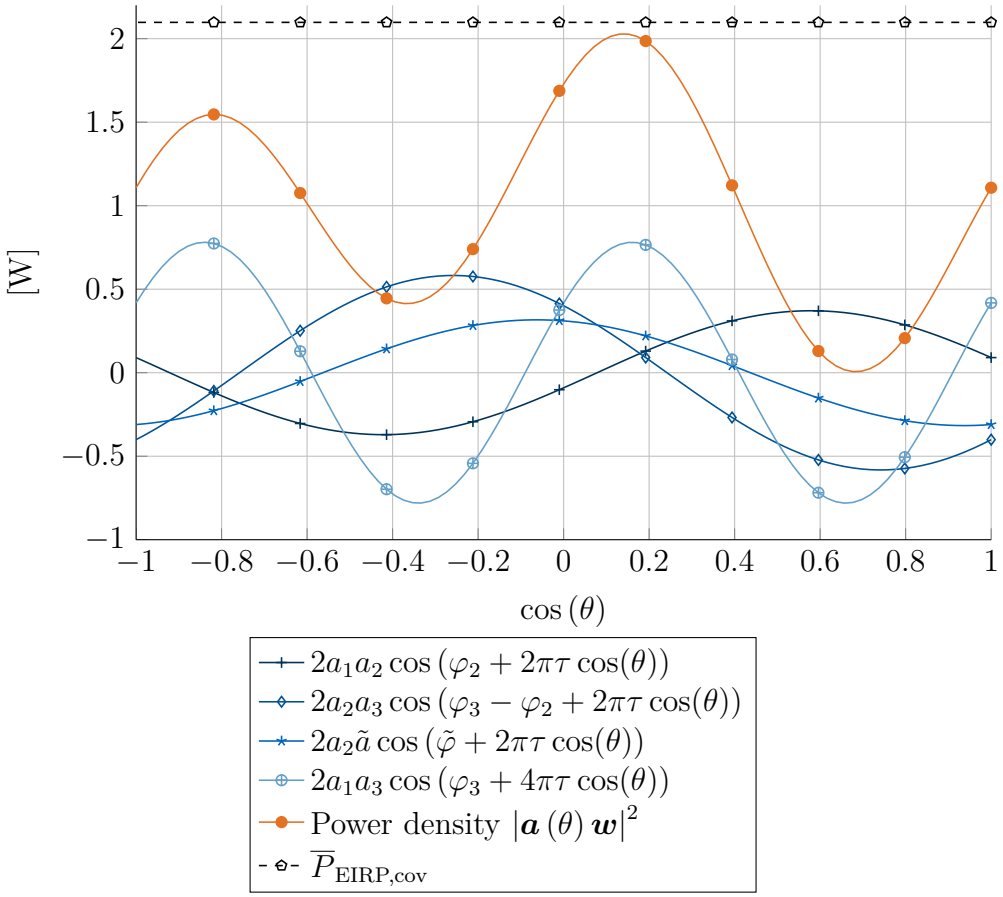

Figure 8.2.: Power density of an example precoder for $M = 3$ antennas.

functions add constructively. In this example the worst case upper bound is $\overline{P}_{\text{EIRP,worst}} = 3$. The fourth curve is the cosinusoidal function $2a_1a_3 \cos(\varphi_3 + 4\pi\tau\cos(\theta))$ which has twice the frequency as the two aforementioned cosinusoidal functions. One could interpret this function as the power density variation caused by interference of the transmissions from the first and third antenna. The sum of the three cosinusoidal functions and the transmit power is the power density. In this example a small gap exists between the maximum of the power density, i.e., the EIRP, and the proposed upper bound $\overline{P}_{\text{EIRP,cov}}$.

8.6. Comparison of EIRP Bounds

We compare the EIRP bounds for proper complex Gaussian i.i.d. precoder coefficients. We normalize the precoding matrix

$$\|\boldsymbol{W}\|_F^2 \leq 0\,\text{dBm} \tag{8.53}$$

such that the total transmit power is 0 dBm independent of the number K of streams and the number M of antennas. We average over 10^5 precoder realizations.

Figure 8.3 shows for a single stream ($K = 1$) the average EIRP and the average of the EIRP bounds. We obtain the EIRP with high accuracy from $N_{\mathrm{IDFT}} = 64M$ sample polar angles, i.e., we oversample the number M of antennas by a factor of 2^6. For our precoder choice the increase of EIRP P_{EIRP} becomes slower with an increasing number M of antennas. Next consider the EIRP lower bound $\underline{P}_{\mathrm{EIRP}}$ for $N_{\mathrm{IDFT}} = 2^4$, $N_{\mathrm{IDFT}} = 2^8$, and $N_{\mathrm{IDFT}} = 2^{12}$ sample polar angles θ. The lower bound is close to the EIRP up to critical sampling $N_{\mathrm{IDFT}} = M$. For undersampling the EIRP lower bound $\underline{P}_{\mathrm{EIRP}}$ does not increase with the number M of antennas and underestimates the EIRP. The lower bound $\underline{P}_{\mathrm{EIRP}}$ seems to be a better estimate than the upper bounds up to critical sampling. However, to ensure that EIRP constraints are fulfilled one must use upper bounds. We examine the error of the lower bound $\underline{P}_{\mathrm{EIRP}}$ in Figure 8.4. The EIRP upper bound $\overline{P}_{\mathrm{EIRP,[105]}}$ is feasible when oversampling at least twice. Hence for $N_{\mathrm{IDFT}} = 2^4$ it provides bounds until $M = 2^3$, for $N_{\mathrm{IDFT}} = 2^8$ until $M = 2^7$, and for $N_{\mathrm{IDFT}} = 2^{12}$ until $M = 2^{11}$, respectively. The gap to the EIRP is small for four times oversampling and very small for eight or more times oversampling. Hence it seems that at least $N_{\mathrm{IDFT}} = 4M$ samples are required to be able to estimate the EIRP accurately. The bound $\overline{P}_{\mathrm{EIRP,[104]}}$ for critical sampling is very loose for small numbers M of antennas. Here the worst case EIRP upper $\overline{P}_{\mathrm{EIRP,worst}}$, proposed in Section 8.4.1, is better. However, for more than $M > 2^8$ antennas $\overline{P}_{\mathrm{EIRP,[104]}}$ is better. Note that the worst case bound $\overline{P}_{\mathrm{EIRP,worst}}$ increases linearly with M while the EIRP increases more slowly. The EIRP upper bound based on the covariance matrix $\overline{P}_{\mathrm{EIRP,cov}}$, proposed in Section 8.4.2, does not require sampling at polar angles and achieves a smaller gap than the worst case EIRP upper $\overline{P}_{\mathrm{EIRP,worst}}$ and than the bound for critical sampling $\overline{P}_{\mathrm{EIRP,[104]}}$. However, the bound becomes loose as the number M of antennas increases.

Figure 8.4 shows the average and the maximum error of the EIRP lower bound $\underline{P}_{\mathrm{EIRP}}$ for $N_{\mathrm{IDFT}} = 2^4$, $N_{\mathrm{IDFT}} = 2^8$, and $N_{\mathrm{IDFT}} = 2^{12}$ sample polar angles θ observed for 10^5 precoder realizations. We already saw in Figure 8.3 that the average error increases slowly as the oversampling becomes smaller. The minimal error is as low as zero. However, the maximum error observed for 10^5 precoder realizations is larger and increases rapidly around critical sampling. Note that for more precoder realizations the maximum error might be even larger. These observations verify the significance of EIRP upper bounds and show that the EIRP lower bound $\underline{P}_{\mathrm{EIRP}}$ cannot show the compliance with EIRP constraints.

Figure 8.5 shows the EIRP P_{EIRP}, the lower bound $\underline{P}_{\mathrm{EIRP}}$ and the proposed upper bounds $\overline{P}_{\mathrm{EIRP,worst}}$, and $\overline{P}_{\mathrm{EIRP,cov}}$ for $K = 1$ stream, $K = 2$ streams, and $K = 8$ streams. The EIRP decreases with the number K of streams for a constant total transmit power. The EIRP bounds decrease similarly.

In conclusion, the EIRP upper bounds based on sampling require at least a four times oversampling to provide accurate bounds. The EIRP lower bound with at least critical sampling is on average a good estimator, but cannot show compliance with EIRP constraints. The EIRP upper bound $\overline{P}_{\mathrm{EIRP,cov}}$, proposed in Section 8.4.2, offers an interesting alternative which is not based on sampling at polar angles. With an increasing number of streams and constant total transmit power the EIRP usually decreases while the gaps of the EIRP bounds remain similar.

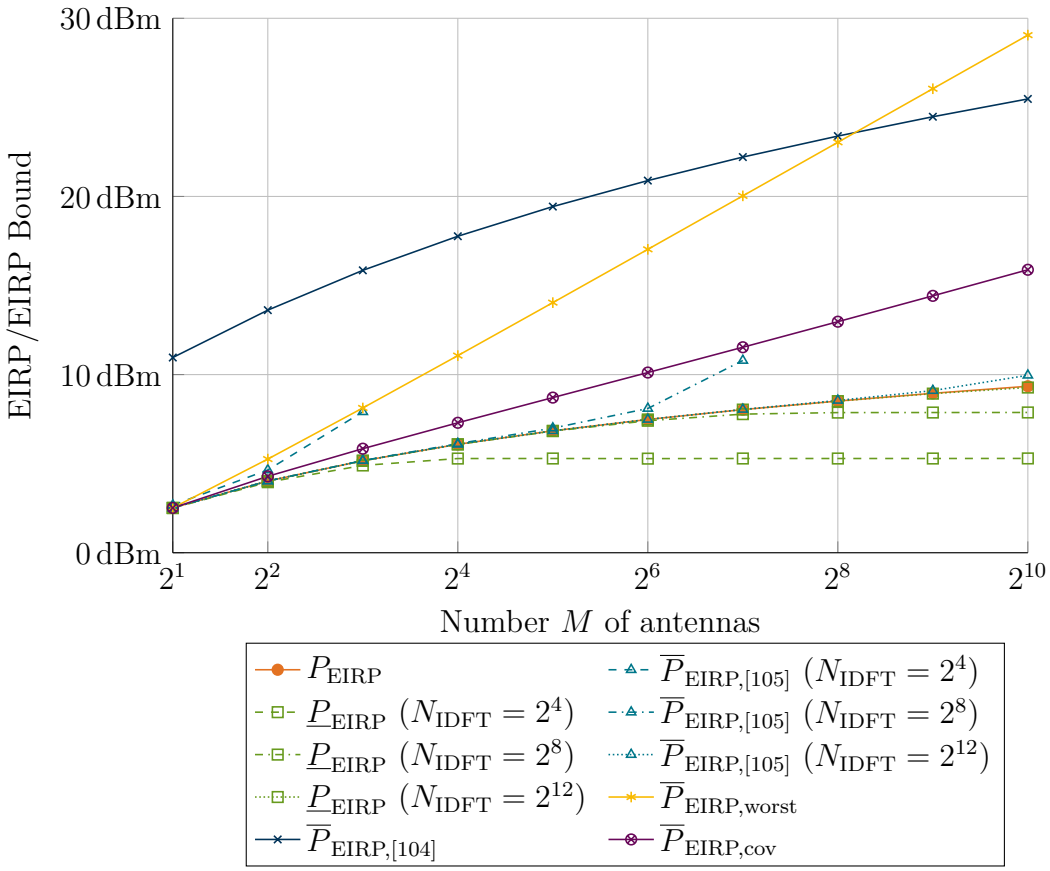

Figure 8.3.: EIRP and EIRP bounds for a single stream with proper complex Gaussian i.i.d. precoder coefficients and normalized total transmit power.

8.7. EIRP Aware Transmission Schemes

We conclude this chapter by a review of EIRP aware transmission schemes. We review linear precoding schemes only. Some of the described strategies also work for other antenna arrays.

8.7.1. Antenna Selection

A simple method to control the EIRP is to select a single antenna to transmit each stream. Usually one selects the antennas which achieve the largest received signal-to-noise ratio (SNR). To fulfill the EIRP constraint one can transmit at each antenna with a transmit power equal to the difference of the EIRP limit minus the antenna gain of the single antenna. This scheme is suboptimal in general, but it achieves capacity when transmitting to a single UE in the following scenarios [91]:

- ▷ Antenna selection combined with power allocation is optimal when two transmit antennas are deployed under an EIRP constraint.

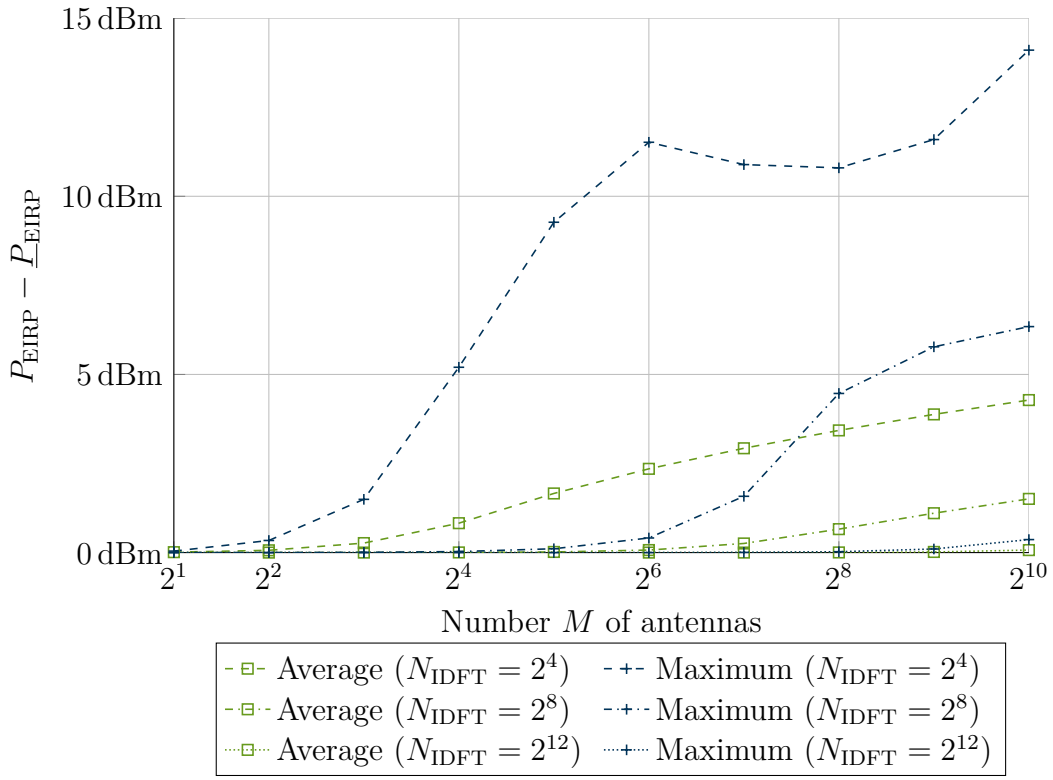

Figure 8.4.: Error of the EIRP lower bound $\underline{P}_{\mathrm{EIRP}}$ for a single stream with proper complex Gaussian i.i.d. precoder coefficients and normalized total transmit power.

- ▷ At low SNR, antenna selection is optimal for any number of transmit antennas under an EIRP constraint.
- ▷ If there are fewer BS antennas than UE antennas, transmitting one stream per BS antenna is optimal at high SNR.
- ▷ For a single antenna UE, antenna selection is always optimal under an EIRP constraint.

However, these scenarios are not massive MIMO scenarios.

8.7.2. Power Control

Another simple option is to scale the power of a transmission scheme which is unaware of the EIRP constraint. Let $\boldsymbol{W}$ be the precoding matrix obtained by applying an EIRP unaware transmission scheme. The precoding matrix which fulfills the EIRP constraint is then found as

$$\boldsymbol{W}^{\mathrm{scaled}} = \boldsymbol{W}\sqrt{\frac{P_{\mathrm{EIRP,max}}}{P_{\mathrm{EIRP}}}} \tag{8.54}$$

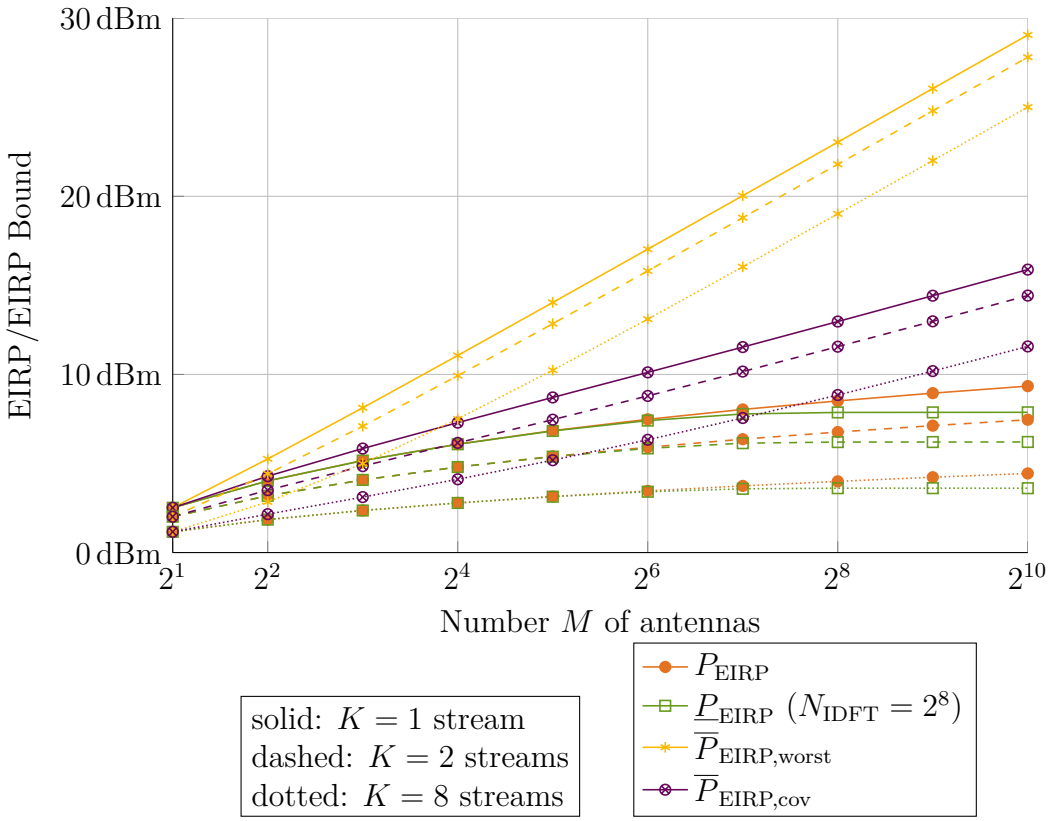

Figure 8.5.: EIRP and EIRP bounds for different numbers K of streams with proper complex Gaussian i.i.d. precoder coefficients and normalized total transmit power.

where $P_{\mathrm{EIRP,max}}$ is the EIRP limit and P_{EIRP} is the EIRP of the precoding matrix $\boldsymbol{W}$. Example transmission schemes are maximum ratio transmission (MRT) and ZFBF given a per-BS power constraint as presented in Section 2.4. More advanced ways of power control to comply with EIRP constraints are possible, for example, one could scale the power of some streams only. We learned in Chapter 7 that transmitting many low power streams usually causes less EIRP than transmitting few high power streams.

8.7.3. Optimal Precoding

The optimal precoder is known for a ULA when transmitting a single stream under an EIRP constraint [86]. It is the solution to the following optimization problem:

$$\begin{aligned} \hat{\boldsymbol{w}}_1 = \; & \arg\max_{\boldsymbol{w}_1} \left| \boldsymbol{h}^{\mathsf{H}} \boldsymbol{w}_1 \right|^2 \\ \text{s.t.} \quad & \lim_{N_{\mathrm{IDFT}} \to \infty} \left\| \boldsymbol{F}_{N_{\mathrm{IDFT}} \times M} \boldsymbol{w}_1 \right\|_\infty^2 \leq P_{\mathrm{EIRP,max}}. \end{aligned} \tag{8.55}$$

For a single transmit stream the EIRP constraint is fulfilled with equality at the optimum [90]. Note that, instead of constraining the peak power density, we can constrain the power density at N_{IDFT} angles where $N_{\mathrm{IDFT}} \to \infty$ approaches infinity

$$\begin{aligned} \hat{\boldsymbol{w}}_1 = \ & \arg\max_{\boldsymbol{w}_1} \left| \boldsymbol{h}^{\mathsf{H}} \boldsymbol{w}_1 \right|^2 \\ \text{s.t.} \quad & \left| \left[\boldsymbol{F}_{N_{\mathrm{IDFT}} \times M} \right]_{(n,:)} \boldsymbol{w}_1 \right|^2 \leq P_{\mathrm{EIRP,max}} \quad \forall n \in \{1, \ldots, N_{\mathrm{IDFT}}\} \,. \end{aligned} \tag{8.56}$$

The optimization problem (8.56) is non-deterministic polynomial-time (NP) hard since the objective is concave. However, it can be approximated as a second order cone problem (SOCP) [86]. Two observations lead to the SOCP formulation: Firstly note that any solution $\hat{\boldsymbol{w}}_1$ to the original problem can be multiplied with a phase shift $e^{j\nu}$ such that $e^{j\nu} \boldsymbol{h}^{\mathsf{H}} \hat{\boldsymbol{w}}_1$ becomes real and non-negative. The resulting vector $e^{j\nu} \hat{\boldsymbol{w}}_1$ is also a solution to the original problem. Hence one can fix w.l.o.g. the precoder $\hat{\boldsymbol{w}}_1$ such that $\boldsymbol{h}^{\mathsf{H}} \hat{\boldsymbol{w}}_1$ is real and non-negative. Secondly the constraints at infinitely many angles are replaced by equally spaced sample polar angles, hence instead of the real EIRP P_{EIRP} the EIRP lower bound $\underline{P}_{\mathrm{EIRP}}$ is considered. The optimization problem becomes

$$\begin{aligned} \hat{\boldsymbol{w}}_1 = \ & \arg\max_{\boldsymbol{w}_1} \boldsymbol{h}^{\mathsf{H}} \boldsymbol{w}_1 \\ \text{s.t.} \quad & \left| \left[\boldsymbol{F}_{N_{\mathrm{IDFT}} \times M} \right]_{(n,:)} \boldsymbol{w}_1 \right|^2 \leq P_{\mathrm{EIRP,max}} \quad \forall n \in \{1, \ldots, N_{\mathrm{IDFT}}\} \\ & \boldsymbol{h}^{\mathsf{H}} \boldsymbol{w}_1 \in \mathbb{R} \\ & \boldsymbol{h}^{\mathsf{H}} \boldsymbol{w}_1 \geq 0. \end{aligned} \tag{8.57}$$

As we saw in Section 8.6, oversampling of $\frac{N_{\mathrm{IDFT}}}{M} = 8$ or more times as many sample polar angles as the number M of ULA antennas allows the approximation that the EIRP lower bound equals the EIRP $\underline{P}_{\mathrm{EIRP}} \approx P_{\mathrm{EIRP}}$. However, to ensure that the EIRP constraint is fulfilled one should use an EIRP upper bound, as discussed in Section 8.3.

The SOCP can be solved, for example, with CVX [108], but, the algorithm has a high computational complexity [90]. The complexity increases when the optimal precoders are determined for multiple OFDM subcarriers jointly. Determining the optimal precoder for each precoder individually usually results in a performance loss [89]. Good performance is achieved with lower complexity when the optimization is carried out over groups of subcarriers with low correlation instead of over all subcarriers [89].

To the best of our knowledge, the optimal precoding strategy for the transmission of multiple streams given an EIRP constraint is not known.

8.7.4. Perturbation of Maximum-Ratio Transmission

Two transmission schemes targeted for UWB transmission of a single stream per subcarrier given an EIRP constraint are proposed in [90]. The transmission schemes improve performance as compared to antenna selection, and to MRT scaled to fulfill the EIRP constraint,

while they have a lower computational complexity than optimal precoding.[1] The schemes make use of the connection between the EIRP of a ULA and the PAPR of OFDM (see Section 8.2). Two schemes originally developed to reduce the PAPR of OFDM transmissions are applied to the MRT vector to reduce the EIRP. The schemes are enhanced to ensure that the direction of peak radiation is preserved. The first PAPR reduction scheme compresses the values of the MRT vector, while the second PAPR reduction scheme applies iterative soft clipping and filtering to the values of the MRT vector. Both approaches radiate more energy in directions other than the direction of peak radiation, which increases the received signal strength while keeping the peak power density unchanged. This way one approaches the optimal precoding under an EIRP constraint [90].

8.7.5. EIRP Constrained Codebooks

Another way to control EIRP is to use precoding vectors from a codebook with known EIRP. One approach based on Golay sequences is presented in [95]. Many works on codes with low PAPR targeted at OFDM systems exist, for example, see [104]. They might also help to control the EIRP.

8.7.6. Heuristic Optimization

One can use heuristic optimization methods to obtain suboptimal solutions for a wide range of antenna arrays and scenarios. The objective would be to maximize some performance metric while the EIRP constraint is not violated.

8.8. Summary

We analyzed the EIRP of a ULA and reviewed existing upper bounds for ULAs which apply to single stream transmissions only. We derived new upper bounds based on the transmission covariance matrix, which also apply to multiple stream transmissions. If the covariance matrix is already available the new bounds have low computational complexity, while the gap to the EIRP is small for low numbers of antennas. The IDFT allows to implement an sampling based EIRP lower bound efficiently. The EIRP upper bounds based on sampling require at least a eight times oversampling to provide accurate bounds. Increasing the number of streams while the total transmit power is constant reduces the EIRP. We reviewed EIRP aware transmission schemes. The optimal precoding is unknown for many scenarios and is often computationally complex when it is known.

[1] In [90] eigen-beamforming is considered instead of MRT. Eigen-beamforming is a generalization of MRT from a UE with a single antenna to a UE with multiple antennas. However, still a single stream is transmitted per subcarrier. In this case eigen-beamforming is optimal.

9

Conclusions

We discussed two aspects of massive MIMO which is a key strategy to achieve the goals of future mobile networks. We analyzed massive MIMO in an indoor scenario in Part I and the EIRP of MIMO arrays in Part II.

Conclusions to Part I

We presented precoding and power allocation schemes which allowed us to create transmissions with different levels of cooperation between BSs. We compared their performance in the 3rd Generation Partnership Project (3GPP) indoor office scenario. We fixed the number of active, single antenna UEs and swept the ratio of total number of BS antennas to the number of served UEs from one to 10-times more BS antennas. We found that a ratio of twice as many BS antennas as UEs provides most of the massive MIMO benefits. We further found that this ratio is a good tradeoff between the number of antennas versus spectral efficiency (SE). Channel hardening occurred for two- to four-times as many BS antennas as served UEs for indoor BSs. The performance differences between power allocations were small and scheduling did not provide gains. The suboptimal transmission schemes approached a capacity upper bound and achieved user fairness. Cooperation between BSs provided gains as compared to no cooperation, which became larger as the level of cooperation increased. Cooperation between indoor BSs provided large gains, while cooperation between outdoor BSs or indoor and outdoor BSs provided only small gains. The positions of BSs determined the wall penetration loss and the interference, which dominated performance. The same performance as a single massive MIMO BS is achieved by distributed BSs with cooperation and fewer antennas. The costs of antenna elements could be traded off with the costs for backhaul capability, while achieving the

same performance. Channel estimation had to be accurate to obtain the massive MIMO and cooperation benefits.

Future research topics include:

- ▷ Extend the analysis to a building with more floors. One must deal with interference between floors and more BS deployments are possible.
- ▷ Optimize the positions of the BSs.
- ▷ Extend the optimization problem to a cost minimization problem or a energy efficiency maximization problem, where costs or required energy are defined, for example, per antenna, per BS, or per backhaul link.
- ▷ Many interference coordination schemes exist besides LS-MIMO. Their performance could be evaluated in the indoor office scenario.
- ▷ Mixed or adaptive transmission schemes could achieve further improvements, for example, depending on their positions some UEs could be served with network MIMO, others with local precoding.
- ▷ One could include particular channel estimation techniques, for example, pilot based techniques to study the effects of pilot contamination, or channel channel prediction techniques.
- ▷ One could evaluate the performance experimentally in a real environment.
- ▷ In a real mobile network the number of UEs changes over time. One could include the variable UE load.

Conclusions to Part II

We defined the EIRP and learned that in most cases one can determine only EIRP bounds, since measuring or calculating the power density at infinitely many positions is infeasible. We reviewed EIRP constraints in regulations. We analyzed an EIRP lower bound of the precoders in the indoor scenario of Part I. The EIRP increased with an increasing number of BS antennas, but, it also decreased when few antennas were added to a fully loaded scenario. The power allocation had a large impact on the EIRP. Transmitting more streams at a constant total transmit power reduced the EIRP. Two- to four-times as many BS antennas as served UEs seems to be a good trade-off between EIRP and performance. The EIRP sometimes violates the typical regulations, and EIRP controlling measures are required. However, with additional degrees-of-freedom one can choose different precoders that might achieve a similar performance at a reduced EIRP. We concluded that massive MIMO achieves its advantages also given EIRP constraints. However, one should include EIRP constraints when analyzing massive MIMO and use EIRP aware transmission schemes. EIRP upper bounds help to design precoders that ensure that the EIRP

does not violate the constraints. We reviewed existing upper bounds for ULAs which apply to single stream transmissions. We derived new upper bounds, which apply also to multiple stream transmissions and which have low computational complexity if the covariance matrix is available. We found that, for ULAs, the EIRP upper bounds based on sampling require at least a four times oversampling to provide accurate bounds. We reviewed EIRP aware transmission schemes and found that the optimal precoding is either unknown or computationally complex for most scenarios.

For the EIRP many open problems exist.

- ▷ To the best of our knowledge, no EIRP upper bounds exist for rectangular arrays or other advanced arrays. In future research one might be able to use the two-dimensional IDFT to obtain EIRP bounds in a similar way as with the IDFT for the ULA.
- ▷ The existing EIRP upper bounds apply to single stream transmissions only and should be extended to multiple streams. Also, new upper and lower bounds could be discovered.
- ▷ The existing EIRP aware transmission schemes could be extended to multiple stream transmissions, and new schemes could be discovered. For example, one could use the proposed EIRP upper bound based on the covariance matrix as a constraint while maximizing a performance metric.
- ▷ One simple method to control EIRP could be EIRP aware power allocation and scheduling.
- ▷ To the best of our knowledge, the capacity given an EIRP constraint is not known for most scenarios.

A

Proofs for Part II

Lemma A.1. Let $\hat{\theta}$ be the angle which solves

$$\hat{\theta} = \arg \max_{\theta \in [0,\pi]} \sum_{k=1}^{K} \left| \boldsymbol{a}\left(\theta\right)^{\mathsf{T}} \boldsymbol{w}_k \right|^2 \tag{A.1}$$

where $\boldsymbol{w}_k \in \mathbb{C}^M$ and the array manifold vector is

$$\boldsymbol{a}\left(\theta\right) = \begin{bmatrix} 1 \\ e^{j2\pi\tau\cos(\theta)} \\ \vdots \\ e^{j2\pi(M-1)\tau\cos(\theta)} \end{bmatrix}. \tag{A.2}$$

The angle $\hat{\theta}$ that solves (A.1) is unique for $0 < \tau < \frac{1}{2}$, one or two angles $\hat{\theta}$ exist for $\frac{1}{2} \leq \tau < 1$, and multiple angles $\hat{\theta}$ exist for $\tau \geq 1$.

Proof. The angle $\hat{\theta}$ is not unique if there is an angle $\tilde{\theta} \neq \hat{\theta}$ for which

$$\boldsymbol{a}\left(\tilde{\theta}\right) = \boldsymbol{a}\left(\hat{\theta}\right). \tag{A.3}$$

This is the case if all elements of the vectors are equal, i.e., $\forall m \in \{1, \ldots, M\}$ we have

$$\begin{aligned} \left[\boldsymbol{a}\left(\tilde{\theta}\right)\right]_{(m)} &= \left[\boldsymbol{a}\left(\hat{\theta}\right)\right]_{(m)} \\ = e^{j2\pi(m-1)\tau\cos\left(\tilde{\theta}\right)} &= e^{j2\pi(m-1)\tau\cos\left(\hat{\theta}\right)} \end{aligned} \tag{A.4}$$

$$\Leftrightarrow 2\pi\,(m-1)\,\tau\cos\left(\tilde{\theta}\right) \mod 2\pi = 2\pi\,(m-1)\,\tau\cos\left(\hat{\theta}\right) \mod 2\pi \tag{A.5}$$

$$\Leftrightarrow (m-1)\,\tau\cos\left(\tilde{\theta}\right) \mod 1 = (m-1)\,\tau\cos\left(\hat{\theta}\right) \mod 1 \tag{A.6}$$

$$\Leftrightarrow \tau\cos\left(\tilde{\theta}\right) \mod 1 = \tau\cos\left(\hat{\theta}\right) \mod 1. \tag{A.7}$$

Note that in (A.7) the antenna index m vanished, since it is an integer. Hence we have to consider only one equation instead of M equations.

W.l.o.g. let $-\frac{1}{2} \leq \tau\cos\left(\hat{\theta}\right) < \frac{1}{2}$ and choose $n \in \mathbb{Z}$ such that $-\frac{1}{2} \leq \tau\cos\left(\tilde{\theta}\right) - n < \frac{1}{2}$. Now we restate (A.7) as

$$\tau\cos\left(\tilde{\theta}\right) = \tau\cos\left(\hat{\theta}\right) + n \tag{A.8}$$

$$\Leftrightarrow \cos\left(\tilde{\theta}\right) = \cos\left(\hat{\theta}\right) + \frac{n}{\tau}. \tag{A.9}$$

For $n = 0$ it follows that $\hat{\theta} = \tilde{\theta}$. For $n \neq 0$ we obtain

$$\tilde{\theta} = \arccos\left(\cos\left(\hat{\theta}\right) + \frac{n}{\tau}\right). \tag{A.10}$$

The inverse cosine function is defined as [83, p. 126]

$$\tilde{\theta} = \arccos(x) \Leftrightarrow x = \cos\left(\hat{\theta}\right) \tag{A.11}$$

where $0 \leq \tilde{\theta} \leq \pi$ and $-1 \leq x \leq 1$.

Hence multiple solutions to (A.10) and multiple angles exist if there is at least one n, $n \neq 0$, which fulfills

$$-1 \leq \cos\left(\hat{\theta}\right) + \frac{n}{\tau} \leq 1. \tag{A.12}$$

For $\tau < \frac{1}{2}$ it follows that $\frac{n}{\tau} > 2$ except for $n = 0$. Hence only $n = 0$ is feasible and a unique angle $\tilde{\theta}$ exists. For $\tau \geq 1$ it follows that there is a nontrivial $n \neq 0$ such that $\left|\frac{n}{\tau}\right| \leq 1$. Hence at least one $n \neq 0$ is feasible and multiple solutions to (A.1) exist. For $\frac{1}{2} \leq \tau < 1$ the number of feasible n depends on $\cos\left(\hat{\theta}\right)$ and τ. The angle $\tilde{\theta}$ can be unique or multiple angles can exist. ■

Lemma A.2 (Harmonic Addition Theorem [109, slightly modified])**.** Let $a, b, \alpha, \beta, \kappa, t \in \mathbb{R}$. The sum of two cosinusoidal functions with frequency κ can be expressed as one cosinusoidal function:

$$a\cos(\alpha + \kappa t) + b\cos(\beta + \kappa t) = c\cos(\gamma + \kappa t) \tag{A.13}$$

where

$$c = \sqrt{a^2 + b^2 + 2ab\cos(\alpha - \beta)} \tag{A.14}$$

$$\gamma = \cos^{-1}\left(\frac{a\cos(\alpha) + b\cos(\beta)}{\sqrt{a^2 + b^2 + 2ab\cos(\alpha - \beta)}}\right). \tag{A.15}$$

Proof. Expand the left hand side of (A.13) as

$$\begin{aligned} & a\cos(\alpha + \kappa t) + b\cos(\beta + \kappa t) \\ = \; & (a\cos(\alpha) + b\cos(\beta))\cos(\kappa t) - (a\sin(\alpha) + b\sin(\beta))\sin(\kappa t) \end{aligned} \tag{A.16}$$

and the right hand side of (A.13) as

$$c\cos(\gamma + \kappa t) = c\cos(\gamma)\cos(\kappa t) - c\sin(\gamma)\sin(\kappa t). \tag{A.17}$$

Comparing (A.16) and (A.17), the following two equations must hold:

$$a\cos(\alpha) + b\cos(\beta) = c\cos(\gamma) \tag{A.18}$$

$$a\sin(\alpha) + b\sin(\beta) = c\sin(\gamma). \tag{A.19}$$

We solve for c by adding the square of (A.18) to the square of (A.19):

$$(a\cos(\alpha) + b\cos(\beta))^2 + (a\sin(\alpha) + b\sin(\beta))^2 = c^2 \tag{A.20}$$

$$\Leftrightarrow \sqrt{a^2 + b^2 + 2ab\cos(\alpha - \beta)} = c. \tag{A.21}$$

Once we find c, we solve for γ in (A.18) as

$$\cos^{-1}\left(\frac{a\cos(\alpha) + b\cos(\beta)}{\sqrt{a^2 + b^2 + 2ab\cos(\alpha - \beta)}}\right) = \gamma. \tag{A.22}$$

■

B

Abbreviations

List of Abbreviations

3GPP	3rd Generation Partnership Project
5G	5th generation mobile networks
AWGN	additive white Gaussian noise
BC	broadcast channel
BS	base station
CB	coordinated beamforming
CDF	cumulative distribution function
CoMP	coordinated multipoint
CS	coordinated scheduling
CS/CB	coordinated scheduling/coordinated beamforming
CSI	channel state information
DPC	dirty paper coding
ECC	Electronic Communications Committee
EIRP	equivalent isotropically radiated power
ERP	effective radiated power
FCC	Federal Communications Commission
FDD	frequency division duplex
i.i.d.	independent and identically distributed

IA	interference alignment
IDFT	inverse discrete Fourier transform
IFFT	inverse fast Fourier transform
ISI	inter symbol interference
ITU	International Telecommunication Union
LOS	line-of-sight
LS-MIMO	large-scale MIMO
LTE	Long Term Evolution
LTE-Advanced	Long Term Evolution-Advanced
MAC	multiple-access channel
METIS	Mobile and wireless communications Enablers for the Twenty-twenty Information Society
MIMO	multiple-input multiple-output
MISO	multiple-input single-output
MMSE	minimum mean squared error
MRT	maximum ratio transmission
NLOS	non line-of-sight
NP	non-deterministic polynomial-time
OFDM	orthogonal frequency-division multiplexing
P-ZF	full-pilot zero-forcing
PAPR	peak-to-average power ratio
PRB	physical resource block
QAM	quadrature amplitude modulation
QoS	quality-of-service
QuaDRiGa	Quasi Deterministic Radio Channel Generator
SAR	specific absorption rate
SE	spectral efficiency
SINR	signal-to-interference-plus-noise ratio
SISO	single-input single-output
SNR	signal-to-noise ratio
SOCP	second order cone problem
SVD	singular value decomposition
TDD	time division duplex
UE	user equipment
ULA	uniform linear array
UWB	ultra wide band

w.l.o.g.	without loss of generality
WINNER	Wireless World Initiative New Radio
WINNER II	Wireless World Initiative New Radio II
WINNER+	Wireless World Initiative New Radio+
WLAN	wireless local area network
ZFBF	zero-forcing beamforming

Bibliography

[1] A. Osseiran, F. Boccardi, V. Braun, K. Kusume, P. Marsch, M. Maternia, O. Queseth, M. Schellmann, H. Schotten, H. Taoka, H. Tullberg, M. A. Uusitalo, B. Timus, and M. Fallgren, "Scenarios for 5G mobile and wireless communications: The vision of the METIS project," *IEEE Commun. Mag.*, vol. 52, no. 5, pp. 26–35, May 2014.

[2] Mobile and Wireless Communications Enablers for the Twenty-Twenty Information Society (METIS), "Deliverable D1.1 - scenarios, requirements and KPIs for 5G mobile and wireless system," Tech. Rep., Apr. 2013.

[3] J. G. Andrews, S. Buzzi, W. Choi, S. V. Hanly, A. Lozano, A. C. K. Soong, and J. C. Zhang, "What will 5G be?" *IEEE J. Sel. Areas Commun.*, vol. 32, no. 6, pp. 1065–1082, Jun. 2014.

[4] T. Marzetta, "Noncooperative cellular wireless with unlimited numbers of base station antennas," *IEEE Trans. Wireless Commun.*, vol. 9, no. 11, pp. 3590–3600, Nov. 2010.

[5] E. Larsson, O. Edfors, F. Tufvesson, and T. Marzetta, "Massive MIMO for next generation wireless systems," *IEEE Commun. Mag.*, vol. 52, no. 2, pp. 186–195, Feb. 2014.

[6] E. Björnson, E. G. Larsson, and T. L. Marzetta, "Massive MIMO: Ten myths and one critical question," *IEEE Commun. Mag.*, vol. 54, no. 2, pp. 114–123, Feb. 2016.

[7] J. Zhang and G. de la Roche, Eds., *Femtocells: Technologies and Deployment.* John Wiley & Sons, 2013.

[8] 3GPP, "TR36.814 - further advancements for E-UTRA physical layer aspects," Tech. Rep. v9.0.0, Mar. 2010.

[9] A. Goldsmith, *Wireless Communications.* Cambridge University Press, 2005.

[10] L. Lu, G. Y. Li, A. L. Swindlehurst, A. Ashikhmin, and R. Zhang, "An overview of massive MIMO: Benefits and challenges," *IEEE J. Sel. Topics Signal Process.*, vol. 8, no. 5, pp. 742–758, Oct. 2014.

[11] E. Björnson, M. Bengtsson, and B. Ottersten, "Optimal multiuser transmit beamforming: A difficult problem with a simple solution structure [lecture notes]," *IEEE Signal Process. Mag.*, vol. 31, no. 4, pp. 142–148, Jul. 2014.

[12] E. Björnson and E. Jorswieck, "Optimal resource allocation in coordinated multi-cell systems," *Foundations and Trends in Communications and Information Theory*, vol. 9, no. 2-3, pp. 113–381, 2013. [Online]. Available: http://dx.doi.org/10.1561/0100000069

[13] Y. F. Liu, Y. H. Dai, and Z. Q. Luo, "Coordinated beamforming for MISO interference channel: Complexity analysis and efficient algorithms," *IEEE Trans. Signal Process*, vol. 59, no. 3, pp. 1142–1157, Mar. 2011.

[14] T. K. Y. Lo, "Maximum ratio transmission," *IEEE Trans. Commun.*, vol. 47, no. 10, pp. 1458–1461, Oct. 1999.

[15] F. Rusek, D. Persson, B. K. Lau, E. G. Larsson, T. L. Marzetta, O. Edfors, and F. Tufvesson, "Scaling up MIMO: Opportunities and challenges with very large arrays," *IEEE Signal Process. Mag.*, vol. 30, no. 1, pp. 40–60, Jan. 2013.

[16] A. Wiesel, Y. Eldar, and S. Shamai, "Zero-forcing precoding and generalized inverses," *IEEE Trans. Signal Proc.*, vol. 56, no. 9, pp. 4409–4418, Sep. 2008.

[17] C. E. Shannon, "A mathematical theory of communication," *The Bell System Technical Journal*, vol. 27, no. 3, pp. 379–423, Jul. 1948.

[18] G. Böcherer, F. Steiner, and P. Schulte, "Bandwidth efficient and rate-matched low-density parity-check coded modulation," *IEEE Trans. Commun.*, vol. 63, no. 12, pp. 4651–4665, Dec. 2015.

[19] G. Ungerboeck, "Channel coding with multilevel/phase signals," *IEEE Trans. Inf. Theory*, vol. 28, no. 1, pp. 55–67, Jan. 1982.

[20] A. Lozano, A. M. Tulino, and S. Verdu, "Mercury/waterfilling: Optimum power allocation with arbitrary input constellations," in *Int. Symp. Information Theory (ISIT)*, Sep. 2005, pp. 1773–1777.

[21] ——, "Optimum power allocation for parallel Gaussian channels with arbitrary input distributions," *IEEE Trans. Inf. Theory*, vol. 52, no. 7, pp. 3033–3051, Jul. 2006.

[22] T. M. Cover and J. A. Thomas, Eds., *Elements of Information Theory*. John Wiley & Sons, 2006.

[23] D. Guo, S. Shamai, and S. Verdu, "Mutual information and minimum mean-square error in Gaussian channels," *IEEE Trans. Inf. Theory*, vol. 51, no. 4, pp. 1261–1282, Apr. 2005.

[24] A. Lozano, A. M. Tulino, and S. Verdu, "Mercury/waterfilling for fixed wireless OFDM systems," in *IEEE Radio and Wireless Symp. (RWW)*, Jan. 2006, pp. 211–214.

[25] ——, "Multiuser mercury/waterfilling for downlink OFDM with arbitrary signal constellations," in *IEEE 9th Int. Symp. Spread Spectrum Techniques and Applications (ISSSTA)*, Aug. 2006, pp. 292–296.

[26] ——, "Optimum power allocation for multiuser OFDM with arbitrary signal constellations," *IEEE Trans. Commun.*, vol. 56, no. 5, pp. 828–837, May 2008.

[27] D. Kivanc, G. Li, and H. Liu, "Computationally efficient bandwidth allocation and power control for OFDMA," *IEEE Trans. Wireless Commun.*, vol. 2, no. 6, pp. 1150–1158, Nov. 2003.

[28] T. Yoo and A. Goldsmith, "Capacity and power allocation for fading MIMO channels with channel estimation error," *IEEE Trans. Inf. Theory*, vol. 52, no. 5, pp. 2203–2214, May 2006.

[29] G. Caire and S. Shamai, "On the achievable throughput of a multiantenna Gaussian broadcast channel," *IEEE Trans. Inf. Theory*, vol. 49, no. 7, pp. 1691–1706, Jul. 2003.

[30] P. Viswanath and D. N. C. Tse, "Sum capacity of the vector Gaussian broadcast channel and uplink-downlink duality," *IEEE Trans. Inf. Theory*, vol. 49, no. 8, pp. 1912–1921, Aug. 2003.

[31] S. Vishwanath, N. Jindal, and A. Goldsmith, "Duality, achievable rates, and sum-rate capacity of Gaussian MIMO broadcast channels," *IEEE Trans. Inf. Theory*, vol. 49, no. 10, pp. 2658–2668, Oct. 2003.

[32] W. Yu and J. M. Cioffi, "Sum capacity of Gaussian vector broadcast channels," *IEEE Trans. Inf. Theory*, vol. 50, no. 9, pp. 1875–1892, Sep. 2004.

[33] M. Costa, "Writing on dirty paper," *IEEE Trans. Inf. Theory*, vol. 29, no. 3, pp. 439–441, May 1983.

[34] N. Jindal, W. Rhee, S. Vishwanath, S. Jafar, and A. Goldsmith, "Sum power iterative water-filling for multi-antenna Gaussian broadcast channels," *IEEE Trans. Inf. Theory*, vol. 51, no. 4, pp. 1570–1580, Apr. 2005.

[35] W. Yu, W. Rhee, S. Boyd, and J. M. Cioffi, "Iterative water-filling for Gaussian vector multiple-access channels," *IEEE Trans. Inf. Theory*, vol. 50, no. 1, pp. 145–152, Jan. 2004.

[36] M. Kobayashi and G. Caire, "An iterative water-filling algorithm for maximum weighted sum-rate of Gaussian MIMO-BC," *IEEE J. Sel. Areas Commun.*, vol. 24, no. 8, pp. 1640–1646, Aug. 2006.

[37] ——, "Iterative waterfilling for weighted rate sum maximization in MIMO-OFDM broadcast channels," in *IEEE Int. Conf. on Acoustics, Speech and Signal Processing (ICASSP)*, vol. 3, Apr. 2007, pp. III–5–III–8.

[38] A. F. Molisch, M. Z. Win, and J. H. Winters, "Space-time-frequency (STF) coding for MIMO-OFDM systems," *IEEE Commun. Lett.*, vol. 6, no. 9, pp. 370–372, Sep. 2002.

[39] T. Bonald, "A score-based opportunistic scheduler for fading radio channels," in *European Wireless (EW)*, 2004.

[40] X. Zhang and J. Lee, "Low complexity MIMO scheduling with channel decomposition using capacity upperbound," *IEEE Trans. Commun.*, vol. 56, no. 6, pp. 871–876, Jun. 2008.

[41] H. Sato, "An outer bound to the capacity region of broadcast channels," *IEEE Trans. Inf. Theory*, vol. 24, no. 3, pp. 374–377, May 1978.

[42] I. E. Telatar, "Capacity of multi-antenna Gaussian channels," *European Transactions on Telecommunications*, vol. 10, pp. 585–595, 1999.

[43] Z. Shen, R. Chen, J. G. Andrews, R. W. Heath, and B. L. Evans, "Low complexity user selection algorithms for multiuser MIMO systems with block diagonalization," *IEEE Trans. Signal Process.*, vol. 54, no. 9, pp. 3658–3663, Sep. 2006.

[44] K. Ko and J. Lee, "Multiuser MIMO user selection based on chordal distance," *IEEE Trans. Commun.*, vol. 60, no. 3, pp. 649–654, Mar. 2012.

[45] J. Wang, D. J. Love, and M. D. Zoltowski, "User selection for the MIMO broadcast channel with a fairness constraint," in *IEEE Int. Conf. Acoustics, Speech and Signal Processing (ICASSP)*, vol. 3, Apr. 2007, pp. III–9–III–12.

[46] G. Gupta and A. K. Chaturvedi, "Conditional entropy based user selection for multiuser MIMO systems," *IEEE Commun. Lett.*, vol. 17, no. 8, pp. 1628–1631, Aug. 2013.

[47] F. Boccardi, R. W. Heath, A. Lozano, T. L. Marzetta, and P. Popovski, "Five disruptive technology directions for 5G," *IEEE Commun. Mag.*, vol. 52, no. 2, pp. 74–80, Feb. 2014.

[48] E. Björnson, L. Sanguinetti, J. Hoydis, and M. Debbah, "Optimal design of energy-efficient multi-user MIMO systems: Is massive MIMO the answer?" *IEEE Trans. Wireless Commun.*, vol. 14, no. 6, pp. 3059–3075, Jun. 2015.

[49] J. Hoydis, S. ten Brink, and M. Debbah, "Massive MIMO in the UL/DL of cellular networks: How many antennas do we need?" *IEEE J. Sel. Areas Commun.*, vol. 31, no. 2, pp. 160–171, Feb. 2013.

[50] J. Choi, D. J. Love, and P. Bidigare, "Downlink training techniques for FDD massive MIMO systems: Open-loop and closed-loop training with memory," *IEEE J. Sel. Topics Signal Process.*, vol. 8, no. 5, pp. 802–814, Oct. 2014.

[51] X. Gao, O. Edfors, F. Rusek, and F. Tufvesson, "Massive MIMO performance evaluation based on measured propagation data," *IEEE Trans. Wireless Commun.*, vol. 14, no. 7, pp. 3899–3911, Jul. 2015.

[52] S. Dierks and N. Jünger, "Energy efficiency of massive MIMO and network MIMO in an indoor scenario," in *21th Int. ITG Workshop Smart Antennas (WSA)*, Mar. 2017, pp. 1–5.

[53] G. J. Foschini, K. Karakayali, and R. A. Valenzuela, "Coordinating multiple antenna cellular networks to achieve enormous spectral efficiency," *IEE Proc. - Communications*, vol. 153, no. 4, pp. 548–555, Aug. 2006.

[54] G. Boudreau, J. Panicker, N. Guo, R. Chang, N. Wang, and S. Vrzic, "Interference coordination and cancellation for 4G networks," *IEEE Commun. Mag.*, vol. 47, no. 4, pp. 74–81, Apr. 2009.

[55] D. Lee, H. Seo, B. Clerckx, E. Hardouin, D. Mazzarese, S. Nagata, and K. Sayana, "Coordinated multipoint transmission and reception in LTE-advanced: Deployment scenarios and operational challenges," *IEEE Commun. Mag.*, vol. 50, no. 2, pp. 148–155, Feb. 2012.

[56] D. Gesbert, S. Hanly, H. Huang, S. S. Shitz, O. Simeone, and W. Yu, "Multi-cell MIMO cooperative networks: A new look at interference," *IEEE J. Sel. Areas Commun.*, vol. 28, no. 9, pp. 1380–1408, Dec. 2010.

[57] M. Schubert and H. Boche, "QoS-based resource allocation and transceiver optimization," *Foundations and Trends in Communications and Information Theory*, vol. 2, no. 6, pp. 383–529, 2006. [Online]. Available: http://dx.doi.org/10.1561/0100000010

[58] A. S. Hamza, S. S. Khalifa, H. S. Hamza, and K. Elsayed, "A survey on inter-cell interference coordination techniques in OFDMA-based cellular networks," *IEEE Communications Surveys Tutorials*, vol. 15, no. 4, pp. 1642–1670, Apr. 2013.

[59] H. Dahrouj and W. Yu, "Coordinated beamforming for the multicell multi-antenna wireless system," *IEEE Trans. Wireless Commun.*, vol. 9, no. 5, pp. 1748–1759, May 2010.

[60] S. A. Jafar, "Interference alignment — a new look at signal dimensions in a communication network," *Foundations and Trends in Communications and Information Theory*, vol. 7, no. 1, pp. 1–134, 2011. [Online]. Available: http://dx.doi.org/10.1561/0100000047

[61] S. Dierks, G. Kramer, and W. Zirwas, "Feasibility conditions of interference alignment via two orthogonal subcarriers," in *Int. Symp. Information Theory (ISIT)*, Jul. 2013, pp. 579–583.

[62] K. Hosseini, W. Yu, and R. S. Adve, "Large-scale MIMO versus network MIMO for multicell interference mitigation," *IEEE J. Sel. Topics Signal Process.*, vol. 8, no. 5, pp. 930–941, Oct. 2014.

[63] E. Björnson, E. G. Larsson, and M. Debbah, "Massive MIMO for maximal spectral efficiency: How many users and pilots should be allocated?" *IEEE Trans. Wireless Commun.*, vol. 15, no. 2, pp. 1293–1308, Feb. 2016.

[64] R. Zhang, "Cooperative multi-cell block diagonalization with per-base-station power constraints," *IEEE J. Sel. Areas Commun.*, vol. 28, no. 9, pp. 1435–1445, Dec. 2010.

[65] S. Shi, M. Schubert, N. Vucic, and H. Boche, "MMSE optimization with per-base-station power constraints for network MIMO systems," in *IEEE Int. Conf. Communications (ICC)*, May 2008, pp. 4106–4110.

[66] S. Kaviani and W. A. Krzymień, "Optimal multiuser zero forcing with per-antenna power constraints for network MIMO coordination," *EURASIP Journal on Wireless Communications and Networking*, vol. 2011, no. 1, pp. 1–12, 2011.

[67] H. Zhang and H. Dai, "On the capacity of distributed MIMO systems," in *38th Conf. Inform. Sciences and Systems (CISS)*, 2004.

[68] A. Forenza, S. Perlman, F. Saibi, M. D. Dio, R. van der Laan, and G. Caire, "Achieving large multiplexing gain in distributed antenna systems via cooperation with pCell technology," in *49th Asilomar Conf. Signals, Systems and Computers (ACSSC)*, Nov. 2015, pp. 286–293.

[69] V. Jungnickel, K. Manolakis, W. Zirwas, B. Panzner, V. Braun, M. Lossow, M. Sternad, R. Apelfrojd, and T. Svensson, "The role of small cells, coordinated multipoint, and massive MIMO in 5G," *IEEE Commun. Mag.*, vol. 52, no. 5, pp. 44–51, May 2014.

[70] H. Huh, A. M. Tulino, and G. Caire, "Network MIMO with linear zero-forcing beamforming: Large system analysis, impact of channel estimation, and reduced-complexity scheduling," *IEEE Trans. Inf. Theory*, vol. 58, no. 5, pp. 2911–2934, May 2012.

[71] H. Huh, G. Caire, H. C. Papadopoulos, and S. A. Ramprashad, "Achieving "massive MIMO" spectral efficiency with a not-so-large number of antennas," *IEEE Trans. Wireless Commun.*, vol. 11, no. 9, pp. 3226–3239, Sep. 2012.

[72] S. Jaeckel, L. Raschkowski, K. Börner, L. Thiele, F. Burkhardt, and E. Eberlein, "QuaDRiGa-quasi determinsitic radio channel generator, user manual and documentation," Fraunhofer Heinrich Hertz Institute, Tech. Rep. v1.4.1-551, 2016.

[73] S. Jaeckel, L. Raschkowski, K. Börner, and L. Thiele, "QuaDRiGa: A 3-D multi-cell channel model with time evolution for enabling virtual field trials," *IEEE Trans. Antennas Propag.*, vol. 62, no. 6, pp. 3242–3256, Jun. 2014.

[74] IST, "D1.1.2 - WINNER II channel models," Tech. Rep. v1.2, 2008.

[75] G. De la Roche, A. Alayón-Glazunov, and B. Allen, *LTE-Advanced and Next Generation Wireless Networks: Channel Modelling and Propagation*. John Wiley & Sons, 2012.

[76] CELTIC, "D5.3: WINNER+ final channel models," Tech. Rep. v1.0, 2010.

[77] C. X. Wang, F. Haider, X. Gao, X. H. You, Y. Yang, D. Yuan, H. M. Aggoune, H. Haas, S. Fletcher, and E. Hepsaydir, "Cellular architecture and key technologies for 5G wireless communication networks," *IEEE Commun. Mag.*, vol. 52, no. 2, pp. 122–130, Feb. 2014.

[78] S. Dierks, M. Amin, W. Zirwas, M. Haardt, and B. Panzner, "The benefit of cooperation in the context of massive MIMO," in *18th Int. OFDM Workshop (InOWoS)*, Aug. 2014, pp. 1–8.

[79] B. Panzner, W. Zirwas, S. Dierks, M. Lauridsen, P. Mogensen, K. Pajukoski, and D. Miao, "Deployment and implementation strategies for massive MIMO in 5G," in *IEEE Global Telecommun. Conf. (Globecom) Workshop Massive MIMO*, Dec. 2014.

[80] S. Dierks, W. Zirwas, M. Jäger, B. Panzner, and G. Kramer, "MIMO and massive MIMO - analysis for a local area scenario," in *23nd European Signal Processing Conf. (EUSIPCO)*, Sep. 2015, pp. 2496–2500.

[81] S. Dierks and N. Jünger, "Scheduling for massive MIMO with few excess antennas," in *20th Int. ITG Workshop Smart Antennas (WSA)*, Mar. 2016, pp. 1–5.

[82] R. Jain, D.-M. Chiu, and W. R. Hawe, "A quantitative measure of fairness and discrimination for resource allocation in shared computer systems," DEC Research Report, Tech. Rep. 301, 1984.

[83] L. Råde and B. Westergren, *Springers Mathematische Formel*, P. Vachenauer, Ed. Springer Verlag, 2000.

[84] M. K. Ozdemir and H. Arslan, "Channel estimation for wireless OFDM systems," *IEEE Communications Surveys Tutorials*, vol. 9, no. 2, pp. 18–48, Feb. 2007.

[85] "TR36.104 - evolved universal terrestrial radio access (E-UTRA); base station (BS) radio transmission and reception," 3GPP, Tech. Rep. v12.10.0, Jan. 2016.

[86] P. Zetterberg, M. Bengtsson, D. McNamara, P. Karlsson, and M. A. Beach, "Performance of multiple-receive multiple-transmit beamforming in WLAN-type systems under power or EIRP constraints with delayed channel estimates," in *IEEE 55th Vehicular Technology Conf. (VTC)*, vol. 4, May 2002, pp. 1906–1910 vol.4.

[87] ——, "Downlink beamforming with delayed channel estimates under total power, element power and equivalent isotropic radiated power (EIRP) constraints," in *IEEE 54th Vehicular Technology Conf. (VTC)*, vol. 1, Oct. 2001, pp. 516–520 vol.1.

[88] N. Doose and P. A. Hoeher, "On EIRP control in downlink precoding for massive MIMO arrays," in *20th Int. ITG Workshop Smart Antennas (WSA)*, Mar. 2016, pp. 1–5.

[89] A. M. Kuzminskiy, "Downlink beamforming under EIRP constraint in WLAN OFDM systems," in *2006 14th European Signal Processing Conf. (EUSIPCO)*, Sep. 2006, pp. 1–5.

[90] C. M. Vithanage, Y. Wang, and J. P. Coon, "Transmit beamforming methods for improved received signal-to-noise ratio in equivalent isotropic radiated power-constrained systems," *IET Communications*, vol. 3, no. 1, pp. 38–47, Jan. 2009.

[91] C. M. Vithanage, J. P. Coon, and S. C. J. Parker, "On capacity-optimal precoding for multiple antenna systems subject to EIRP restrictions," *IEEE Trans. Wireless Commun.*, vol. 7, no. 12, pp. 5182–5187, Dec. 2008.

[92] K. Issiali, V. Guillet, G. E. Zein, and G. Zaharia, "Impact of EIRP constraint on MU-MIMO 802.11ac capacity gain in home networks," in *Mediterranean Conf. Information & Communication Technologies (MedICT)*. Springer International Publishing, 2015, pp. 75–84.

[93] W. L. Stutzman and G. A. Thiele, *Antenna Theory and Design*, 3rd ed. John Wiley & Sons, 2014.

[94] C. A. Balanis, *Antenna Theory - Analysis and Design*, 3rd ed. John Wiley & Sons, 2006.

[95] T. M. Kim, A. Ghaderipoor, and A. Paulraj, "Transmit beamforming for EIRP-limited MIMO systems based on Golay sequence," in *IEEE Global Communications Conf. (GLOBECOM)*, Dec. 2012, pp. 4798–4803.

[96] B. M. Hochwald, D. J. Love, S. Yan, P. Fay, and J. M. Jin, "Incorporating specific absorption rate constraints into wireless signal design," *IEEE Commun. Mag.*, vol. 52, no. 9, pp. 126–133, Sep. 2014.

[97] S. S. Oh and Y.-H. Lee, "Simulation study for EIRP measurement of base-station antenna using simple phase retrieval technique," in *16th Int. Seminar/Workshop Direct and Inverse Problems of Electromagnetic and Acoustic Wave Theory (DIPED)*, Sep. 2011, pp. 123–126.

[98] "Guidelines for determining the effective radiated power (ERP) and equivalent isotropically radiated power (EIRP) of a RF transmitting system," Federal Communications Commission (FCC), Tech. Rep. 412172, Jul. 2015.

[99] D. Ying, D. J. Love, and B. M. Hochwald, "Transmit covariance optimization with a constraint on user electromagnetic radiation exposure," in *IEEE Global Communications Conf. (GLOBECOM)*, Dec. 2013, pp. 4104–4109.

[100] "Series K: Protection against interference - guidance on complying with limits for human exposure to electromagnetic fields," ITU Telecommunication Standardization Sector (ITU-T), Tech. Rep. K.52, Dec. 2004.

[101] "15.247: Operation within the bands 902-928 MHz, 2400-2483.5 MHz, and 5725-5850 MHz," Federal Communications Commission (FCC), Tech. Rep., Jul. 2017.

[102] C. Carlson, "How I made wine glasses from sunflowers," http://blog.wolfram.com/2011/07/28/how-i-made-wine-glasses-from-sunflowers/, Jul. 2011.

[103] J. W. Cooley and J. W. Tukey, "An algorithm for the machine calculation of complex fourier series," *Mathematics of Computation*, vol. 19, no. 90, pp. 297–301, 1965.

[104] K. G. Paterson and V. Tarokh, "On the existence and construction of good codes with low peak-to-average power ratios," *IEEE Trans. Inf. Theory*, vol. 46, no. 6, pp. 1974–1987, Sep. 2000.

[105] G. Wunder and H. Boche, "Peak value estimation of bandlimited signals from their samples, noise enhancement, and a local characterization in the neighborhood of an extremum," *IEEE Trans. Signal Process.*, vol. 51, no. 3, pp. 771–780, Mar. 2003.

[106] M. Sharif, M. Gharavi-Alkhansari, and B. H. Khalaj, "On the peak-to-average power of OFDM signals based on oversampling," *IEEE Trans. Commun.*, vol. 51, no. 1, pp. 72–78, Jan. 2003.

[107] G. P. Styan, "Hadamard products and multivariate statistical analysis," *Linear Algebra and its Applications*, vol. 6, pp. 217–240, 1973. [Online]. Available: http://www.sciencedirect.com/science/article/pii/0024379573900232

[108] M. Grant and S. Boyd, "CVX: Matlab software for disciplined convex programming, version 2.1," http://cvxr.com/cvx, Mar. 2014.

[109] E. W. Weisstein, "Harmonic addition theorem. from MathWorld–a Wolfram web resource," http://mathworld.wolfram.com/HarmonicAdditionTheorem.html.